



National Library  
of Canada

Acquisitions and  
Bibliographic Services Branch

395 Wellington Street  
Ottawa, Ontario  
K1A 0N4

Bibliothèque nationale  
du Canada

Direction des acquisitions et  
des services bibliographiques

395, rue Wellington  
Ottawa (Ontario)  
K1A 0N4

*Vous l'avez vu. Vous l'avez vu.*

*Vous l'avez vu. Vous l'avez vu.*

## NOTICE

The quality of this microform is heavily dependent upon the quality of the original thesis submitted for microfilming. Every effort has been made to ensure the highest quality of reproduction possible.

If pages are missing, contact the university which granted the degree.

Some pages may have indistinct print especially if the original pages were typed with a poor typewriter ribbon or if the university sent us an inferior photocopy.

Reproduction in full or in part of this microform is governed by the Canadian Copyright Act, R.S.C. 1970, c. C-30, and subsequent amendments.

## AVIS

La qualité de cette microforme dépend grandement de la qualité de la thèse soumise au microfilmage. Nous avons tout fait pour assurer une qualité supérieure de reproduction.

S'il manque des pages, veuillez communiquer avec l'université qui a conféré le grade.

La qualité d'impression de certaines pages peut laisser à désirer, surtout si les pages originales ont été dactylographiées à l'aide d'un ruban usé ou si l'université nous a fait parvenir une photocopie de qualité inférieure.

La reproduction, même partielle, de cette microforme est soumise à la Loi canadienne sur le droit d'auteur, SRC 1970, c. C-30, et ses amendements subséquents.

Canada

UNIVERSITY OF ALBERTA  
TRANSVERSE FIELD IONIZATION CHAMBER FOR  
THE PARITY VIOLATION EXPERIMENT AT 230 MeV.

BY

TREVOR J. STOCKI



A thesis submitted to the Faculty of Graduate Studies and Research in partial  
fulfilment of the requirements for the degree of master of science.

IN

NUCLEAR PHYSICS

DEPARTMENT OF PHYSICS

Edmonton, Alberta

FALL 1993



National Library  
of Canada

Acquisitions and  
Bibliographic Services Branch

395 Wellington Street  
Ottawa, Ontario  
K1A 0N4

Bibliothèque nationale  
du Canada

Direction des acquisitions et  
des services bibliographiques

395, rue Wellington  
Ottawa (Ontario)  
K1A 0N4

*Voilà! Votre référence*

*Voilà! Votre référence*

**The author has granted an irrevocable non-exclusive licence allowing the National Library of Canada to reproduce, loan, distribute or sell copies of his/her thesis by any means and in any form or format, making this thesis available to interested persons.**

**L'auteur a accordé une licence irrévocable et non exclusive permettant à la Bibliothèque nationale du Canada de reproduire, prêter, distribuer ou vendre des copies de sa thèse de quelque manière et sous quelque forme que ce soit pour mettre des exemplaires de cette thèse à la disposition des personnes intéressées.**

**The author retains ownership of the copyright in his/her thesis. Neither the thesis nor substantial extracts from it may be printed or otherwise reproduced without his/her permission.**

**L'auteur conserve la propriété du droit d'auteur qui protège sa thèse. Ni la thèse ni des extraits substantiels de celle-ci ne doivent être imprimés ou autrement reproduits sans son autorisation.**

ISBN 0-315-88163-1

**Canada**

UNIVERSITY OF ALBERTA

RELEASE FORM

NAME OF AUTHOR: Trevor J. Stocki

TITLE OF THESIS: Transverse Field Ionization Chamber for  
the Parity Violation Experiment at 230  
MeV.

DEGREE: Master of Science

YEAR THIS DEGREE GRANTED: 1993

Permission is hereby granted to the University of Alberta Library to reproduce single copies of this thesis and to lend or sell such copies for private, scholarly or scientific research purposes only.

The author reserves all other publication and other rights in association with the copyright in the thesis, and except as hereinbefore provided neither the thesis nor any substantial portion thereof may be printed or otherwise reproduced in any material form whatever without the author's prior written permission.

(Signed).....

60 Rosewood Dr.

Sherwood Park, AB

CANADA, T8A-0L9

Date: .....

UNIVERSITY OF ALBERTA

FACULTY OF GRADUATE STUDIES AND RESEARCH

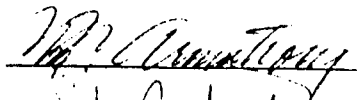
The undersigned certify that they have read, and recommend to the Faculty of Graduate Studies and Research for acceptance, a thesis entitled TRANSVERSE FIELD IONIZATION CHAMBER FOR THE PARITY VIOLATION AT 230 MeV submitted by TREVOR J. STOCKI in partial fulfillment of the requirements for the degree of Master of Science in Nuclear Physics.

Dr. G. Roy



Supervisor

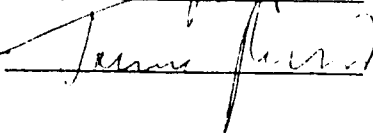
Dr. W. Armstrong



Dr. E. Nyland



Dr. J. Pinfold



DATED 4.27.98

To Evelyn,  
my mother, and my father.

## Abstract

A transverse field ionization chamber has been built and tested for the 230 MeV proton-proton parity nonconservation experiment at TRIUMF. This experiment will measure the longitudinal analyzing power  $A_L$ . The ionization chamber has been designed to minimize noise from attachment, recombination, spallation, delta ray, and space charge effects. The ionization chamber output has been found to follow a universal curve, which is a plot of the chamber's output divided by the chamber pressure and by the beam current versus the voltages applied to the chamber divided by the chamber pressure and by the square root of the beam current. By subtracting the two signals from the chamber, a mock data taking experiment was performed, which showed that the ionization chamber is intrinsically able to measure  $A_L$  to a statistical accuracy of  $\pm 2 \times 10^{-8}$  after 300 hours, assuming a liquid hydrogen target of 40 cm, and a beam polarization of 80%.

## Acknowledgements

I would like to thank Dr. Gerry Roy for his guidance and support in the supervision of my thesis. I would also like to thank my collaborators, Dr. W.T.H. van Oers, Dr. Shelley A. Page, Dr. Larry Lee, Alice Hamain, Dr. James Birchall, Dr. Charles A. Davis, Dr. John R. Campbell and Dr. W. Desmond Ramsay for all of their help answering my many questions.

The technical advice from Ken Lukas, John Yandon, Jan Schapman, Len Wampler, Shane Mullin, and the University of Alberta machinists was very beneficial to me and my thesis project. I would also like to thank Jeff Lange for proof reading my thesis and Jason Kosowan for his help with the laborious initial assembly of the ionization chamber.

I would also like to thank my parents who have always encouraged my education and Evelyn Hughes who believed in me, when I did not.



## Table of Contents

1	Introduction . . . . .	1
1.1	The General PNC Nucleon-Nucleon Potential . . . . .	5
1.2	Meson Exchange PNC Potential . . . . .	6
1.3	The Two Nucleon S-P Amplitudes . . . . .	12
2	Measurement of Nucleon-Nucleon PNC Effects . . . . .	16
2.1	Longitudinal Analyzing Power . . . . .	17
2.2	How $A_z$ Is Measured . . . . .	22
3	Ionization Chambers . . . . .	33
3.1	The Transverse Field Ionization Chambers . . . . .	36
3.2	Attachment . . . . .	41
3.3	Recombination . . . . .	42
3.4	Spallation Noise . . . . .	44
3.5	Noise from Delta Rays . . . . .	48
3.6	Space Charge . . . . .	56
3.7	Summary of Design Considerations . . . . .	62
4	Physical Setup of TRIC Tests . . . . .	63
4.1	How The Plateau Curves Were Obtained . . . . .	65
4.2	How the Noise Factor $\alpha$ Was Measured . . . . .	67
4.3	How $\delta A_z$ Was Measured . . . . .	73
5	Results of the Main Assembly Plateau Measurements . . . . .	76
5.1	Halo Monitor Plateau Results . . . . .	84
5.2	Results of the Alpha Measurements . . . . .	89
5.3	Results of the $\delta A_z$ Measurements . . . . .	93
5.4	TRIC Linearity . . . . .	95
6	Conclusions . . . . .	97
	Appendix A: TRIC High Voltage Problem . . . . .	98
	Appendix B: Hydrogen Safety . . . . .	104
	Appendix C: TRIC Bakeout Studies . . . . .	106
	Bibliography . . . . .	115

## List of Tables

Table 1.1: The four forces of nature and their relative strengths. . . . .	1
Table 1.2: Classification and examples of weak interactions . . . . .	1
Table 1.3: Exchange mesons considered for the PNC potential . . . . .	8
Table 1.4: Calculated values for nucleon-nucleon-meson weak couplings . . . . .	11
Table 1.5: Two nucleon S-P weak amplitudes and meson exchange equivalents . . . . .	13
Table 2.1: Systematic errors in the TRIUMF PNC experiment. . . . .	18
Table 2.2: Measurements of $A_z$ . . . . .	23
Table 3.1: Attachment coefficients for various gases. . . . .	42
Table 3.2: Spallation product energies and ranges. . . . .	47
Table 5.1: Knee voltages from universal curves. . . . .	79
Table C.1: Outgassing measurements made on the TRIC. . . . .	110

## List of Figures

Figure 1.1: An example of a leptonic weak decay is the decay of a muon . . .	2
Figure 1.2: An example of a semileptonic weak decay is the beta decay of a neutron. . . . .	2
Figure 1.2a: An example of a lambda decay . . . . .	2
Figure 1.3: The hadronic weak interaction in the proton-proton system. . . . .	7
Figure 2.1: The largest systematic error in the proton-proton system, circulating transverse polarization. . . . .	20
Figure 2.2a: The experimental setup for the LAMPF 15 MeV parity violation experiment. The scattered protons were detected in scintillators while a beam stop was used to detect the transmitted protons . . . . .	24
Figure 2.2b: The experimental setup for the PSI parity violation experiment. The scattered protons are detected in an ionization chamber while a faraday cup is used to detect the transmitted protons. . . . .	24
Figure 2.2c: The experimental setup for the LAMPF 800 MeV parity violation experiment. The transmitted protons were measured before and after the liquid hydrogen target by two ionization chambers. . . . .	27
Figure 2.3: The phase shifts for the proton-proton interaction. . . . .	27
Figure 2.4: The apparatus for the TRIUMF parity violation experiment. The beam is going from right to left. The intensity profile monitors and the fast steering magnets are used to center the beam. The polarisation profile monitors measure the amount of circulating transverse polarisation. Then the beam is measured by two transverse field ionization chambers (TRICs) before and after the liquid hydrogen target. . . . .	29
Figure 2.5: From top to bottom: the plates used in the beam profile monitor, a beam profile, and a comparison of the beam displacement when the fast feedback loop is on and off. . . . .	30
Figure 2.6: Theoretical predictions for $A_2$ compared with data from the Bonn, SIN, LAMPF, and ZGS experiments. . . . .	32
Figure 3.1: The basic parallel plate ionization chamber. The beam ionizes the gas. The electrons from this ionization travel to the collection plate. The guard plates are there to minimize the edge effects of the electric field. . . . .	34

Figure 3.2: The ion chamber's dependence on the applied voltage. . . . .	34
Figure 3.3: A beam's eye view of the TRIC plate assembly. The side electrodes increase by 1 kV per plate (from bottom to top). These electrodes are used to reinforce the electric field along the sides. . . . .	37
Figure 3.4: An above view of the seven collection plates of the TRIC. The triangular plates are used to measure beam alignment, the main plate is used for data taking and the wing plates measure the amount of halo. . . . .	37
Figure 3.5: The outer casing of the TRIC, indicating all the feedthroughs. . .	39
Figure 3.6: One of the two assemblies that make up the halo monitor. The shown assembly is made up of two small ion chambers. . . . .	39
Figure 3.7: The general shape of the energy spectra of fragments produced by spallation. . . . .	46
Figure 3.8: Spallation yields from .002" thick havar and from .003" thick stainless steel. There is very little difference between the two yields. . . . .	49
Figure 3.9: How the various elements in havar contribute to the total spallation yield. . . . .	50
Figure 3.10: The noise from delta rays tends to go like the inverse of the collection plate length. . . . .	54
Figure 3.11: The noise from delta rays tends to go like $P^{.418}$ and not like $1/\sqrt{P}$ , where P is the chamber pressure in atmospheres. . . . .	54
Figure 3.12: The space charge effects are shown. The applied field is denoted as $E_a$ . The opposing field is shown as $E_i$ and the sideways field is shown as $E_s$ . . . . .	57
Figure 4.1: An example of the output from the FFT. The peaks are at multiples of 60 Hz. . . . .	71
Figure 4.2: A histogram of a digitized difference signal. The full width half maximum of this histogram is used to calculate the noise figure, $\alpha$ . . . . .	71
Figure 4.3: A histogram of $\Delta V/V$ . The full width half maximum of this histogram is used to find $\delta A_z$ . . . . .	75
Figure 5.1: The TRIC output plotted versus the applied voltage for different beam currents as a chamber pressure of 1/3 of an atmosphere. . . . .	77

Figure 5.2: The universal curve for the main plate for beam currents from 100 nA to 500 nA and for chamber pressures of 1/3, 2/3, and 1 atmosphere. . . . .	77
Figure 5.3: The universal curve for beam currents of 250 nA and 320 nA, at a chamber pressure of 2/3 atmosphere. The beam current was measured for each point on the graph. . . . .	77
Figure 5.4: The universal curve for the three middle plates tied together, for a beam current of 130 nA, and a chamber pressure of 2/3 atmosphere. . .	80
Figure 5.5: Plateau curves for the left wing at various beam currents and at a chamber pressure of 1/3 of an atmosphere. . . . .	82
Figure 5.6a: Universal curves for the left wing for beam currents of 100 nA to 500 nA and chamber pressures of 1/3, 2/3 and 1 atmosphere. . . . .	83
Figure 5.6b: Universal curves for the right wing for beam currents of 100 nA to 500 nA and chamber pressures of 1/3, 2/3 and 1 atmosphere. . . . .	83
Figure 5.7: Plateau curve for bottom halo monitor for beam currents of 300 nA and 500 nA at a chamber pressure of 2/3 atmosphere. . . . .	85
Figure 5.8: Plateau curve for the bottom halo monitor. The internal signal cables have been shielded, but the bump is still there. The main assembly high voltage has been turned off. . . . .	86
Figure 5.9: Plateau curve for the bottom halo monitor in the same situation as in figure 5.8 except now the main assembly high voltage is on at -13 kV. Note that the scale of this figure is 5 times larger than figure 5.8. . . . .	86
Figure 5.10a: The amount of halo measured by the right halo monitor and the right wing. The halo monitor is 5.2 cm from the center of the beam and the wings are 3.8 cm from the center of the beam. . . . .	88
Figure 5.10b: The amount of halo measured by the left halo monitor and the left wing . . . . .	88
Figure 5.11: The range of $\alpha$ for different beam currents and different applied voltages. . . . .	90
Figure 5.12: The noise figure $\alpha$ does not decrease with increased pressure as the theoretical $\alpha$ from delta rays would imply. . . . .	90
Figure 5.13: The noise figure $\alpha$ increases with decreased length of collection plates . . . . .	92

Figure 5.14: The noise figure $\alpha$ does not go like $1/\sqrt{L}$ as the delta ray noise calculation implied. . . . .	92
Figure 5.15: A comparison of the two methods used to measure $\alpha$ . The digital alpha is about a factor of 1.5 to 3 larger than the FFT alpha. . . . .	94
Figure 5.16: The error in $A_z$ as a function of spin flip frequency. . . . .	94
Figure 5.17: The TRIC appears linear when compared with the SEM. . . . .	96
Figure 5.18: Since the TRIC is sensitive to space charge effects and the SEM is not, one would suspect that the ratio of TRIC/SEM should decrease as a function of beam current. . . . .	96
Figure A.1: The current drawn by the TRIC high voltage supply as a function of applied voltage. Note that the points above 0.3 mA are where the TRIC discharges . . . . .	99
Figure A.2: The approximate position of the discharge within the TRIC during the September 1992 high voltage tests. . . . .	100
Figure A.3: The various glows seen during the March 1993 high voltage tests	102
Figure C.1: The TRIC temperature as a function of time for the November 1992 baking. . . . .	107
Figure C.2: The TRIC temperature as a function of time for the March 1993 baking . . . . .	107
Figure C.3: The TRIC pressure as a function of time for the March 1993 baking . . . . .	109
Figure C.4: Rate of rise curve for a base pressure of $6.2 \times 10^{-6}$ torr. . . . .	111
Figure C.5: Rate of rise curve for a base pressure of $2.3 \times 10^{-6}$ torr. . . . .	111
Figure C.6: Rate of rise curve for a base pressure of $7.6 \times 10^{-8}$ torr. . . . .	112
Figure C.7: Rate of rise curve for a base pressure of $1.6 \times 10^{-8}$ torr. . . . .	112
Figure C.8: Rate of rise curve for a base pressure of $6.8 \times 10^{-9}$ torr. . . . .	113
Figure C.9: Outgassing rate of the TRIC as a function of heating time. . . . .	113

### List of Abbreviations

4ASEM	. . .	The secondary electron emission current monitor in beamline 4A at TRIUMF.
DDH	. . . .	Desplanques, Donoghue, and Holstien
FFT	. . . .	Fast fourier transform
GIM	. . . .	Glashow, Illiopoulos, and Maini
IPM	. . . .	Intensity profile monitor
LH <sub>2</sub>	. . . . .	Liquid hydrogen
PC	. . . . .	Parity conservation
PNC	. . . .	Parity nonconservation
QCD	. . . .	Quantum Chromodynamics
SEM	. . . .	Secondary electron emission current monitor
TRIC	. . . .	Transverse field ionization chamber
UHP	. . . .	Ultra high purity
V/F	. . . . .	Voltage to frequency converter

## 1 Introduction

There are four forces in nature: gravitational, electromagnetic, weak and strong nuclear forces. The table below shows the relative strengths of these forces:

Table 1.1: The four forces of nature and their relative strengths.

<u>Force</u>	<u>Relative Strength</u>
Strong nuclear	1
Electromagnetic	$10^{-2}$
Weak nuclear	$10^{-6}$
Gravitational	not measurable on the subatomic scale

The force under study is the weak force. Experimental tests have been done to test leptonic and semileptonic weak interactions but the hadronic or nonleptonic interaction has not been completely solved. Therefore, the weak interaction between nucleons is of interest. Examples of these types of interactions are listed below:

Table 1.2: Classification and examples of weak interactions.

Leptonic	$\mu^+ \rightarrow e^+ \nu_e \bar{\nu}_\mu$	$\nu_e e^- \rightarrow e^- \nu_e$
Semileptonic	$\Delta S = 0$ $n \rightarrow p e^- \bar{\nu}_e$ $\bar{\nu}_e p \rightarrow n e^+$	$\Delta S = 1$ $K^+ \rightarrow \pi^0 + e^+ + \nu_e$ $K^+ \rightarrow \mu^+ + \nu_\mu$
Hadronic	$N + N \rightarrow N + N$ PNC in Nuclei	$\Lambda \rightarrow \pi^- p$ $K^+ \rightarrow \pi^+ \pi^0$

where PNC stands for parity nonconservation, and S is the strangeness quantum number. Figure 1.1 shows an example of a leptonic weak interaction, namely muon decay. A semileptonic interaction is also shown in figure 1.2. In this figure, the beta



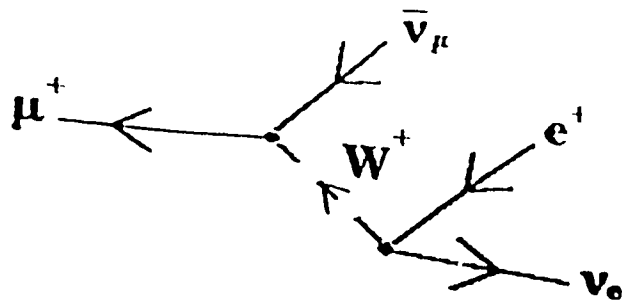


Figure 1.1: An example of a leptonic weak decay is the decay of a muon.

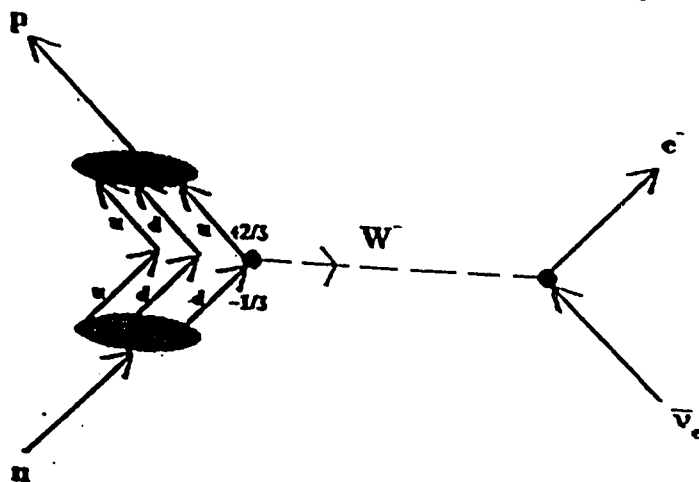


Figure 1.2: An example of a semileptonic weak decay is the beta decay of a neutron.

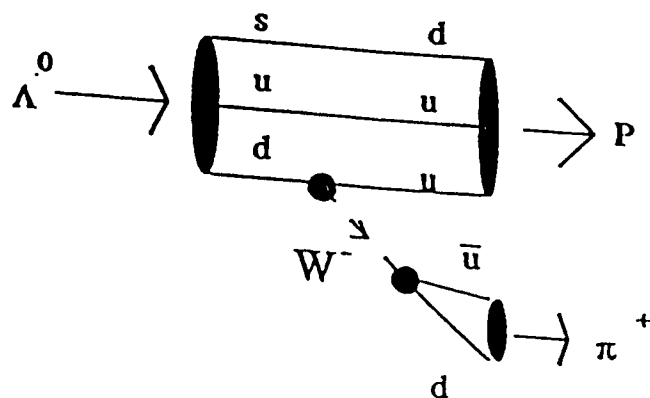


Figure 1.2a: An example of a lambda decay.

decay of a neutron is depicted. A third type of weak interaction, namely the hadronic weak  $p + p \rightarrow p + p$  interaction was studied. Normally the strong and electromagnetic forces mask the effects of the weak force therefore the weak interaction can only be examined when the effects of the strong and electromagnetic forces are very small. This can be accomplished by the use of a symmetry principle which is conserved by the strong and electromagnetic forces but violated by the weak interaction, such as parity nonconservation.

In the present Standard Model, it has been found that strangeness changing and charm changing weak neutral current ( $Z^0$ ) interactions are suppressed by the Glashow, Iliopoulos, and Maini (GIM<sup>1</sup>) mechanism. The GIM mechanism, a theory that was introduced by Glashow, Iliopoulos, and Maiani (GIM) in 1970, showed that the existence of a new quark namely the charm quark (the charm quark was not discovered till 1974), would require that extra terms would need to be added to the weak neutral current interaction matrix element. These new terms cancel with the strangeness changing part of the weak neutral current interaction. It is because of these new terms that only nonstrangeness changing  $\Delta S = 0$  weak neutral current interactions can occur between quarks. This last statement would imply that  $Z^0$  interactions between quarks can only be studied by the use of a flavour conserving process. At first glance it would be thought that the flavour changing reaction  $\Lambda \rightarrow \pi^- p$  must be a neutral current process. But it turns out that this reaction is a charged current strangeness changing reaction and is not a neutral current reaction, as shown in figure 1.2. In this charged current reaction, the strange quark in the  $\Lambda$  decays

into an up quark and a  $W^-$ . This  $W^-$  then becomes outgoing the  $\pi^-$ . This last example shows that the weak neutral current interaction between quarks can not be studied in a flavour changing process. So the weak neutral current interaction between quarks can only be studied in parity nonconserving, flavour conserving nucleon-nucleon reactions.

Currently the weak interaction described by the Standard Model only describes weak interactions between point particles, like quarks and leptons. The model does not completely describe the weak interaction between structured particles, like hadrons. This last statement is due to the fact that weak interactions between hadrons are affected by the strong interaction. In other words in order to know the hadronic weak interaction well, one must know the strong interaction well. Quantum chromodynamics (QCD) may be the right theory for the strong force, but QCD is not exactly solved at the low momentum transfer limit (nonperturbative limit). The difficulty of this problem is shown when one considers the  $\Delta I = 1/2$  (where  $I$  stands for isospin) rule for hadronic weak, charged current, strangeness changing decays, like  $\Lambda \rightarrow N\pi$ . The Standard Model says that there should be  $\Delta I = 1/2$  and  $\Delta I = 3/2$  decay amplitudes in this  $\Delta S = 1$  hadronic weak process. Experimental results show that the  $\Delta I = 3/2$  decay amplitudes are suppressed (by a factor of 20) in comparison with the  $\Delta I = 1/2$  decay amplitudes. The Standard Model does not explain this suppression. This unexplained anomaly must be due to the strong interaction since the Standard Model describes the weak interaction and doesn't account for the suppression. Therefore, one can learn about both the strong and weak interactions by

looking at these hadronic weak interactions ( $\Delta S = 0$  and  $\Delta S = 1$ ).

### 1.1 The General PNC Nucleon-Nucleon Potential

In the energy region which is of interest to us, namely the low energy region ( $< 1$  GeV), the hadronic weak interaction can be described by a phenomenological current-current Lagrangian. This Lagrangian is:

$$L = \frac{G_F}{\sqrt{2}} (J_w^\dagger J_w + J_z^\dagger J_z) + \frac{G_F}{\sqrt{2}} (J_w^\dagger J_w + J_z^\dagger J_z)^\dagger \quad (1.1)$$

where  $J_w$  is the charged weak current (due to  $W^\pm$  boson exchange),  $J_z$  is the neutral weak current (due to  $Z^0$  exchange),  $G_F$  is the Fermi coupling constant, and the superscript  $\dagger$  are abbreviations for Hermitian conjugate. In this model, since we are dealing with low energy, we can neglect charm, bottom, and top quark contributions and keep only the up, down, and strange quark contributions. This description is the general description of the PNC nucleon-nucleon interaction.

There are two more specific descriptions of the PNC nucleon-nucleon interaction, both of which are model dependent. One of these descriptions describe the interaction in terms of five S-P amplitudes which is examined in section 1.3. The other description uses single meson exchange ( $\pi$ ,  $\rho$ , and  $\omega$ ) and the multiple ( $2\pi$ ) meson exchange models. In the meson exchange model one of the vertices is governed by the strong interaction, while the other vertex is governed by the weak

interaction.

## 1.2 Meson Exchange PNC Potentials

At the energies lower than 300 MeV, Adelberger & Haxton<sup>2</sup> assert that the parity conserving (PC) nucleon-nucleon interaction can be described by the use of meson exchange potentials. This meson exchange idea can be used to explain the PNC interaction by changing one of the meson couplings to a weak coupling. This is shown in figure 1.3. By effectively putting a "magnifying glass" on the weak vertex, one can see all of the structure of the  $W^\pm$  and  $Z^0$  exchanges.

In the static limit, the mass  $m$  and the momentum transfer  $p$  of the exchange meson are in the denominator of the meson propagator in the form  $p^2 + m^2$ . Since the mass and the momentum transfer appear in the denominator, light meson exchange will dominate at low energies. This would imply that the PNC nucleon-nucleon interaction will be described by the exchange of light mesons which are listed in table 1.3. Thus, as the center of mass energy increases, more types of meson exchange diagrams will contribute to the potential, however only mesons with  $m^2 < p^2$  will contribute.

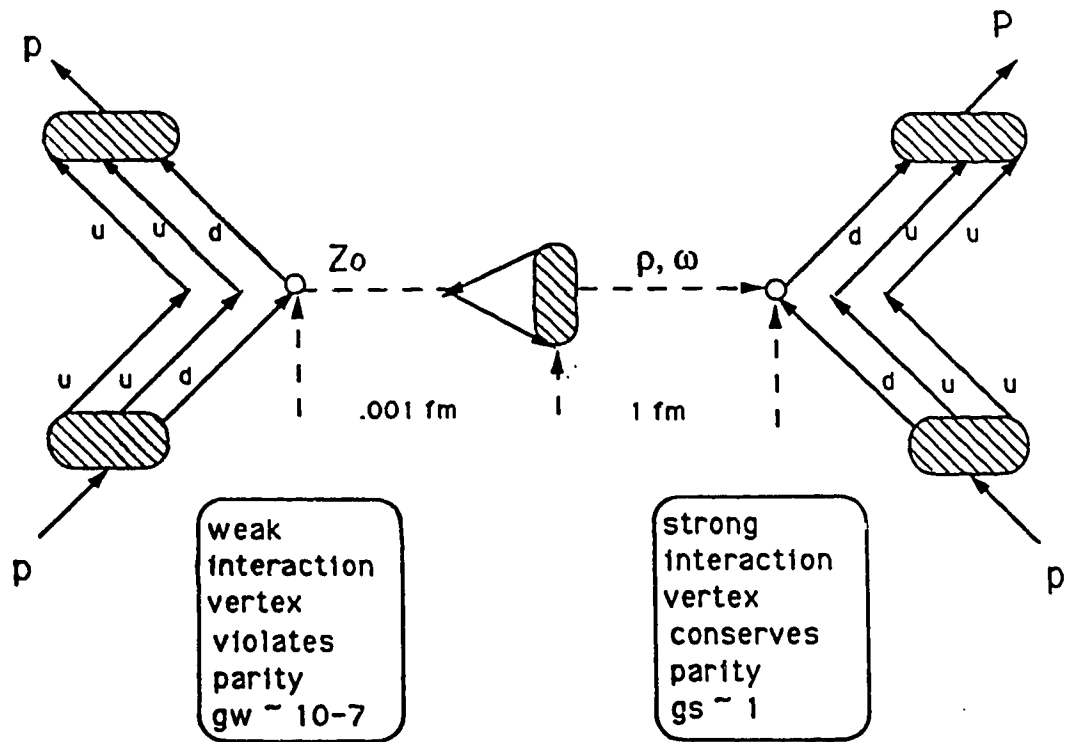


Figure 1.3: The hadronic weak interaction in the proton-proton system.

Table 1.3: Exchange mesons considered for the PNC potential.

Type of meson	Name	Mass (MeV)
Pseudoscalar	$\pi$	140
	$\eta$	549
	$\eta'$	958
Scalar	$S$	975
	$\delta$	983
Vector	$\rho$	769
	$\omega$	783
	$\phi$	1020

However, not all of these mesons contribute. By the use of Barton's theorem<sup>3</sup> the neutral scalar and pseudoscalar mesons ( $\pi^0$ ,  $\eta$ ,  $\eta'$ ,  $S$ ,  $\delta^0$ ) do not contribute to the PNC potential. Barton's theorem states that CP invariance and hermiticity disallows the coupling of neutral  $J = 0$  mesons. In other words these neutral pseudoscalar and neutral scalar mesons are their own antiparticles therefore they have a charge conjugation (C) of +1. Since we are looking at a PNC effect parity (P) is violated and since CPT must be conserved, time reversal (T) must be violated. The only evidence so far, from the neutral kaon system, of time reversal violation has been a factor of 1000 smaller than PNC effects. The above considerations would then imply that  $\pi^0$ ,  $\eta$ ,  $\eta'$ ,  $S$ , and  $\delta^0$  exchange in the PNC proton-proton system would be of the order of  $10^{-10}$ , which is not measurable at this time. The conservation of CPT does not eliminate the neutral vector mesons,  $\omega^0$  and  $\rho^0$ . This is because the neutral vector mesons have separate antiparticles, like the neutron. The neutrons and antineutrons are distinguished by the fact that the direction of the magnetic moment is flipped with respect to the spin of the particle. McKellar & Pick<sup>4</sup> have shown that  $\delta^\pm$  is just a

form factor correction to  $\pi^\pm$  exchange. They have also argued that  $\phi$  exchange is small in comparison to  $\rho$  and  $\omega$  exchange. These arguments show that in the PNC nucleon-nucleon system the single exchanges of  $\pi^\pm$ ,  $\rho^\pm$ ,  $\rho^0$ , and  $\omega^0$  dominate.

Thus, it can be seen that the PNC potential can be broken up into 3 parts:

$$V^{PNC} = V_{\pi^\pm} + V_{\text{vector mesons}} + V_{2\pi} \quad (1.2)$$

Where the vector mesons exchanged are the  $\rho^\pm$ ,  $\rho^0$ , and  $\omega^0$  mesons. The nonrelativistic potential, which does not include  $2\pi$  exchanges, will now be looked at.

Holstein<sup>5</sup> finds the nonrelativistic PNC nucleon-nucleon potential as:



$$\begin{aligned}
V_{12}^{PNC} = & \frac{f_\pi g_{\pi NN}}{\sqrt{2}} i \left( \frac{\vec{\tau}_1 \times \vec{\tau}_2}{2} \right)^3 (\vec{\sigma}_1 + \vec{\sigma}_2) \cdot \left[ \frac{\vec{p}_1 - \vec{p}_2}{2M} f_\pi(r) \right] \\
& - g_\rho (h_\rho^0 \vec{\tau}_1 \cdot \vec{\tau}_2 + h_\rho^1 \left( \frac{\vec{\tau}_1 + \vec{\tau}_2}{2} \right)^3 + h_\rho^2 \frac{(3\tau_1^3 \tau_2^3 - \vec{\tau}_1 \cdot \vec{\tau}_2)}{2\sqrt{6}}) \\
& \quad \times ((\vec{\sigma}_1 - \vec{\sigma}_2) \cdot \left[ \frac{\vec{p}_1 - \vec{p}_2}{2M} f_\rho(r) \right] \\
& \quad + i(1 + \chi_v) \vec{\sigma}_1 \times \vec{\sigma}_2 \cdot \left[ \frac{\vec{p}_1 - \vec{p}_2}{2M} f_\rho(r) \right]) \\
& \quad - g_\omega (h_\omega^0 + h_\omega^1 \left( \frac{\vec{\tau}_1 + \vec{\tau}_2}{2} \right)^3) \\
& \quad \times ((\vec{\sigma}_1 - \vec{\sigma}_2) \cdot \left[ \frac{\vec{p}_1 - \vec{p}_2}{2M} f_\omega(r) \right] \\
& \quad + i(1 + \chi_s) \vec{\sigma}_1 \times \vec{\sigma}_2 \cdot \left[ \frac{\vec{p}_1 - \vec{p}_2}{2M} f_\omega(r) \right]) \\
& - (g_\omega h_\omega^1 - g_\rho h_\rho^1) \left( \frac{\vec{\tau}_1 - \vec{\tau}_2}{2} \right)^3 \times (\vec{\sigma}_1 + \vec{\sigma}_2) \cdot \left[ \frac{\vec{p}_1 - \vec{p}_2}{2M} f_\rho(r) \right] \\
& - g_\rho h_\rho^1 i \left( \frac{\vec{\tau}_1 \times \vec{\tau}_2}{2} \right)^3 \times (\vec{\sigma}_1 + \vec{\sigma}_2) \cdot \left[ \frac{\vec{p}_1 - \vec{p}_2}{2} M f_\rho(r) \right]
\end{aligned} \tag{1.3}$$

where

$$f_v(r) = \frac{\exp(-m_v r)}{4\pi r} \quad v = \pi, \rho, \omega \tag{1.4}$$

is the Yukawa potential for the corresponding mesons,  $p_1$  and  $p_2$  are the momenta of the nucleons,  $\sigma_1$  and  $\sigma_2$  are the spin matrices for the two nucleons,  $\tau_1$  and  $\tau_2$  are the isospin matrices for the two nucleons, and  $\chi_v$ ,  $\chi_s$  are the isovector and isoscalar nucleon anomalous magnetic moments. The strong coupling constants are given by  $g$ , where the subscript denotes the meson exchanged. The coupling constants are

denoted by a subscript (which identifies the meson exchanged) and a superscript (which describes the isospin the coupling is carrying). For example,  $h_\rho^0$  is the coupling constant for  $\rho$  exchange with  $\Delta I = 0$ , and  $h_\omega^1$  is the coupling constant for  $\omega$  exchange with  $\Delta I = 1$ . The exception to this notation is the pion coupling constant,  $f_\pi$  which describes  $\pi$  exchange. This  $\pi$  exchange is only  $\Delta I = 1$  exchange. Whereas the  $\rho$  and  $\omega$  are both  $\Delta I = 0,1$  exchanges. A  $\Delta I = 2$  exchange also occurs and it is due to  $\rho$  exchange.

Desplanques, Donoghue, and Holstein (DDH)<sup>6</sup> have calculated these weak coupling constants. They have also included a "reasonable range" for each value, because of uncertainties associated with symmetry breaking and associated with strong interaction effects. Table 1.4 shows these calculated values for nucleon-nucleon-meson weak couplings in the Weinberg-Salam ( $Z^0$  and  $W^\pm$  exchange) model:

Table 1.4: Calculated values for nucleon-nucleon-meson weak couplings.

Weinberg-Salam Model	Reasonable Range	Best Value
$f_\pi$	$0 \rightarrow 30$	12
$h_\rho^0$	$30 \rightarrow -81$	-30
$h_\rho^1$	$-1 \rightarrow 0$	-0.5
$h_\rho^2$	$20 \rightarrow -29$	-25
$h_\omega^0$	$15 \rightarrow -27$	-5
$h_\omega^1$	$5 \rightarrow -2$	-3

These amplitudes are in units of  $g_w = 3.8 \times 10^{-8}$  which is the canonical weak interaction scale.

The above is for the nucleon-nucleon system. For the proton-proton system things become simpler. Since the proton-proton reaction conserves flavour, only the

neutral weak current is involved. This last statement implies that only the neutral vector mesons are exchanged, namely  $\rho^0$  and  $\omega^0$ . This weak proton-proton interaction is unlike the strong proton-proton interaction, which is dominated by  $\pi^0$  exchange.

### 1.3 The Two Nucleon S-P Amplitudes

It turns out that  $V^{PNC}$  from the prior sections can be broken up into three terms according to isospin:

$$V^{PNC} = V_{\Delta I=0}^{PNC} + V_{\Delta I=1}^{PNC} + V_{\Delta I=2}^{PNC} \quad (1.5)$$

This potential, at low energies can be written in terms of five S-P amplitudes, which are given in table 1.5. The crosses in this table indicate the reaction in which the amplitude is involved. The transition notation is the spectroscopic notation, where the subscript is the total angular momentum of the system, the letter denotes the total orbital angular momentum (S denotes 0, P denotes 1, D denotes 2 and so on), and the superscript is  $2s + 1$ , where  $s$  is the total spin of the system. For example,  $^3S_1$  denotes a total angular momentum of 1, a total orbital angular momentum of 0, and a total spin of 1. Customarily these 5 zero range amplitudes are included with a sixth parameter namely PNC pion-nucleon coupling constant  $F_\pi$ .

Table 1.5: Two nucleon S-P weak amplitudes and meson exchange equivalents.

Transition	$\Delta I$	n-n	n-p	p-p	N-N system exchanges
$^3S_1 \leftrightarrow ^1P_1$	0		x		$\rho^\pm, \rho^0, \omega^0$
$^1S_0 \leftrightarrow ^3P_0$	0	x	x	x	$\rho^\pm, \rho^0, \omega^0$
	1	x		x	$\rho^0, \omega^0$
	2	x	x	x	$\rho^\pm, \rho^0$
$^3S_1 \leftrightarrow ^3P_1$	1		x		$\pi^\pm, \rho^\pm, \rho^0, \omega^0$

Equation (1.6) gives the PNC coupling constants and their equivalent weak/strong coupling constant combinations.

$$\begin{aligned}
 F_\pi &= g_{\pi NN} \frac{f_\pi}{\sqrt{32}} \\
 F_0 &= -g_\rho \frac{h_\rho^0}{2} \\
 F_1 &= -g_\rho \frac{h_\rho^1}{2} \\
 F_2 &= -g_\rho \frac{h_\rho^2}{2} \\
 G_0 &= -g_\omega \frac{h_\omega^0}{2} \\
 G_1 &= -g_\omega \frac{h_\omega^1}{2} \\
 H_1 &= -g_\rho \frac{h_\rho'^1}{4}
 \end{aligned} \tag{1.6}$$

Note that in the  $^3S_1 \leftrightarrow ^3P_1$  case there is a pion exchange component. This component can be filtered out from the heavier meson exchange components, using the fact that

the pion is too light to satisfy the zero range approximation, as do the heavier vector mesons.

By looking at weak nucleon-nucleon partial wave amplitudes near threshold, the meson exchange potential and the  $S \rightarrow P$  amplitudes can be related. The partial wave scattering amplitudes are given by:

$$f_{nn}^{pn}(\vec{k}', \vec{k}) = V_{nn}^{pn} [(\vec{k}' + \vec{k}) \cdot [\vec{\sigma}_1 - \vec{\sigma}_2] + i(\vec{k}' - \vec{k}) \cdot [\vec{\sigma}_1 \times \vec{\sigma}_2]]$$

$$\vec{k} = \frac{\vec{k}_1 - \vec{k}_2}{2}$$

$$\vec{k}' = \frac{\vec{k}'_1 - \vec{k}'_2}{2}$$
(1.7a)

and by,

$$f_{pn}(\vec{k}', \vec{k}) = \frac{V_{pn}}{2} [(\vec{k}' + \vec{k}) \cdot [\vec{\sigma}_p - \vec{\sigma}_n] + i(\vec{k}' - \vec{k}) \cdot [\vec{\sigma}_p \times \vec{\sigma}_n]]$$

$$+ \frac{U_{pn}}{2} [(\vec{k}' + \vec{k}) \cdot [\vec{\sigma}_p - \vec{\sigma}_n] - i(\vec{k}' - \vec{k}) \cdot [\vec{\sigma}_p \times \vec{\sigma}_n]]$$

$$+ W_{pn}(\vec{k}' + \vec{k}) \cdot [\vec{\sigma}_p + \vec{\sigma}_n]$$

$$\vec{k} = \frac{\vec{k}_p - \vec{k}_n}{2}$$

$$\vec{k}' = \frac{\vec{k}'_p - \vec{k}'_n}{2}$$
(1.7b)

Where  $k$  is the initial nucleon momentum,  $k'$  is the final nucleon momentum, and  $\sigma_p$  ( $\sigma_n$ ) is the  $\sigma$  matrix element between initial and final proton (neutron) spins. The  $S \rightarrow P$  amplitudes are given below, in the Born approximation. The  $^1S_0 \rightarrow ^3P_0$

amplitudes  $V$  are given by:

$$\begin{aligned} V_{nn}^{pp} &\approx \frac{1}{m_\rho^2} [(F_0 \pm F_1 + \frac{F_2}{\sqrt{6}})(2 + \mu_v) + (G_0 \pm G_1)(2 + \mu_s)] \\ V_{pn} &\approx \frac{1}{m_\rho^2} [(F_0 - \sqrt{\frac{2}{3}} F_2)[2 + \mu_v] + G_0[2 + \mu_s]] \end{aligned} \quad (1.8a)$$

where  $\mu_s$  and  $\mu_v$  are the strong scalar and vector magnetic moments.

The  $^3S_1 \rightarrow ^3P_1$  amplitude  $W_{pn}$  is given by:

$$W_{pn} \approx \frac{1}{m_\rho^2} [2F_\pi \frac{m_\rho^2}{m_\pi^2} + 2H_1 + G_1 - F_1] \quad (1.8b)$$

Finally, the  $^3S_1 \rightarrow ^1P_1$  amplitude is:

$$U_{pn} \approx \frac{1}{m_\rho^2} [G_0 \mu_s - 3F_0 \mu_v] \quad (1.8c)$$

These above amplitudes were given by Adelberger & Haxton<sup>2</sup>, where they assumed  $m_\rho = m_\omega$ .

If PNC experiments were easy then it would be possible to get these 5 partial wave amplitudes from 5 low energy nucleon-nucleon experiments. One of these experiments would even be able to get the pion exchange contribution out of the  $^3S_1 \rightarrow$

$^3P_1$  amplitude. But it turns out that these low energy measurements are very difficult. Adelberger & Haxton<sup>2</sup> assert that the measurements are so difficult that only one observable has shown a definite PNC effect. This implies that to get all the information on PNC effects, one must look at complex nuclei (which won't be examined here).

## 2 Measurement of Nucleon-Nucleon PNC Effects

This section will look at the types of experiments that can be done to look at PNC effects. The strength of the PNC interaction as compared to the PC nucleon-nucleon interactions goes like:

$$\frac{4\pi G_F m_\pi^2}{g_{\pi NN}^2} \approx 10^{-7} \quad (2.1)$$

where  $m_\pi$  is the mass of the pion,  $G_F$  is the Fermi coupling constant, and  $g_{\pi NN}$  is the strong pion coupling constant. This above expression implies that the hadronic weak interaction is  $10^7$  times smaller than the hadronic strong interaction. This fact would imply that a measurement of hadronic weak interactions is a very small effect in comparison to hadronic strong interactions. To measure this tiny contribution to the nucleon interaction experimentalists will have to minimize statistical and systematic errors.

## 2.1 Longitudinal Analyzing Power

The PNC observable in the proton-proton (p-p) system is the longitudinal analyzing power, which is:

$$A_z = \frac{1}{P_z} \frac{\sigma^+(\theta) - \sigma^-(\theta)}{\sigma^+(\theta) + \sigma^-(\theta)} \quad (2.2)$$

where  $P_z$  is the amount of the beam which is longitudinally polarized, where  $\theta$  is the angle between the incident proton and the scattered proton,  $\sigma^+(\theta)$  and  $\sigma^-(\theta)$  are the cross sections when the spin of the proton is parallel and antiparallel to the beam direction, respectively. In a proton-proton scattering experiment, a parity operation is equivalent to flipping the spin of the incident longitudinal polarized proton. So the numerator of equation 2.2 is a measure of parity violation because it is the difference between the cross sections of flipped protons. Note that this  $A_z$  should not be confused with the helicity dependence of the total cross section. For low energy p-p scattering ( $E_p < 50$  MeV) the analyzing power and the helicity dependence are approximately equal, but in p-d or p- $\alpha$  scattering they are not approximately equal at any energy.

To get a precise measurement of  $A_z$  the spin state of the beam will have to be flipped at a rate which is fast enough such that the beam properties (like beam intensity, beam position, and emittance) don't change. This condition would imply a need for a beam source which can put out a high amount of polarization and a fast



spin flip rate. But there will still be some systematic errors, that will have to be accounted for by subtracting them out. Equation 2.3 illustrates this:

$$A_{\text{exp}} = A_z + \sum \frac{\Delta A}{\Delta x_i} \Delta x_i \quad (2.3)$$

where  $A_{\text{exp}}$  is the measured asymmetry,  $\Delta x_i$  is the variation in the beam property, and  $\Delta A/x_i$  is the sensitivity of  $A_z$  to a given beam parameter. Below is a table of systematic errors that occur when  $A_z$  is measured for the TRIUMF PNC experiment:

Table 2.1: Systematic errors in the TRIUMF PNC experiment.

Parameter	$\Delta A/x_i$	$\Delta x_i$	$\Delta A_z$
Current	$3 \times 10^{-4} \Delta I/I$	$1.8 \times 10^{-5}$	$5 \times 10^{-9}$
Position	$7 \times 10^{-9}/\text{mm}$	0.01	$7 \times 10^{-11}$
Size	$3 \times 10^{-6}/\text{mm}$	$< 0.01 \text{ mm}$	$3 \times 10^{-8}$
$P_x, P_y$	$4 \times 10^{-7}$	0.001	$4 \times 10^{-10}$
$xP_y, yP_x$	$4 \times 10^{-5}/\text{mm}$	$1.3 \times 10^{-4} \text{ mm}$	$5 \times 10^{-9}$
Energy	$3 \times 10^{-9}/\text{eV}$	$< < 1 \text{ eV}$	$< < 3 \times 10^{-9}$

where  $\Delta A_z$  is the false asymmetry due to that beam parameter,  $P_x$  and  $P_y$  are unwanted transverse polarization components, and the circulating transverse polarization is proportional to  $xP_y$  and  $yP_x$ .

The first systematic error in table 2.1 is helicity dependent current changes. This will cause a false measurement in  $A_z$ . It is estimated that this effect will lead to a false asymmetry of  $5 \times 10^{-9}$ . This result is measured for the situation when the spin flip occurs within the ion source of the cyclotron. Data will also be taken by having the spin flipped by use of a spin precessor after the beam has been extracted from the ion source.

The second systematic error in table 2.1 is helicity dependent beam position changes. This effect is estimated to give a false asymmetry of  $7 \times 10^{-11}$ . This asymmetry will be dealt with by use of a fast feedback loop, which will be discussed in section 2.2.

Table 2.1 lists size modulation as a third systematic error in  $A_z$ . At this point in the preparation of the TRIUMF experiment, size modulation effects are not well known. During the final data taking the beam size will be monitored by use of an intensity profile monitor which will be described in the next section. If this intensity profile monitor shows large helicity dependent size changes, then this systematic error will be corrected for by the same method which is used in helicity current changes.

Another systematic error in  $A_z$  that is listed in table 2.1 is due to beam energy changes which are correlated with the spin flip. This error comes from the fact that if the energy of the beam changes slightly between spin flips, then the amount of energy deposited in the ion chambers changes. This change in deposited energy results in a change in signal which is a false  $A_z$  effect. This effect is minimized by having the energy modulation within the cyclotron's optically pumped polarized ion source much less than 1 eV. It has been estimated that a 5 eV change in beam energy before the beam enters the cyclotron will result in a .15% change in horizontal beam size and a .5% change in vertical beam size. To test this estimation an induced energy modulation will be performed at the ion source and then the beam spot size changes will be measured with the intensity profile monitor. The intensity profile monitor will be described in the next section.

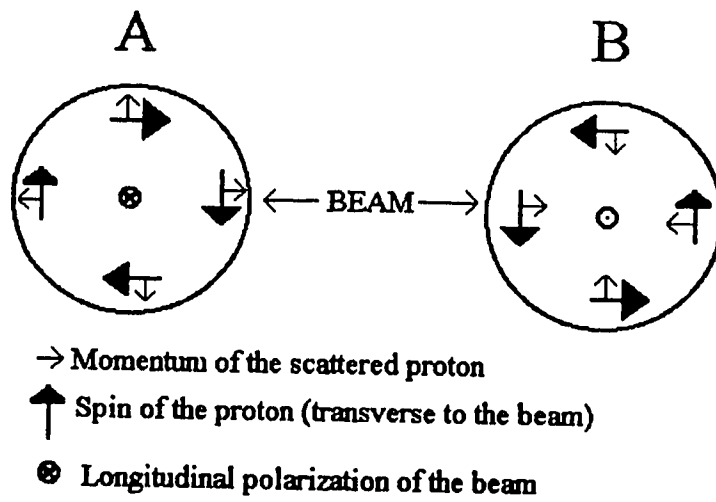


Figure 2.1: The largest systematic error in the proton-proton system, circulating transverse polarization.

Another systematic error in  $A_z$  that is shown in table 2.1 is due to unwanted transverse polarization components  $P_x$  and  $P_y$ . Since the parity conserving analyzing power in proton-proton scattering at 230 MeV is about a factor of 10 larger than at the lower energies,  $P_x$  and  $P_y$  give a large false asymmetry. In the TRIUMF experiment this effect is dealt with by adjusting the spin precession solenoids to yield an average  $P_x$  and  $P_y$  less than 0.1%.

The most serious systematic error in the p-p system is due to a residual transverse component of the polarization of the beam. This is a second order effect. Figure 2.1 shows how this effect is a problem. In figure 2.1a there are positive helicity protons coming out of the page. These protons have a small amount of transverse polarization which is oriented clockwise. Now assuming that proton scattering has a large transverse analyzing power, it is found that positive helicity protons scatter mostly to the left. Therefore the protons prefer to be scattered outward. When the spin is flipped the transverse component of the polarization is in the counterclockwise direction (figure 2.1b). This would now imply that the protons prefer to scatter inward. This effect of having the protons scatter outward then inward looks just like a PNC effect. This false effect is called circulating transverse polarization. It is proportional to  $\langle xp_y \rangle$  and  $\langle yp_x \rangle$  (where  $p_x$  and  $p_y$  are the x and y components of the beam's polarization). This effect vanishes for a perfect  $4\pi$  detector. The effect can be measured by measuring the polarization profile of the beam. This circulating transverse polarization is produced when the beam passes through a bending magnet asymmetrically. Basically when a transversely polarized

proton passes through the center of a magnetic dipole it is unaffected because the magnetic field lines are in the same direction as the spin of the proton. But when the longitudinally polarized proton enters the magnet off axis, the proton tends to precess slightly because of the fringe fields have a small magnetic field component which is parallel or antiparallel to the beam direction. These fringe fields are the cause of the circulating transverse polarization. These small fringe fields are in opposite directions above and below the center of the magnet, so the small transverse component gained by a proton going through upper portion of the magnet is the reverse of the small transverse component gained by a proton going through the lower portion of the magnet.

## 2.2 How $A_z$ Is Measured

The PNC observable in the p-p system is  $A_z$ .  $A_z$  is sensitive to  $\Delta I = 0, 1, 2$   $^1S_0 \leftrightarrow ^3P_0$  amplitudes in the low energy limit ( $E_p < 50$  MeV). At this low energy  $A_z$  is independent of  $\theta$ , and  $A_z$  has an energy dependence which is given by the PC  $^1S$  and  $^3P$  phase shifts. The weak matrix elements are constant in this low energy region. These above facts would imply that at  $E_p < 50$  MeV, experiments measure the same PNC quantity. For  $E_p > 50$  MeV, S-P and higher order partial wave PNC amplitudes cause  $A_z$  to have both angular and energy dependence.

$A_z$  can be measured in a transmission experiment or in a scattering experiment. In both cases to get a statistical accuracy of  $10^8$ ,  $10^{16}$  protons must be detected because statistical accuracy goes like the square root of the number of particles

detected. If individual signal pulses were counted at a rate of 10 MHz, then it would take about 30 years to get the required statistical accuracy. This implies that detector currents must be integrated rather than having detector pulses counted. If this current integration method is used, then in some experiments statistical accuracy would be achieved after only a number of hours. The TRIUMF experiment that will be discussed below will use 300 hours of data taking. Transmission experiments are performed at high energies where there are enough scattered protons to see the effect. This is the opposite to low energy experiments, where there is very little scattering and the PNC effect can only be seen by detecting scattered protons. Below is a table of the results from p-p PNC experiments:

Table 2.2: Measurements of  $A_z$ .

Energy	Lab	$A_z \times 10^{-7}$	Reference
13.6 MeV	Bonn	$-(1.5 \pm 0.5)$	7
15 MeV	LAMPF	$-(1.7 \pm 0.8)$	8
45 MeV	PSI	$-(1.50 \pm .22)$	9
46 MeV	Berkeley	$-(1.3 \pm 2.3)$	2
47 MeV	Texas A&M	$-(4 \pm 3)$	2
230 MeV	TRIUMF	under way	10
800 MeV	LAMPF	$2.4 \pm 1.1$	11
5.3 GeV	ZGS	$26.5 \pm 6.0$	11
3 GeV	Saclay	suggested	11
22 GeV	BNL	suggested	11
$\geq 200$ GeV	Fermilab	suggested	11

The last 3 have only been suggested. It is not known if they are actually being researched.

The first p-p PNC result was determined by the Los Alamos<sup>8</sup> group at

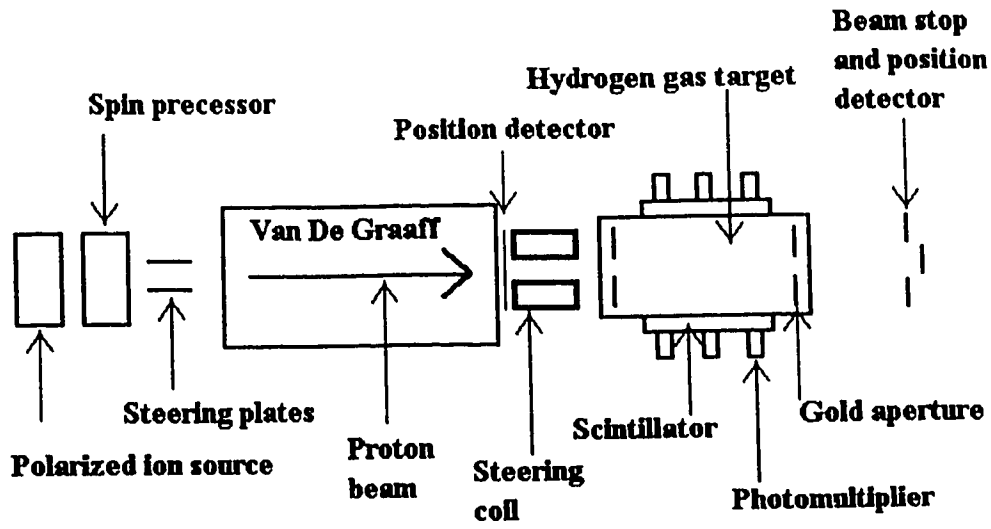


Figure 2.2a: The experimental setup for the LAMPF 15 MeV parity violation experiment. The scattered protons were detected in scintillators while a beam stop was used to detect the transmitted protons.

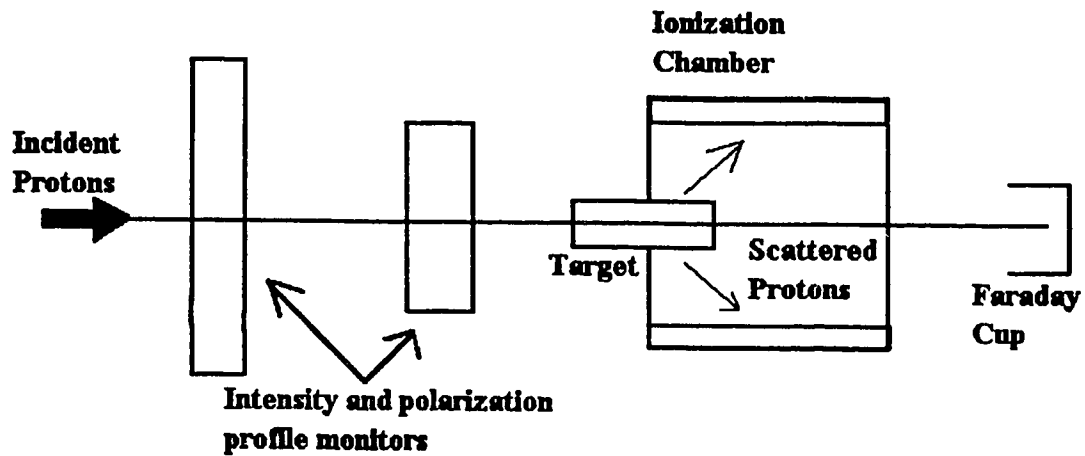


Figure 2.2b: The experimental setup for the PSI parity violation experiment. The scattered protons are detected in an ionization chamber while a faraday cup is used to detect the transmitted protons.

15 MeV. The experimental setup is shown in figure 2.2a. The protons were scattered by a 3 atmosphere  $H_2$  gas target. These scattered protons were detected in four scintillators, which were arranged like the four walls of a box. The transmitted protons were detected in a beam stop. To correct for beam size errors, two fast steering systems were used. One system used the steering plates with position detector after the accelerator (shown in figure 2.2a). The other system used the steering coil and the beam stop, which was divided up into center plate and four outside quadrants. The helicity of the beam was flipped at a rate of 1 kHz. The final result, which is in the table above, only includes statistical error. The systematic error was estimated to be small.

The most precise measurement was done at PSI<sup>9</sup> and was done with the precision of a swiss watch. The polarized beam was produced by an atomic beam polarized ion source at the PSI injector cyclotron. This beam was about 3 to 4  $\mu A$  of current with  $83 \pm 2\%$  polarization. Figure 2.2b shows the schematic set up. The proton's helicity was reversed nominally every 30 ms. The first 20 ms of this time was used to find the fraction of the beam which was scattered. This was done by taking the ratio of the signals from the ionization chamber (which detects the scattered protons) to the signal from the Faraday cup (which detects the transmitted protons). To determine the polarization profile of the beam, polarimeters were used. These polarimeters were made up of two wheels with 2 graphite strips on each wheel. These graphite strips were moved through the beam by the use of stepping motors. The scattered protons from these graphite targets were detected in 4 scintillation



detectors. This detection gave a clean separation of elastic and inelastic scattering in graphite. Now since the  $p + {}^{12}\text{C}$  reaction has a large transverse analyzing power ( $\approx .93$ ), information on both the beam intensity profile and the beam polarization profile were found. The most time consuming part of this experiment was the minimization of the systematic errors. The results of from this experiment are in agreement with the results from the experiments done at Berkeley<sup>2</sup> and Texas A&M<sup>2</sup>.

The 800 MeV experiment<sup>11</sup> at LAMPF was a transmission experiment. The experimental setup for this measurement is shown in figure 2.2c. The transmitted protons before and after the liquid hydrogen target were measured in this experiment because the number of scattered protons was large in comparison to low energy experiments. This measurement was accomplished by use of two main ionization chambers. To correct for beam size problems, multiwire chambers were used to measure the beam position and profile. The beam position was stabilized by using position signals from split plate ionization chambers. Polarimeters and a  $\text{CH}_2$  scanning polarimeter were used to measure false asymmetries due to polarization effects. The TRIUMF 230 MeV experiment is still in the preparation stage and it will be described next.

The TRIUMF experiment will measure  $A_z$  to an accuracy of  $\pm 2 \times 10^{-8}$ ; theory predicts that  $A_z$  will turn out to be  $5 \times 10^{-8}$ . The motivation for doing this experiment is to determine as absolutely as possible the  $h_p$  contribution to  $A_z$ . This measurement of the  $h_p$  contribution relies on the fact that the p-p weak coupling constant  $h_p$  is dominant at an energy of 230 MeV. The measurement will determine

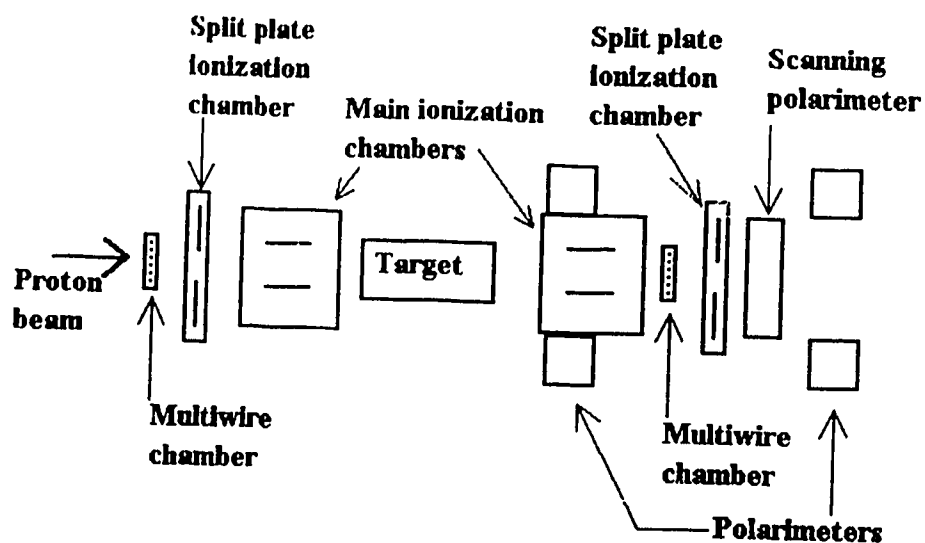


Figure 2.2c: The experimental setup for the LAMPF 800 MeV parity violation experiment. The transmitted protons were measured before and after the liquid hydrogen target by two ionization chambers.

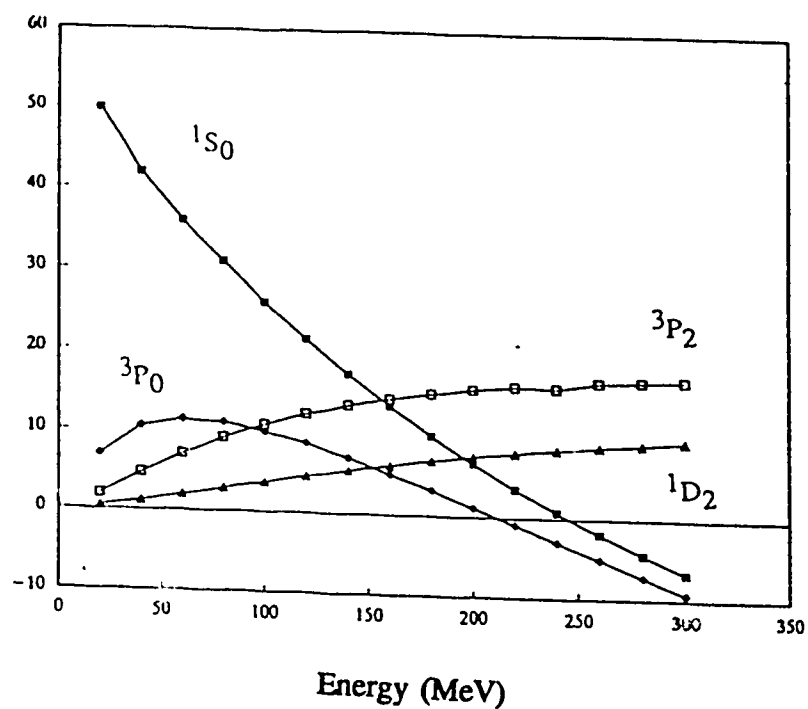


Figure 2.3: The phase shifts for the proton-proton interaction.

$h_p$  to  $0.12 \times 10^{-6}$  which is 10% of the DDH best value, and will determine  $h_w$  to  $0.15 \times 10^{-6}$ , which is 50% of the DDH best value. The energy of 230 MeV was chosen because  $A_z$  is dominated by  $h_p$  at this energy. This situation is different at 15 MeV where  $h_p$  and  $h_w$  have equal importance. At 230 MeV the mixing of S and P partial waves passes through zero. Figure 2.3 shows that the phases in the  $^1S_0$  and  $^3P_0$  partial waves go through zero near 230 MeV. This last statement implies that P-D partial wave mixings are dominant. P-D partial wave mixings have a small  $h_w$  component, which implies that the P-D is mostly due to  $h_p$ . At the lower energies like 15 and 45 MeV, the S and P mixing doesn't cancel and therefore  $A_z$  is due to both  $h_p$  and  $h_w$ .

The experimental apparatus is shown in figure 2.4. In this apparatus the longitudinally polarized beam will pass through fast steering magnets first. These magnets will center the beam to within  $\pm 10 \mu\text{m}$ . This centering by the fast feed back loop, in which the intensity profile monitor sends a signal to an amplifier which powers aircore steering magnets, which then steer the beam. Figure 2.5 shows the motion of the beam's centroid with the fast feed back loop on and off. As seen in the figure, the loop works quite well. The figure also shows a beam intensity profile. The profile monitors achieve these two functions by the use of an effect called secondary electron emission. The plates used for the fast feedback loop are shown in the figure as the split plate pack. The plates used to measure the intensity profile of the beam are shown as the x-y harp pack.

In order to determine the beam polarization profile (to account for the circulating polarization) two polarization profile monitors will be used. The TRIUMF

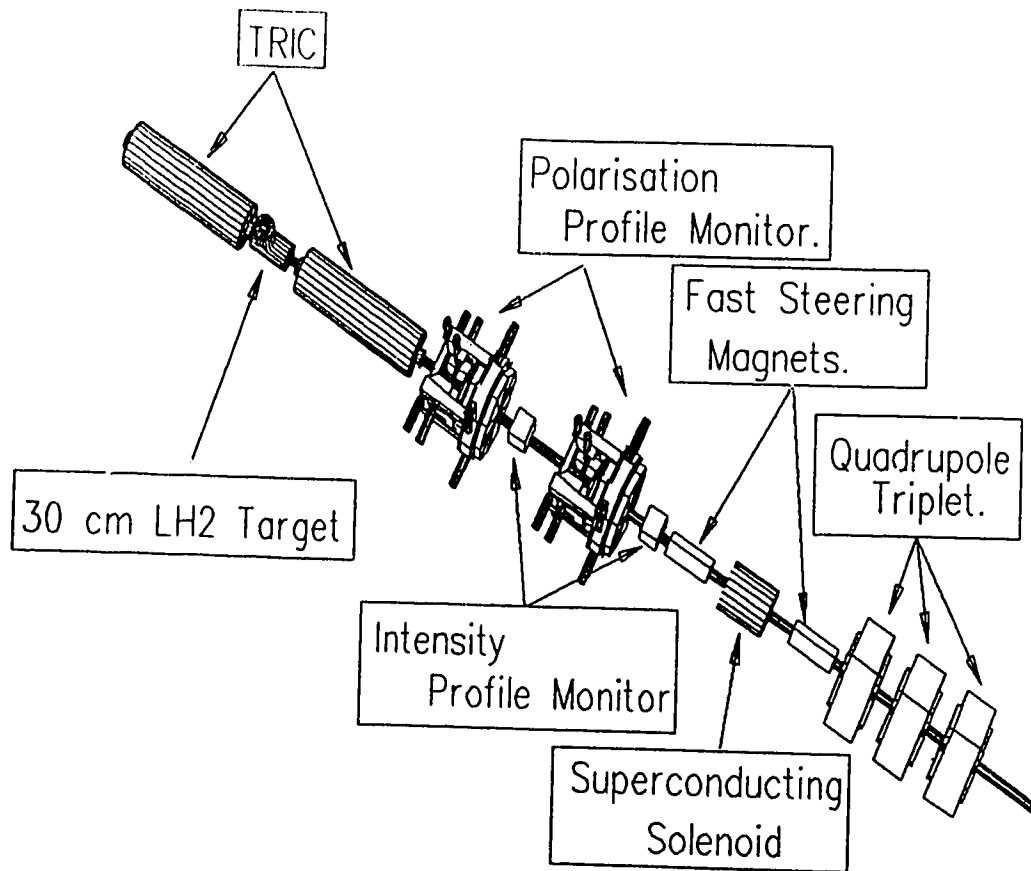


Figure 2.4: The apparatus for the TRIUMF parity violation experiment. The beam is going from right to left. The intensity profile monitors and the fast steering magnets are used to center the beam. The polarisation profile monitors measure the amount of circulating transverse polarisation. Then the beam is measured by two transverse field ionization chambers (TRICs) before and after the liquid hydrogen target.

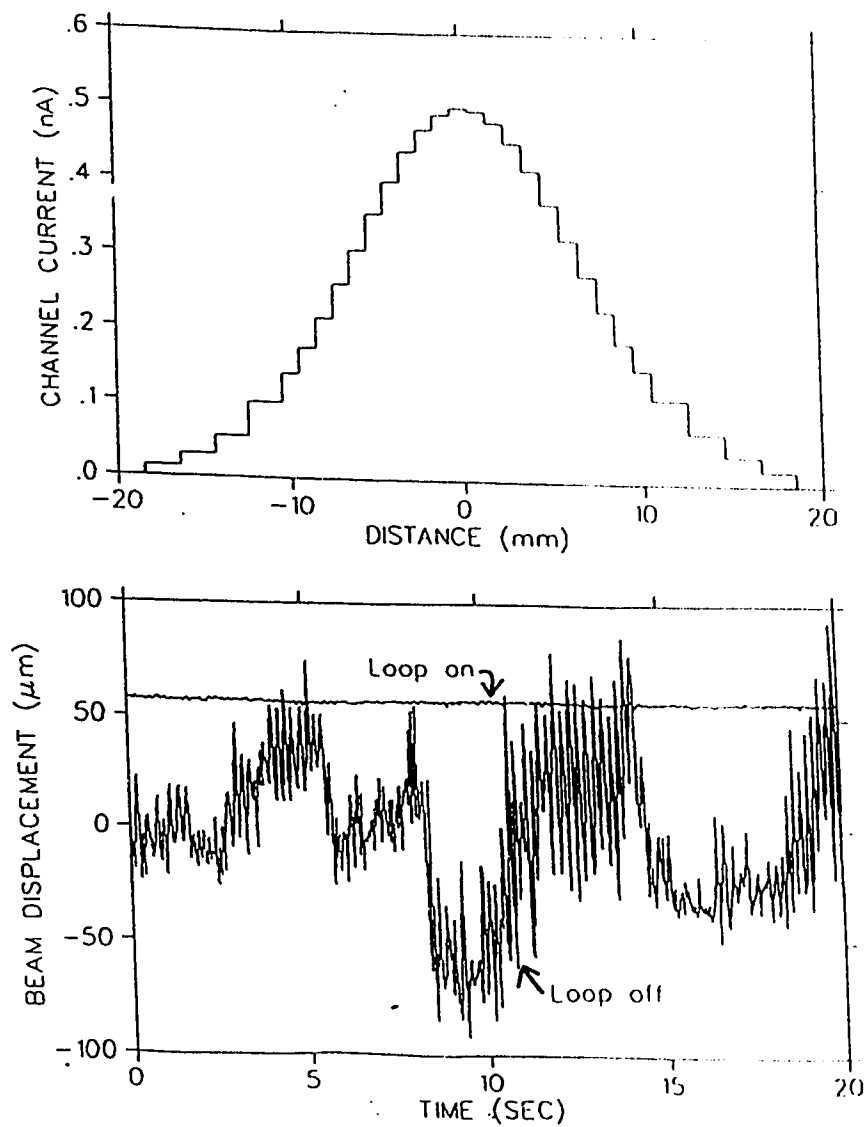
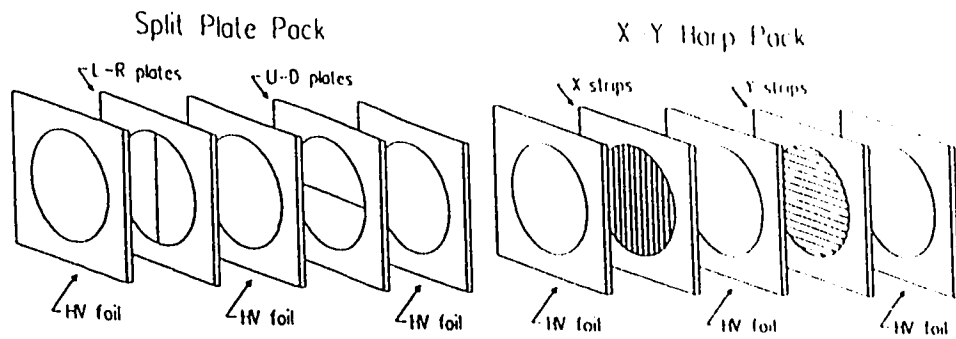


Figure 2.5: From top to bottom: the plates used in the beam profile monitor, a beam profile, and a comparison of the beam displacement when the fast feedback loop is on and off.

polarization profile monitors use hydrogenous (high density polyethylene) blades instead of carbon blades as used in the PSI experiment. The protons which scatter and recoil off of these blades are measured in coincidence by scintillation detectors, to discriminate against (p, 2p) events from carbon.

The target which will be used for this transmission experiment will be a 40 cm  $\text{LH}_2$  target. The measurement of  $A_z$  will be done by two transverse field ion chambers (TRICs). These TRICs have been designed to deal with noise due to spallation, delta rays, space charge, attachment and recombination all of which will be described below in chapter 3.

At present one polarization profile monitor is built and running. The last test run (March 1992) shows encouraging results, namely that the polarization profile monitors are well understood. The intensity profile monitors have been built and tested. They work well, but have a few small technical problems that have yet to be ironed out. This parity experiment does not have its own beam line at TRIUMF yet. However, there will be a new beam line built in the fall of 1993 for this experiment.

Finally, how well does the theory predict the values in table 2.2? Figure 2.6 shows the fits to the experimental data. At low energies Driuoli and Miller<sup>13</sup> as well as Iqbal and Niskanen<sup>14</sup> used meson exchange models. These models do not fit the high energy data point because meson exchange potentials tend to break down around 1 GeV. Knowing this fact, Goldman and Preston<sup>15</sup> used a quark model calculation to examine the parity violating asymmetry at higher energies. From Figure 2.6 it can be seen that the low energy calculations fit the data reasonably well; similarly, the higher

energy calculation fits the high energy data point.

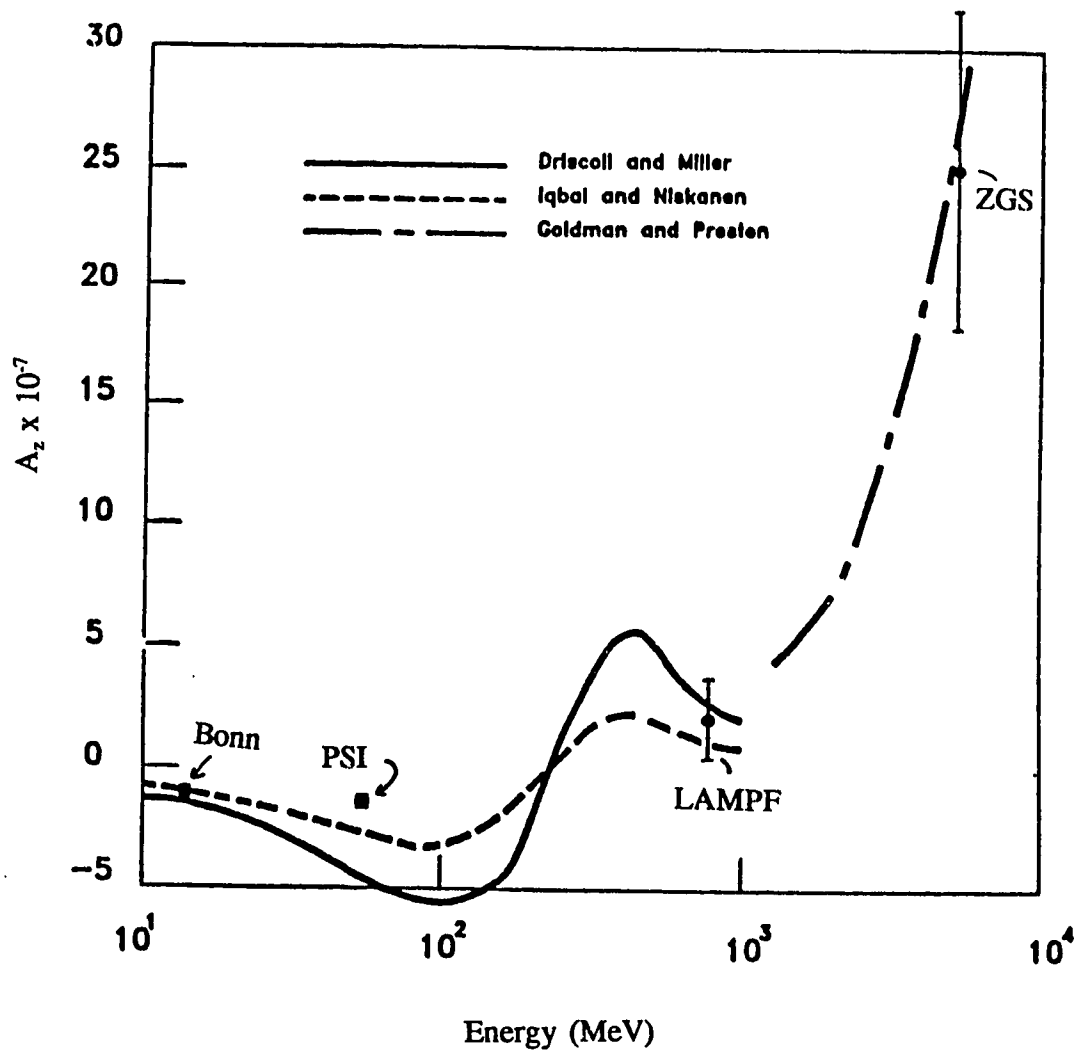


Figure 2.6: Theoretical predictions for  $A_z$  compared with data from the Bonn, PSI, LAMPF, and ZGS experiments.

### 3 Ionization Chambers

As mentioned in the last section the primary measuring devices for the 230 MeV experiment will be the transverse field ionization chambers (TRICs), which are parallel plate ionization chambers. A Parallel plate ionization chamber can be thought of as a parallel plate capacitor which has a gas between the plates. As shown in figure 3.1 the top plate has negative high voltage applied to it. The bottom plate is usually segmented into guard plates and the collector plate. The guard plates are there to ensure that the fringing field effects do not affect the electrons travelling to the collection plate. The gas between the two plates becomes ionized once the beam passes between the two plates; the positive ions go to the high voltage plate and the electrons are collected on the collection plate. The electrons are collected instead of the ions because the electrons move faster in the electric field. These collected electrons will result in a current which is proportional to the number of ion pairs produced in the gas, which in turn is proportional to the energy deposited by the incident radiation.

Figure 3.2 shows the ion chamber's signal dependence on the applied voltage. In the first section of the curve the applied voltage is low enough that the ions have enough time to recombine back into neutral atoms. As the voltage is increased in this section, the velocity of the electrons and ions increase, which leaves less time for the electron ion pairs to recombine.

As the voltage is increased further recombination losses become negligible. This region of the curve is called the ionization chamber region. While the number



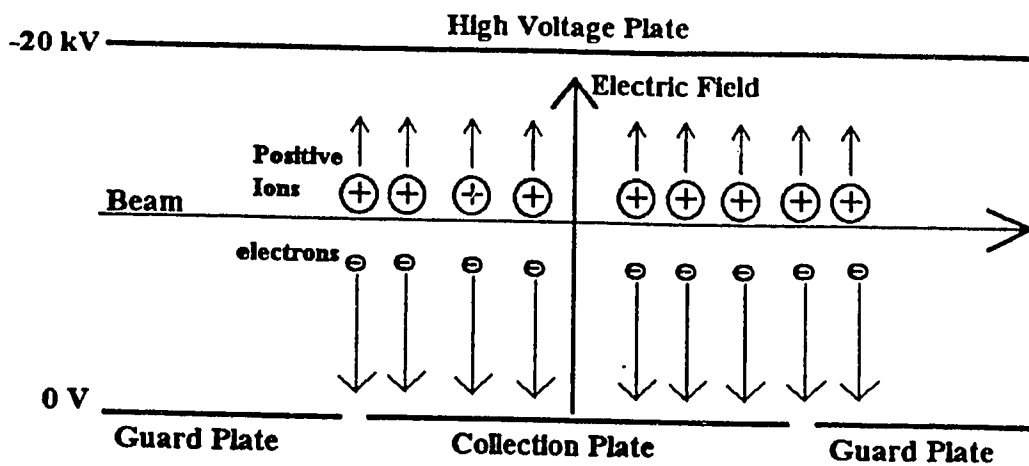


Figure 3.1: The basic parallel plate ionization chamber. The beam ionizes the gas. The electrons from this ionization travel to the collection plate. The guard plates are there to minimize the edge effects of the electric field.

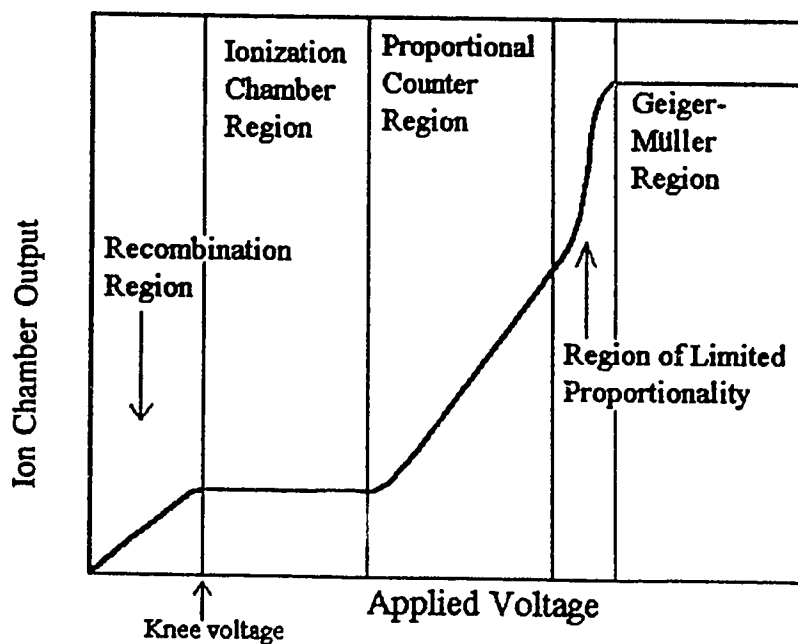


Figure 3.2: The ion chamber's dependence on the applied voltage.

of ion pairs is independent of the applied voltage in this region of the curve, the amount of charge collected is proportional to the number of ion pairs created. In fact, the number of ion pairs produced and collected is proportional to the number of particles passing between the plates and the amount of energy these particles have deposited. These two sections of the curve will be collectively referred to as the plateau curve.

If the voltage is increased above the ion chamber region, then the electrons which have been freed have enough energy to ionize more atoms. This region is the proportional counter region, where gas multiplication takes place. Here, gas multiplication is linear, and the pulse size proportionality to the initial ionization is conserved. As the voltage is increased even further, nonlinear effects are introduced. These nonlinear effects are due to space charge effects which cause the electric field within the plates to get distorted. This region is the region of limited proportionality.

Eventually as the voltage is increased, the pulse size proportionality completely breaks down, and the pulse size becomes independent of the initial ionization. In this region secondary electron avalanches occur. These avalanches are caused by photons which have been emitted by excited atoms. The photons can travel large distances in the chamber, so in a sense the whole chamber participates. Therefore information about the deposited energy of the particle can not be measured, since all incident particles produce identical output pulses. This region of the curve is known as the Geiger-Müller region of the curve.

The region that is used by ionization chambers is the ionization chamber

region. In this region, the current signal measured by the chamber is proportional to the rate of arrival of the incident radiation and the amount of energy deposited by this radiation.

### 3.1 The Transverse Field Ionization Chambers

The transverse field ionization chambers (TRICs) will be run at -20 kV, which is applied to the top plate. There have been problems with discharges from this top plate; these problems are discussed in appendix A. Below this high voltage is a stack of side electrodes. Each of these side electrodes decrease in voltage by 1 kV per electrode till they reach the bottom plate which is at ground. The voltage on each plate is decreased by the use of a resistor chain. These side electrodes are used to shape the electric field to prevent space charge distorting the chamber's electric field. This space charge will be examined more closely in section 3.6, below. Figure 3.3 shows a beam's view of this plate assembly. The gap between the high voltage plate and the ground plate is 10 cm. This ground plate is segmented into seven collection plates which are shown in figure 3.4. The side collection plates measure the beam's halo. The triangular collection plates measure the beam alignment. Whereas the center plate is used together with the rest of the plates to measure the beam current during data taking.

The gas that will be used in the chamber will be 250 torr of hydrogen.

Appendix B has information on the precautions taken when the TRIC has been filled

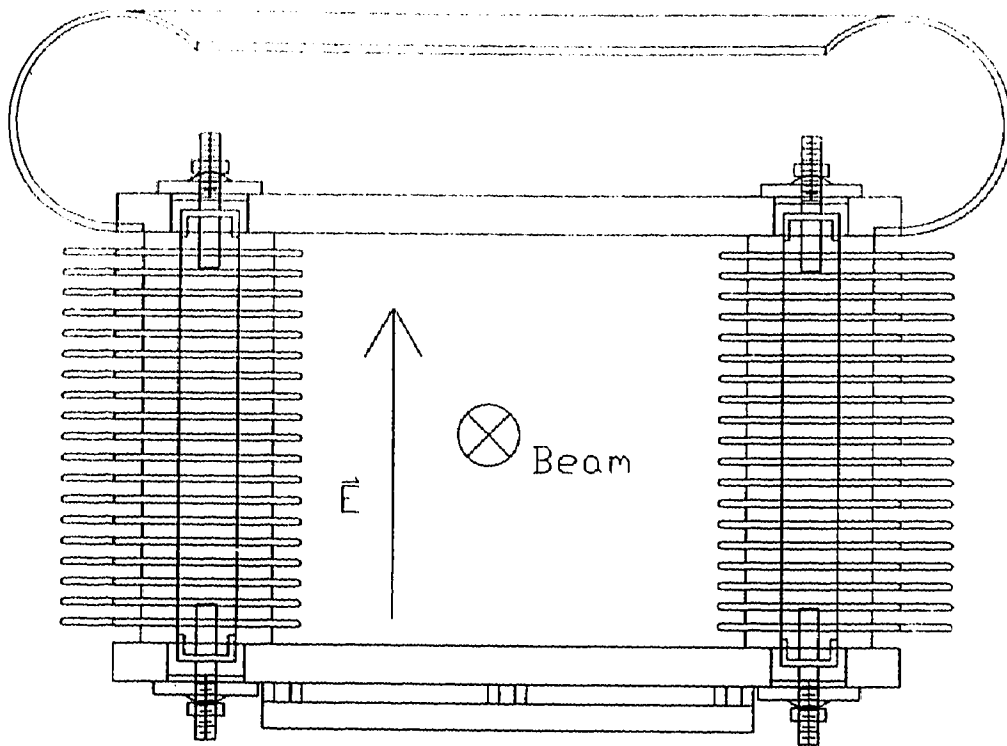


Figure 3.3: A beam's eye view of the TRIC plate assembly. The side electrodes increase by 1 kV per plate (from bottom to top). These electrodes are used to reinforce the electric field along the sides.

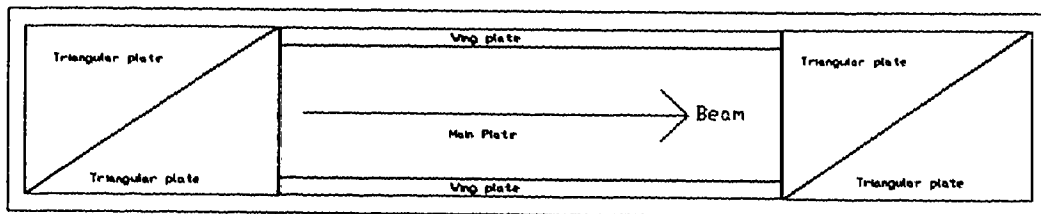


Figure 3.4: An above view of the seven collection plates of the TRIC. The triangular plates are used to measure beam alignment, the main plate is used for data taking and the wing plates measure the amount of halo.

with hydrogen. By knowing that the energy loss<sup>16</sup> of 200 MeV protons in hydrogen gas is 9 MeV cm<sup>2</sup>/g and that it takes 37 eV to produce one ion pair in hydrogen gas, it can be determined that at a pressure of 250 torr the gas gain of the TRIC is 7 ion pairs per cm of collection plate traversed. So for all the collection plates tied together (60 cm), the gas gain is 420 ion pairs. So if a beam of 500 nA is shot through the TRIC, the signal measured from all the plates tied together is 0.21 mA.

To insure the purity of the hydrogen gas, the chamber will be baked to 150 °C and evacuated, before the hydrogen is introduced. Appendix B has the details of the bakeout of the TRIC.

The outer casing of the TRIC is shown in figure 3.5. This casing has feedthroughs for two pressure gauges: an ion gauge to measure the pressure during evacuation and baking, and a transducer gauge to measure the pressure once the hydrogen is introduced into the chamber. These two gauges measure different pressure ranges. The ion gauge is sensitive to a range of pressures from  $5 \times 10^{-2}$  torr to  $4 \times 10^{-10}$  torr (in air), where as the transducer gauge measures from 1 torr to 1000 torr. Some of the other feedthroughs are the -20 kV high voltage feedthrough, the segmented collection plate signal feedthrough, a view port, and a feedthrough for an optional getter. The flanges for the beamline connections are also shown. These flanges are not exactly as shown in the diagram. For the upstream TRIC, the downstream flange has been moved to the downstream wall of the chamber. Whereas the downstream TRIC has had its upstream flange moved to the upstream wall of the chamber. These changes have been done to facilitate the connections with the liquid

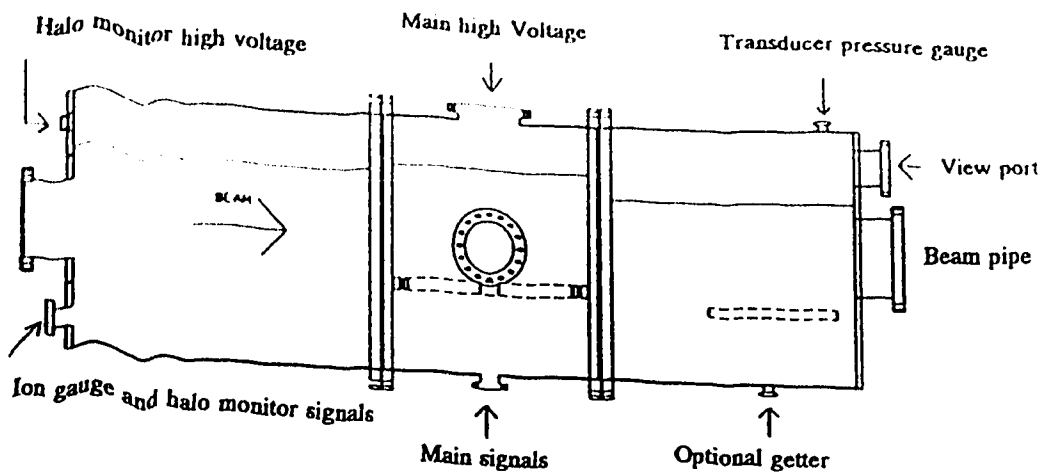


Figure 3.5: The outer casing of the TRIC, indicating all the feedthroughs.

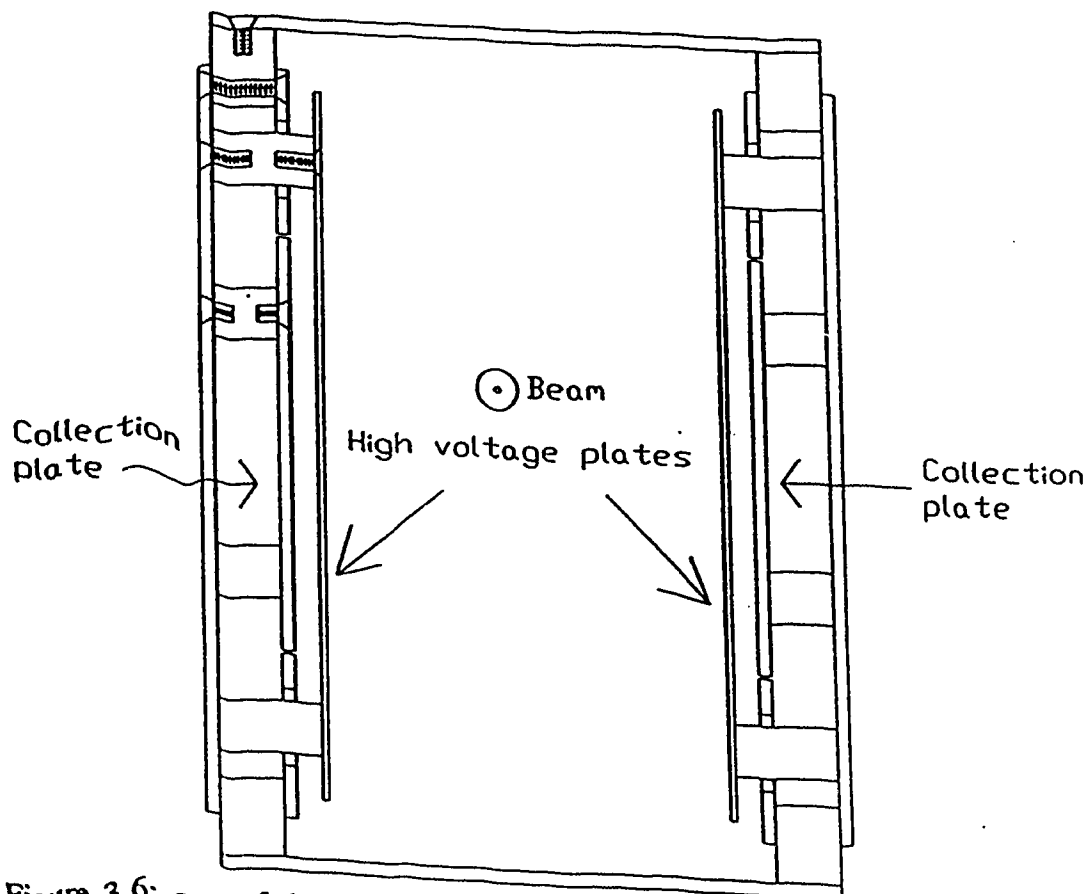


Figure 3.6: One of the two assemblies that make up the halo monitor. The shown assembly is made up of two small ion chambers.

hydrogen target. There is also a high voltage feedthrough and a signal feedthrough for the halo monitor.

The halo monitor is located in the upstream end of the TRIC. The halo monitor is made up of two of the assemblies shown in figure 3.6. These two assemblies are mounted perpendicular to each other. The halo monitor is made up of four small ionization chambers (top, bottom, left and right). These halo monitors are run at 500 V and have a gap of 6 mm between the high voltage and collection plates. These halo monitors measure the beam between 5.2 cm and 5.8 cm from the center of the beam. The purpose of these halo monitors is to evaluate how much beam is hitting the main plate assembly, thereby indicating the degree of spallation products. The gas gain of the halo monitor running in 250 torr of hydrogen gas is 18 ion pairs per proton.

Currently there are two TRICs (TRIC 1 and TRIC 2) that have 10 cm gaps between the high voltage and collection plates. TRIC 1 has been tested in the beam, with a halo monitor. TRIC 2 has only been used in high voltage tests so far. It has been proposed that TRIC 2 should not have a halo monitor put into it due to the problems (see section 5.1) that have been found with the TRIC 1 halo monitor. A third TRIC (TRIC 3) has been proposed to have a 15 cm gap between the high voltage plate and the collection plate. This third TRIC would replace the downstream TRIC in the beamline. The reason for changing the gap on the downstream side of the target is due to a beam breathing effect. This beam breathing effect occurs when the beam changes its crosssectional area between the upstream TRIC and the

downstream TRIC. This effect would cause one of the two TRICs in the beamline to miss some of the beam that the other TRIC has seen. If this effect is at all correlated to spin flip, it would be a false parity violation signal. So by enlarging the downstream TRIC, this effect will not affect the results of the experiment. This beam breathing effect is not measurable in the present parity experimental set up.

### 3.2 Attachment

Now that the ion chamber has been described, the physical effects on its performance can be examined. The first of these effects that will be looked at is attachment. Attachment occurs when the electron from the ion pair attaches to a neutral atom and forms a negative ion. This negative ion has more mass than the electron, so the ion will move slower in the electric field of the chamber. Since this negative ion moves slower than the electron, the ion will not be collected at the same time as the electron. Therefore part of the signal from the ion pairs produced by the incident radiation will be lost or misplaced in time.

To get an idea of the effect of attachment, the attachment coefficient must be looked at. Price<sup>17</sup> defines the attachment coefficient,  $h$ , as the probability of attachment per electron and neutral ion collision. The value of attachment coefficients depend largely on the type of gas inside the ion chamber and the amount of impurities in the gas. The attachment coefficient also depends on the pressure of that gas and on the energy of the electron from the ion pair. The value of  $1/h$  can be thought of as



the number of collisions with neutral atoms required for an attachment to occur. To minimize the noise in the chamber due to attachment,  $1/h$  should be as large as possible in comparison to the number of collisions the electron makes before it hits the collection plate. Below is a table of attachment coefficients for various gases:

Table 3.1: Attachment coefficients for various gases.

Gas	Attachment coefficient
halogen gases	$10^{-3}$
O <sub>2</sub> and water vapour	$10^{-4}$
Ar, H <sub>2</sub> , N <sub>2</sub> , CO <sub>2</sub> , methane, ammonia	$10^{-6}$ or smaller

From the above table it can be seen that halogen gas, O<sub>2</sub>, and water vapour impurities should be minimized inside the ionization chamber. Price<sup>17</sup> recommends that the amount of O<sub>2</sub> in an ion chamber should be less than 50 parts per million. Attachment is dealt with by using ultra high purity hydrogen inside the TRICs. By evacuating and baking the TRIC before the hydrogen introduced the contaminants in the TRIC are minimized. The inside surfaces of the TRIC has also been electropolished and cleaned with methanol during its construction in a clean room.

### 3.3 Recombination

Another factor that influences the performance of the TRIC is recombination. Recombination happens when the ion pairs are close enough that they have the ability to recombine and form a neutral gas molecule. In order to estimate if recombination

is a problem the velocity of the electrons and of the positive ions can be examined.

Sharpe<sup>18</sup> gives velocities of the electrons and ions as:

$$\begin{aligned} v(e^-) &= \mu_- \sqrt{\frac{V}{pd}} \\ v(ion) &= \mu_+ \frac{V}{pd} \end{aligned} \quad (3.1)$$

where  $V$  is the applied voltage on the chamber,  $d$  is the distance between the plates,  $p$  is the pressure in atmospheres,  $\mu_-$  is the electron mobility, and  $\mu_+$  is the positive ion mobility. Sharpe<sup>18</sup> gives  $\mu_-$  as  $5 \times 10^4 \text{ cm}^{3/2}/V^{1/2}\text{s}$  and  $\mu_+$  as  $14 \text{ cm}^2/V\text{s}$  for hydrogen. So by using the pressure as  $1/3$  of an atmosphere, the plate gap as  $10 \text{ cm}$ , and the voltage as  $20 \text{ kV}$ , then the velocities are found to be  $3.9 \times 10^6 \text{ cm/s}$  for electrons and  $6.0 \times 10^3 \text{ cm/s}$  for the positive ions. Given the large difference in the velocities it would be thought that the losses due to recombination are small. To be sure, the fractional loss due to recombination will be looked at. Sharpe<sup>18</sup> gives the fractional loss for a parallel plate ion chamber as:

$$f = \frac{\alpha N d^{g+3}}{\mu_+ \mu_- V^{g+1}} \quad (3.2)$$

where  $\alpha$  is the recombination coefficient,  $N$  is the number of ion pairs per  $\text{cm}^3$  per

second, and  $g$  is an exponent depending on the type of gas within the chamber.

Sharpe<sup>18</sup> gives the value of  $10^{-10}$  for  $\alpha$ , if the objects recombining are electrons and positive ions and a value of  $10^{-6}$  for  $\alpha$  if the two objects recombining are negative and positive ions. He also gives limits for  $g$  as 1 for air and 0.5 for argon; he does not give a value for  $g$  for hydrogen. So it is assumed that the value for  $g$  for hydrogen is within these two values.

So by knowing the gas gain of the chamber, assuming that the beam has a 1 cm radius, using an applied voltage of 20 kV, and a pressure of 1/3 of an atmosphere, the fractional loss due to recombination is found to be within  $1.1 \times 10^{-6}$  (using 0.5 for  $g$ ) and  $2.5 \times 10^{-8}$  (using 1 for  $g$ ).

### 3.4 Spallation Noise

Another effect that introduces noise into the chamber is spallation. Spallation occurs when the proton beam hits a nucleus and the nucleus gives off nuclear fragments. These fragments can introduce noise into the TRIC because these large fragments tend to ionize more gas than the protons from the beam. Spallation is a random process, so it tends to introduce large random signals into the TRIC output. There are three places in the TRIC that are possible sources of this type of noise. The first is the gas used inside the ionization chamber. If this gas was composed of heavy elements, then there would be spallation noise from this gas. However, hydrogen gas will be used. Since hydrogen gas cannot produce spallation fragments,

spallation noise from the gas inside the TRIC is eliminated.

The second place that spallation can occur is from the plate assembly used to detect the protons. This source of spallation noise has been minimized by having the ion chamber electric field transverse to the beam, instead of having the field parallel to the beam. By using this configuration, the less of the beam hits the collection plates and therefore less spallation fragments are produced.

The third place spallation noise can come from is the windows which separate the gas within the TRIC from the rest of the beamline. To lower the noise from these windows, the distance between the windows and the sense region of the TRIC is 55 cm upstream of the sense region and 45 cm downstream of the sense region. This extra distance between windows and the sense region is then used as a volume to range out the spallation products.

The energy spectra of the fragments produced tend to look like figure 3.7, where  $\sigma$  in this case is the cross section for producing the spallation fragment. This figure has a low energy peak at the most probable emission energy,  $E^*$ , which is independent of the bombardment energy. Kortelling<sup>19</sup> claims that the position of this maximum in the energy spectra, at a given angle, does not change within 1 MeV for bombardment energies of 210 MeV, 300 MeV, and 400 MeV. Kortelling<sup>19</sup> also claims that the maximum in the spectra is due to the Coulomb barrier of the target nucleus and that the position of the maximum is affected very little when the bombardment energy is changed from 200 MeV to 5.5 GeV. Wu<sup>20</sup> claims that the lower energy fragments are nearly isotropic for lighter target nuclei and that these low

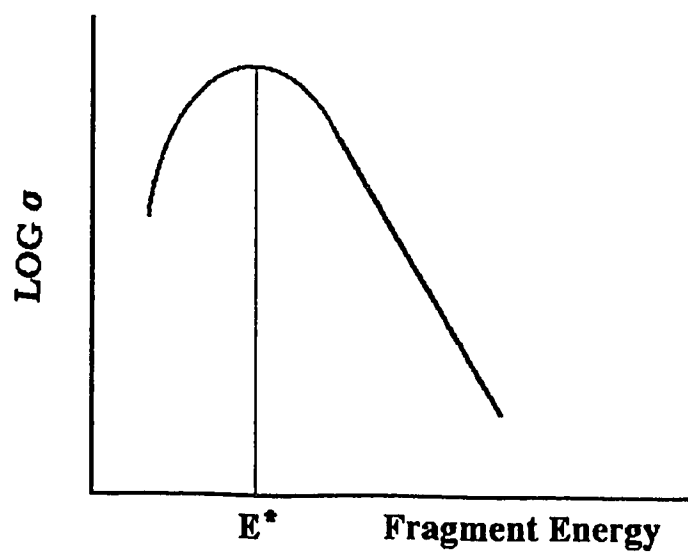


Figure 3.7: The general shape of the energy spectra of fragments produced by spallation.

energy fragments are slightly forward peaked for heavier nuclei. Wu<sup>20</sup> also claims that the high energy fragments are produced mostly at forward angles.

Using the idea that this maximum in the particle spectra does not change from 200 MeV to 5.5 GeV for the bombardment of nickel, the ranges of various spallation products in the TRIC can be estimated by the use of a TRIUMF computer program called LOSSPROG<sup>21</sup>. Nickel is used as an approximation for the stainless steel in the TRIC windows. Below is a table of spallation products and their ranges in 250 torr of hydrogen gas.

Table 3.2: Spallation Product Energies and Ranges.

Product	E* (MeV)	Range in 250 torr of H <sub>2</sub> (cm)	Reference
proton	5	509	20
deuteron	5	290	20
triton	5	209	20
<sup>3</sup> He	12	254	22
alpha	8	98	22
<sup>6</sup> Li	13	75	22
<sup>7</sup> Li	12	58	23
<sup>7</sup> Be	12	33	23
<sup>11</sup> B	12	15	23

The value of E\* was estimated from the energy spectra graphs in the cited references. As can be seen from the table, most of the lighter particles will make it to the active region, but these particles are not as ionizing as the heavier ones. As indicated by table 3.2, any spallation product which is heavier than <sup>7</sup>Li will not make it to the sense region of the TRIC.

By use of a program called SPLAT<sup>24</sup>, the spallation yields from windows have

been estimated. Windows made of 0.002" thick havar (a strong metal) were considered an alternative to the 0.003" thick stainless steel windows, so the SPLAT program was used to compare the spallation yields from the two different windows. This program uses the Silverberg-Tsao<sup>25</sup> semi-empirical cross sections to calculate the spallation yields. The figure 3.8 shows the yields from havar and from stainless steel (which was approximated by iron), for a variety of products. From this graph it is seen that there is very little difference between the havar and stainless steel windows with respect to spallation yield. Since the spallation yields are similar, the noise from these two types of windows should be similar. Figure 3.9 shows how the various elements in havar contribute to the spallation yield. It can be seen from this graph that the heavier elements like Co tend to be a large factor in the total spallation yield.

### 3.5 Noise from Delta Rays

A third source of noise in the ion chamber is delta ray production. Delta rays are high energy electrons (in comparison to the collected electrons) which are a result of a charge particle colliding directly with an electron within an atom. These delta rays have much more energy than the electrons which are usually collected. According to Attix<sup>26</sup>, the maximum energy in MeV that a delta ray can have is:

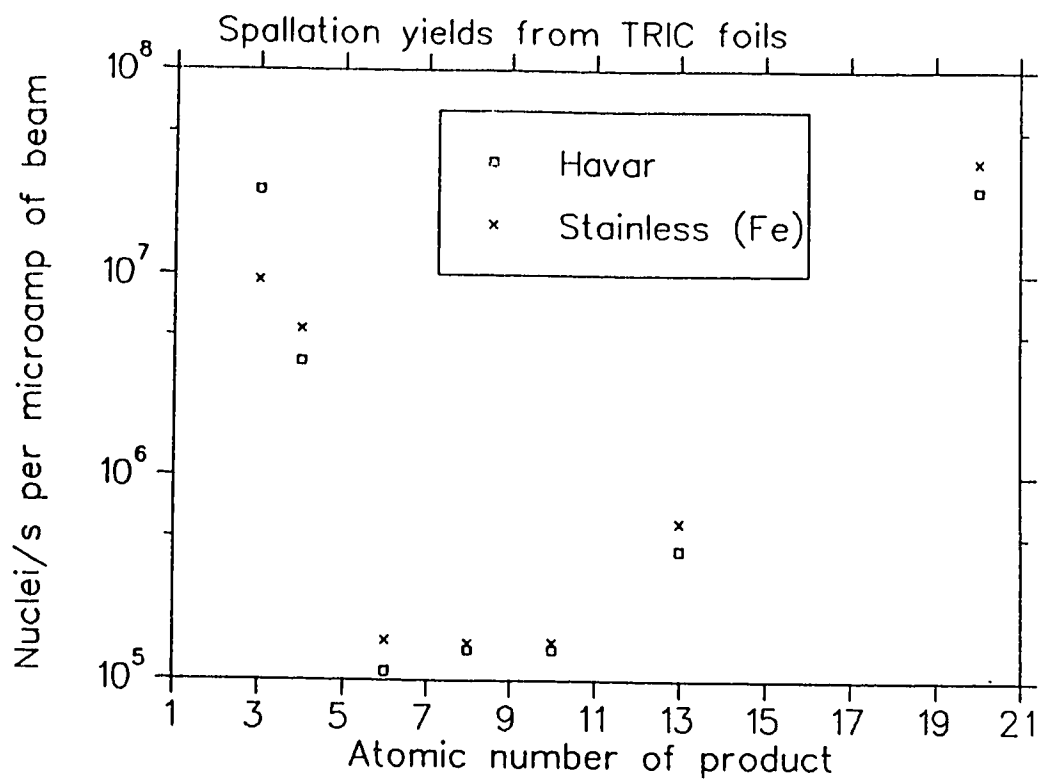


Figure 3.8: Spallation yields from .002" thick havar and from .003" thick stainless steel. There is very little difference between the two yields.



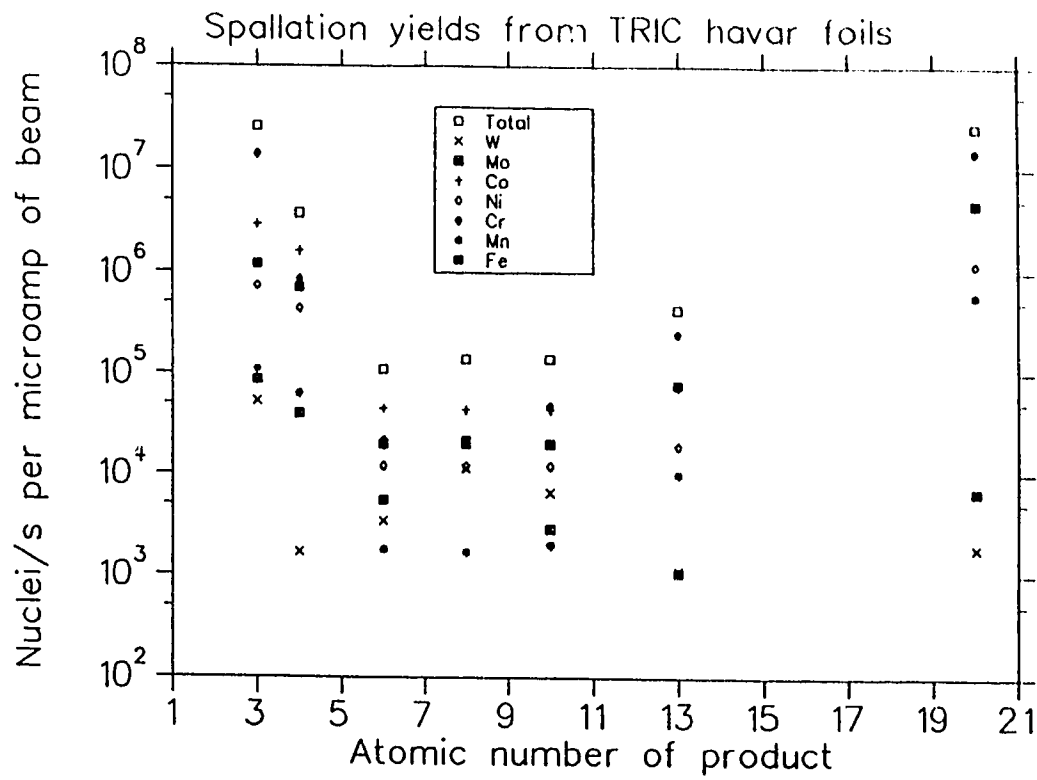


Figure 3.9: How the various elements in havar contribute to the total spallation yield.

$$T_{\max} \approx 1.022 \frac{\beta^2}{1 - \beta^2} \quad (3.3)$$

A 230 MeV proton,  $\beta = 0.595$ , therefore the maximum energy of a delta ray will be 0.56 MeV. This is considerably higher than the 20 keV electron which is usually collected on the TRIC collection plate. These delta rays contribute to the noise of the chamber by ionizing more gas (i.e. a 0.56 MeV delta ray will produce 14 ion pairs in 5 cm of  $H_2$  in comparison to a 230 MeV proton which produces 36 ion pairs in 5 cm of  $H_2$ ). This extra ionized gas will result in a current fluctuation in the TRIC signal. To find a way to minimize the noise from delta rays the number of delta rays produced must be looked at.

To get an idea of how many delta rays are produced in the chamber, the TRIUMF kinematics handbook<sup>16</sup> gives the delta ray production rate for incident protons as:

$$\frac{d^2N}{dxdT} = 0.1535 \frac{z_{\text{med}} \rho_{\text{med}}}{A_{\text{med}}} \frac{z^2}{\beta^2} \frac{F}{T^2} \quad (3.4)$$

$$F = 1 - \beta^2 \frac{T}{T_{\max}} + \frac{1}{2} \frac{T^2}{(T_{\text{inc}} + m_{\text{inc}} c^2)^2}$$

where  $\rho_{\text{med}}$  is the density of the medium,  $T$  is the kinetic energy of the delta ray (in MeV),  $z_{\text{med}}$  is the atomic number of the medium,  $A_{\text{med}}$  is the atomic mass number of the medium,  $Z$  is the atomic number of the incident particle,  $T_{\text{inc}}$  is the kinetic energy

of the incident particle,  $T_{\max}$  is the maximum delta ray energy, and  $m_{\text{inc}}$  is the mass of the incident particle.

The minimum energy of these delta rays can be found by calculating the number of delta rays,  $k$ , which Rossi<sup>27</sup> gives as:

$$j_p = \frac{k}{L} = \frac{.1535r}{\beta^2 I_o} (\log \frac{T_{\max}}{I_o} + s - \beta^2) \quad (3.5)$$

where the theoretical constants are  $r = 0.285$  and  $s = 3.04$  for hydrogen and  $j_p$  is the number of delta rays per unit length of the active volume of the chamber. In equation 3.4,  $I_o$  is the ionization potential (Leo<sup>28</sup> gives it as 15.4 eV), and  $L$  in our case is the length of the active volume in our TRIC. So by also knowing that the number of delta rays is given by integrating equation 3.4:

$$k = \int_{T_{\min}}^{T_{\max}} \frac{dN}{dT dx} dT \approx \frac{0.1535 L \rho_{\text{med}}}{\beta^2 T_{\min}} \quad (3.6)$$

the minimum energy can be found of the delta rays can be found by substituting equation 3.5 into equation 3.6. The above approximation for  $k$ , can be used because the last two terms tend to be smaller than the first term when equation 3.4 is

integrated.

By using equation 3.5 with  $L = 60$  cm, it can be determined that the number of the delta rays produced is 194 per cm inside the TRIC. To get an idea of how much noise is produced by delta rays, the noise factor  $\alpha$  must be looked at:

$$\alpha^2 = \frac{1}{k} \frac{E(\Delta^2) - E(\Delta)^2}{E(\Delta)^2} \quad (3.7)$$

where  $k$  is the number of delta rays produced,  $E(\Delta^2)$  is second moment of the energy distribution of the delta rays, and  $E(\Delta)$  is the average delta ray energy. This noise figure,  $\alpha$ , is the same as the measured  $\alpha$  in section 4.2, except the  $\alpha$  defined by equation 3.7 is only due to delta rays. This noise figure  $\alpha$  is intrinsic chamber noise relative to noise from proton statistics. The average of the energy distribution of the distribution is given by:

$$E(\Delta) = \frac{1}{k} \int_{T_{\min}}^{T_{\max}} \frac{0.1535 L \rho_{med}}{\beta^2} \frac{dT}{T^2} \Delta(T) \quad (3.8)$$

The second moment of the delta ray energy distribution is given by:

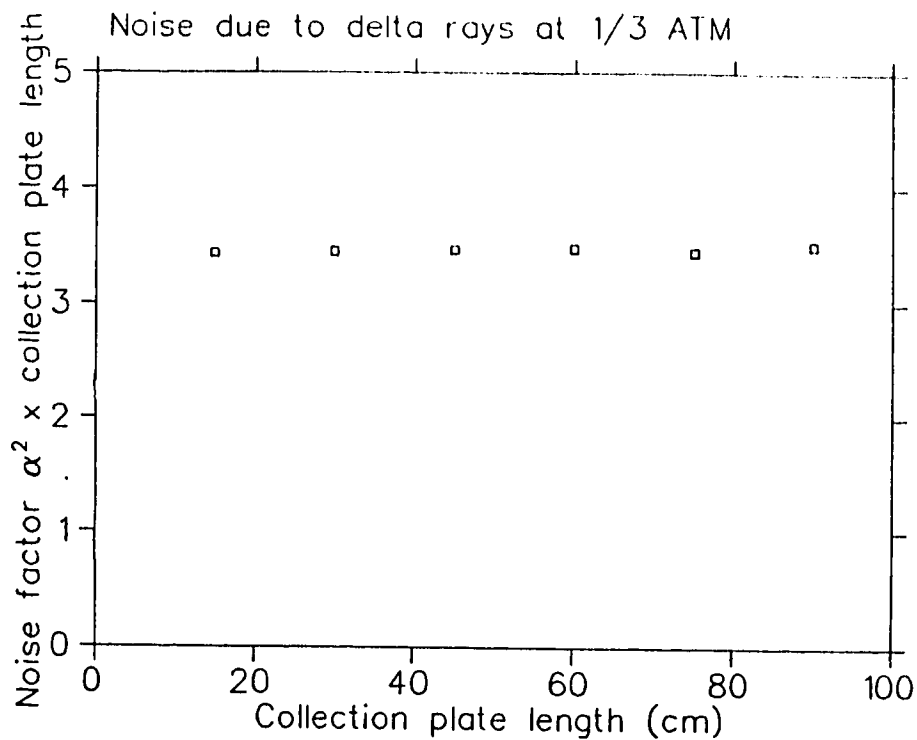


Figure 3.10: The noise from delta rays tends to go like the inverse of the collection plate length.

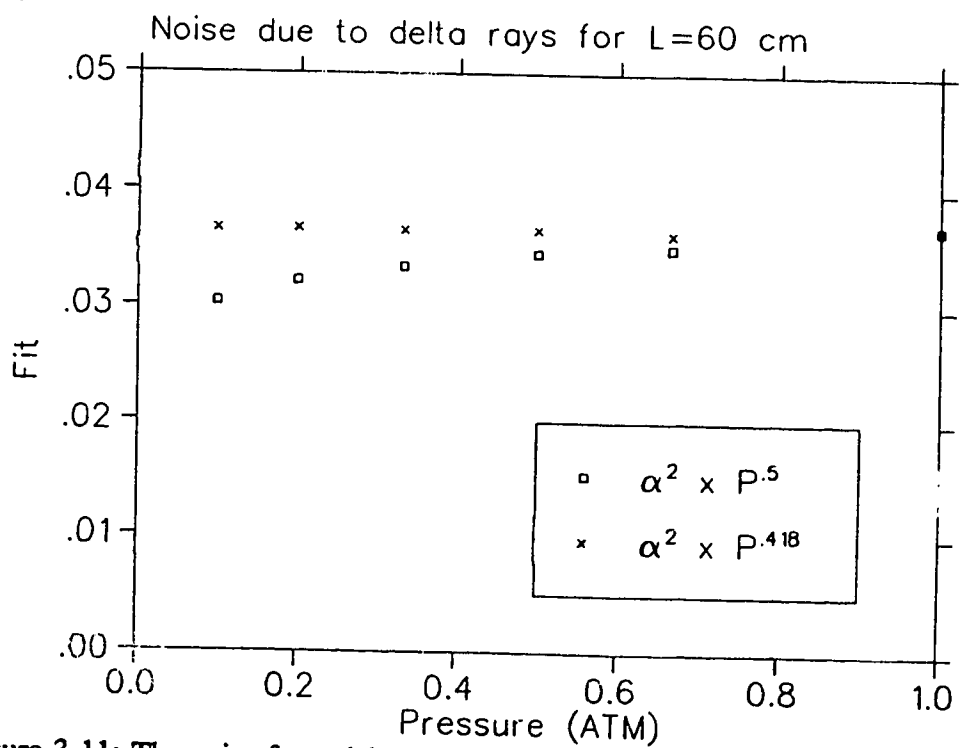


Figure 3.11: The noise from delta rays tends to go like  $P^{-0.418}$  and not like  $1/\sqrt{P}$ , where  $P$  is the chamber pressure in atmospheres.

$$E(\Delta^2) = \frac{1}{k} \int_{T_{\min}}^{T_{\max}} \frac{0.1535 L \rho_{med}}{\beta^2} \frac{dT}{T^2} \Delta^2(T) \quad (3.9)$$

where  $\Delta(T)$  is the amount of energy deposited by the delta ray within the active region of the chamber. This function  $\Delta(T)$  can be determined by calculating the angle the delta ray is emitted with respect to the incident beam direction. Then by using this angle, the length of the delta ray's path within the active region can be evaluated. Once this range is found, the energy per cm deposited in the active region can be calculated using the fit to experimental data<sup>16</sup> for electron ranges in hydrogen (for electron energies from 0.01 MeV to 0.55 MeV):

$$R = 2434 T^{1.522} \quad (3.10)$$

where  $R$  is in g/cm<sup>2</sup> and  $T$  is in MeV.

Now by using a program called ALPHA<sup>29</sup> which calculates  $\alpha^2$  by the above method,  $\alpha^2$  was calculated for various chamber pressures and for various collection plate lengths. This calculation was done for a beam energy of 230 MeV. This program approximated the TRIC active volume by a cylinder of 5 cm radius and of length  $L$ . Figure 3.10 shows that  $\alpha^2$  tends to go like  $1/L$ . Fitting the collection plate results showed that  $\alpha^2$  goes like  $L^{-.992}$ . Figure 3.11 shows that  $\alpha^2$  tends to go like  $P^{-.418}$  and not like  $1/\sqrt{P}$ . Fitting the chamber pressure results showed that  $\alpha^2$  goes like  $P^{-.418}$ . These calculations implied that the noise from delta rays is reduced if the

collection plate length is increased and if the chamber pressure is increased. The TRIC collection plate length is 60 cm, so that this noise from delta rays is reduced. The TRIC collection plate length was not made any longer due to size restrictions of the beamline and so that the beam size does not change a large amount over the collection area.

### 3.6 Space Charge

Yet another physical effect which occurs inside ionization chambers is space charge. Space charge is a result of the fact that the electrons move about 650 times faster than the positive ions in the gas. This large difference between the velocities implies that the electrons will be collected before the positive ions reach the high voltage plate. So the chamber will have an extra electric field due to the slow moving positive ions. This extra field will do two things to the original electric field. The first thing that it will do is oppose the original electric field. This opposing field will be designated as  $E_1$  is shown in figure 3.12. The second thing that the space charge will do to the original electric field is cause it to bulge out sideways. This sideways effect is also shown in figure 3.12.

To calculate the opposing field,  $E_1$ , the charge density of the electrons can be neglected since the electron velocity is much greater than the positive ion velocity. A simple two dimensional case was looked at, with the center of the two plates being at  $y = 0$ , the collection plate at  $y = -d/2$ , and the high voltage plate at  $y = d/2$ . In this

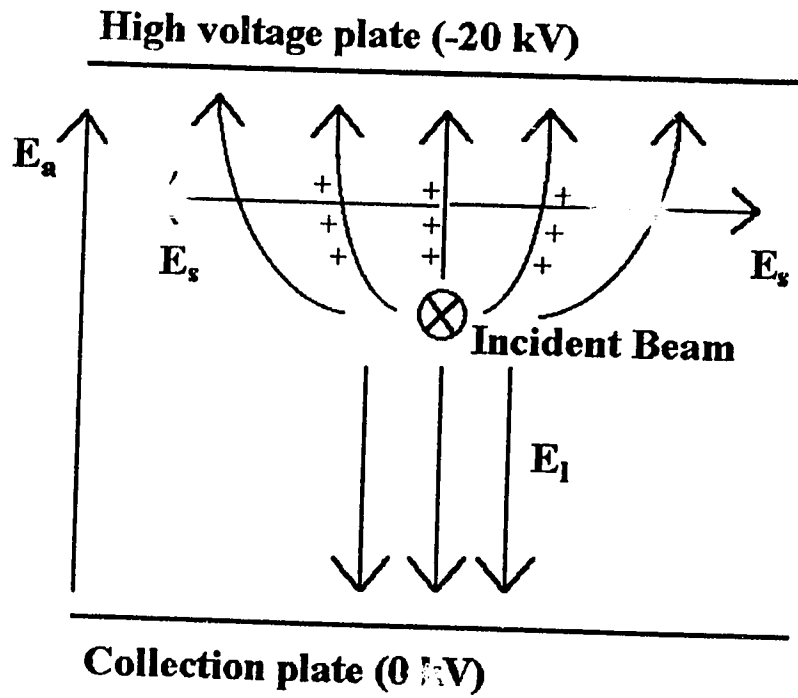


Figure 3.12: The space charge effects are shown. The applied field is denoted as  $E_a$ . The opposing field is shown as  $E_i$  and the sideways field is shown as  $E_s$ .



case Maxwell's equations give:

$$\frac{dE_y}{dy} = \frac{\rho_+}{\epsilon_0} \quad (3.11)$$

Where  $E_y = E_{\text{applied}} + E_i$ ,  $\rho_+$  is the charge density of the positive ions (which is assumed to be constant). By using equation 3.1 for the ion velocity, the current density was found to be:

$$J_y = \rho_+ v_+ = -\frac{\rho_+ \mu_+}{P} E_y \quad (3.12)$$

Where  $P$  is the chamber pressure in atmospheres,  $\mu_+$  is the positive ion mobility.

Substituting equation 3.11 into equation 3.12, it is found that:

$$J_y = \frac{\mu_+ \epsilon_0}{P} E_y \frac{dE_y}{dy} \quad (3.13)$$

However it is also known that the ion current can be written as:

$$J_y = \frac{g P I_b}{w} \quad (3.14)$$

where  $g$  is the gas gain ( $21 \text{ cm}^{-1}$ ),  $I_b$  is beam current,  $w$  is the width of the beam.

Now by putting equation 3.14 and equation 3.13 together and rearranging, it is found:

$$E_y^2 = \frac{2gI_b y P^2}{\mu_+ \epsilon_0 w} \quad (3.15)$$

But equation 3.15 gives:

$$E_y = P \sqrt{\frac{2gI_b y}{\mu_+ \epsilon_0 w}} \quad (3.16)$$

Now since  $E_y = -dV/dy$  and since  $I_b$  and  $P$  do not depend on  $y$ , it is found that  $V$  goes like the square root of the beam current and goes linearly with pressure. This would mean that the knee voltage in figure 3.2 should go like  $P\sqrt{I_b}$ .

If  $E_1$  becomes strong enough, the ions will not move as fast as when  $E_1$  is small. If the charges slow down enough, nonlinear effects from recombination will arise. To minimize this nonlinearity, the TRIC pressure was decreased to 250 torr.

The sideways mechanism was then examined. The charge density of the negative ions within the chamber was neglected, since they travel so much faster than the positive ions. It was assumed that the positive ion charge density  $\rho_+$  is uniform and occupies an area  $w$  by  $d/2$ , where  $w$  is the width of the beam and  $d$  is the distance between the plates in the ion chamber. So  $\rho_+$  was on the upper side of the chamber and occupies an area of  $w$  by  $d/2$ . Now by using equation 3.1, for the

positive ion velocities, the charge density is given by:

$$\rho_+ = \frac{gI_b P^2}{w\mu_+ E_a} \quad (3.17)$$

where  $g$  is the gas gain of the TRIC (21 per cm),  $I_b$  is the beam current,  $E_a$  is the applied electric field, and  $\rho_+$  is the positive ion mobility. So if the positive charge distribution is assumed to be an infinite sheet in the beam direction, then it is known that the electric field on each side of this sheet is given by:

$$E_s \approx \frac{\rho_+}{2\epsilon_0} = \frac{gI_b P^2}{2\epsilon_0 \mu_+ E_a} \quad (3.18)$$

The sideways field should be compared to the applied field:

$$\frac{E_s}{E_a} \approx \frac{gI_b P^2}{2\epsilon_0 \mu_+ E_a^2} \quad (3.19)$$

Now for some value of applied voltage,  $E_s/E_a$  will be the value for the knee voltage.

At this voltage  $E_s/E_a$  will be a constant,  $C$ . In this case  $E_a$  is approximately  $V_{knee}/d$ .

So by rearranging equation 3.19, it was found that:

$$\frac{V_{knee}}{d} \approx \frac{gP\sqrt{I_b}}{C\mu_+} \quad (3.20)$$

From equation 3.20 it would seem that this very simple model predicts that the sideways mechanism goes like the square root of the incident beam current and this mechanism goes linearly with the TRIC pressure. To compensate for this sideways effect, the TRIC has been equipped with intermediate electrodes which are shown in figure 3.3. These side electrodes reinforce the applied field by preventing the bulging of the electric field due to space charge.

From previous measurements, done at TRIUMF, with an ion chamber which was borrowed from the Los Alamos 800 MeV parity violation experiment, it was found that the knee voltage goes like the square root of the beam current and goes linearly with the pressure. It was found that:

$$\frac{V_{knee}}{P\sqrt{I_b}} = 0.72 \pm 0.08 \frac{\text{Volts}}{P(\text{atm})\sqrt{I(\text{nA})}} \quad (3.17)$$

Since the geometry of the Los Alamos ionization chamber is similar to the TRIC, this result can be used to indicate how the two chambers compare in terms of space charge effects.

### 3.7 Summary of Design Considerations

The last few sections have shown that the known effects which contribute to noise have been accounted for. Recombination is not a source of worry, since the recombination of hydrogen is small. Attachment is found to be small as long as the TRIC has very few contaminants. Minimizing these contaminants is done by baking and evacuating the TRIC before the hydrogen is introduced into the TRIC. Noise due to delta rays is reduced by making the sensitive volume of the chamber 60 cm long. Space charge can be reduced by reducing the pressure at the expense of delta ray noise. This choice is justified by the fact that space charge can slow down the collected ions or it can also warp the applied field in such away that some extra ions are collected. To ensure that the field is not warped, intermediate electrodes are used to reinforce the applied field. Noise due to spallation products, is reduced by increasing the distance between the TRIC windows and active volume. This action creates a volume of hydrogen which will range out the spallation products.

## 4 Physical Setup of TRIC Tests

The TRIC was tested at TRIUMF in the 4A beamline, just outside the TISOL confinement area. During these tests a 222 MeV transversely polarized proton beam was used. The beam was transversely polarized so that the TRIUMF ion source group could also do some tests. Note that 230 MeV has often been quoted as the beam energy which will be used in the TRIUMF experiment. It turns out that in the present geometry, 222 MeV is the energy at which the  $h_p$  coupling constant dominates, in a past geometry it was an energy of 230 MeV. If a TRIC with a 15 cm gap is used in the final data taking, another beam energy will have to be selected, since the geometry will have been changed.

The TRIC was tested twice in this beamline, once in September 1992 and once in March 1993. In the first run the TRIC was used in the beamline, with the 4A secondary electron emission current monitor (4ASEM). In the second run the TRIC was tested along with the parity intensity profile monitor (IPM), one air core steering magnet, and the 4ASEM current monitor. The IPM and steering magnet were used for two purposes. The first purpose was to have a monitor with which TRIC could be compared. The second was to use the fast steering magnet and the IPM to center the beam with respect to the TRIC. This centring would then reduce noise from beam wandering. The 4ASEM was also used as a device with which the TRIC could be compared.

Before the first run was started, the TRIC was evacuated for about four days,

by use of a turbomolecular pump. The pressure within the TRIC was measured to be about  $3 \times 10^{-7}$  torr before the TRIC was moved put into the beamline. Once the TRIC was moved into position, it was pumped out again for about 3 hours. Whereas before the second test run, the TRIC was baked for 140 hours as it was evacuated (see appendix C for details on the TRIC bakeout). Again the TRIC was taken to the beamline only after it was baked and evacuated. The pressure within the TRIC before it was put into position was  $6.8 \times 10^{-9}$  torr. This baking was not done in the first test run, because the seals used on the 20 inch TRIC flanges could not hold vacuum at the bakeout temperature. Baking was done before the second run because the original seals were replaced with helicoflex delta seals (a commercially made metal o-ring type seal), which could take the bakeout temperature. For both runs, the TRIC was filled with ultra high purity hydrogen (see appendix B for hydrogen safety details). During the first run, the pressure of this hydrogen was varied (250 torr, 500 torr and 700 torr), whereas for the second run the pressure was not varied and kept at 250 torr.

The voltage applied to the TRIC was also varied due to discharge problems within the TRIC (see appendix C for details). During the first run the TRIC high voltage was varied from -6 kV to -15 kV while the TRIC pressure was 250 torr and was varied from -10 kV to -20 kV when the TRIC was at 500 torr. During the second run the TRIC high voltage was kept at about -13 kV for most of the run.

#### 4.1 How The Plateau Curves Were Obtained

As indicated from section 3, a plateau curve is basically the TRIC output signal plotted as a function of the applied voltage. These plots were done by having the collection plates of the TRIC or halo monitor connected to a preamplifier, which changed the current into a voltage. The preamplifier was then read by a CAMAC digital voltmeter (Kinetic Systems 3527) which sent the voltage value to the computer.

During the first run the two upstream triangular plates were tied together and the two downstream triangular plates were also tied together, to give two separate signals. These two signals, along with three separate signals from the wing plates, and the central plate were all sent to the University of Alberta 6 channel two stage preamplifier. The gains in this preamplifier were as follows: 50 mV/ $\mu$ A (with an output full scale of 10 V) for the main plate, 24 mV/nA (with an output full scale of 10 V) for the side plates, and 100 mV/ $\mu$ A (with an output full scale of 10 V) for the triangular plates. When the halo monitor was used (and the main assembly was not used), the 6 channel preamplifier was used for two of the halo monitor plates at a time. The gain used in this case was 24 mV/nA (with a full scale of 10 V). The high voltage supply used for the main assembly was a Spellman supply, which sent a monitor signal to the digital voltmeter (10 V = 20 kV). A Bertan 10 kV supply was used for the halo monitors, which also sent a monitor signal (10 V = 10 kV) to the digital voltmeter. In order for these plateau curves to be normalized with respect to pressure, the Baratron pressure gauge on the TRIC was read into the digital voltmeter



(10 V = 1000 torr). Late in the first run, the beam current, as measured by the 4ASEM, was sent into a preamp which gave out a voltage which was then read into the digital voltmeter so that the plateau curves could be normalized to the beam current point by point.

During the second run, all four triangular plates were tied together and all three central plates were tied together. The signals from these two collection regions were then sent to the preamplifiers in the University of Alberta precision subtracter, which had a gain of 1 mV/ $\mu$ A and a full scale of 10 V. All four signals from the halo monitor were read at the same time and sent into the Los Alamos preamplifiers which had a gain of 2 V/ $\mu$ A and had a full scale of 10 V, until run number 98. For run 98 and onward the gain of these preamplifiers was changed to 1 mV/nA, with a full scale of 10 V. All of these preamplified signals were sent to the digital voltmeter, which was read by the computer. To normalize these plateau curves with respect to beam current, the normalization foil signal from the IPM was read. This was done by sending the normalization foil signal into the University of Alberta 32 channel preamplifier which then sent a voltage to the U of A 16 channel voltage to frequency converter which was then connected to a LeCroy 4434 ECL scaler. The converter was read and controlled by the computer. During this run a INR high voltage supply was used for the main plate assembly. It had an output monitor which was set to the digital voltmeter (1 V = 10 kV). The halo monitors used the same Bertan supply as in the first run and the pressure was read the same way as in the first run.

After all of these electronics were set up, the plateau curves were generated by having one person run the data acquisition program and one person vary the high voltage manually. The high voltage was taken from 0 to a certain of negative voltage and then back down to 0 volts for each individual run. The results of these measurements are discussed in chapter 5.

## 4.2 How The Noise Factor $\alpha$ Was Measured

Before the method of measuring  $\alpha$  is discussed, what  $\alpha$  is and why it is important should be examined. Alpha can be thought of as intrinsic chamber noise relative to the noise from proton statistics (shot noise). So basically if  $\alpha = 0$ , the noise in the TRIC would only be due to proton shot noise. Alpha is defined by:

$$\frac{\alpha}{\sqrt{N}} = \frac{\delta I_c}{I_c} \quad (4.1)$$

where  $N$  is the number of protons in the incident beam,  $I_c$  is the current signal from the chamber, and  $\delta I_c$  is the root mean square detector noise due only to the physical effects that contribute to noise within the chamber. Alpha is important because it determines how long the final data taking experiment will run to get the required

statistical precision. To find the run time the function  $A_{zobs}$  was defined as:

$$A_{zobs} = \frac{S}{T} P_z A_z = \frac{N^+ - N^-}{N^+ + N^-} \quad (4.1a)$$

where  $S$  is the percentage of scattered protons,  $T$  is the percentage of transmitted protons,  $P_z$  is the percentage of polarized beam,  $N^+$  is the number of counts taken in the positive helicity state,  $N^-$  is the number of counts taken in the negative helicity state. Since  $N^+ - N^- \approx 10^{-8}$ , it was assumed that  $N^+ = N^- = N$ . Clearly from 4.1a, it was found:

$$(\delta A_{obs})^2 = \left( \frac{S}{T} P_z \delta A_z \right)^2 = \frac{(\delta N)^2}{2N^2} \quad (4.1b)$$

But it was known that the error in  $N$  is due to shot noise and chamber noise:

$$(\delta N)^2 = (\delta N_{shot})^2 + (\delta N_{TRIC1})^2 + (\delta N_{TRIC2})^2 \quad (4.1d)$$

By using 4.1 and the fact that  $(\delta N_{shot})^2 = NS$ , it was found that:

$$(\delta N)^2 = NS + N\alpha_1^2 + N\alpha_2^2 \quad (4.1e)$$

By using 4.1b, 4.1e, and the fact that the experiment runs for 2 helicity states:

$$2N = \frac{TI_b t}{e} = \frac{S + \alpha_1^2 + \alpha_2^2}{\left( \frac{S}{T} P_z \delta A_z \right)^2} \quad (4.1f)$$

where  $I_b$  is the beam current,  $t$  is the run time, and  $e$  is the electronic charge. If 4.2f is solved for  $t$  and if  $S$  and  $T$  are set for a 20 cm liquid hydrogen target, then the run time is given by:

$$t = t_0 \left( 1 + \frac{1}{S} \left( \frac{20}{L} \right) (\alpha_1^2 + \alpha_2^2) \right) \quad (4.2)$$

where:

$$t_0 = \frac{20e}{SLIP_z^2 (\delta A_z)^2} \quad (4.3)$$

where  $S$  is the scattering probability for a 20 cm target (2%),  $L$  is the liquid hydrogen target length in cm,  $I$  is the beam current,  $P_z$  is the longitudinal polarization of the beam,  $\delta A_z$  is the required statistical error in  $A_z$ , and where the individual TRIC noise factors are given by  $\alpha_1$  and  $\alpha_2$ .

Two different ways of measuring  $\alpha$  were used during the September run: 1) by using the FFT manually and 2) by using the voltage to frequency converter (V/F). In order to cancel out the shot noise in the chamber, signals from two collection plates in the TRIC must be subtracted. This assumes that the chamber noise will be incoherent and therefore add in quadrature, whereas the shot noise will be coherent and cancel. In other words, this measurement uses effectively two separate plates in

the chamber to measure the protons going through the chamber. Shot noise is due to statistical nature of ionization in the chamber proton beam, so since both plates will see the same incident proton the shot noise will be the same for both plates and therefore it will cancel. Whereas different numbers of ions will be collected on the two plates, depending on the physical noise processes within the chamber. The two signals from the TRIC came from tying the two upstream triangular plates together and from tying the two downstream triangular plates together when in 15 cm mode. In 30 cm mode, the two TRIC signals came from tying all the triangular plates together and from tying the main plate and the wings together.

When the FFT was used, the TRIC signals were amplified by the 6 channel University of Alberta preamplifier (gain of 50,000), then sent to the Los Alamos analog subtractor (gain of 50), and this difference was then sent to the FFT. This FFT was used to measure the spectral density, which gives an indication of the noise within the chamber. The FFT produced plots of voltage versus frequency. An example of a FFT plot is shown in figure 4.1. It was not possible to obtain print outs of FFT plots during the September test run, figure 4.1 is a FFT plot from earlier tests of the borrowed LAMPF ionization chamber. The peaks in the spectrum are at multiples of 60 Hz; they are due to electronic noise pick up. The voltage given on the vertical axis is a measure of the amplitude of the frequency component of the spectrum. The spectral density,  $S_d$ , was then found by selecting a part of the spectrum, integrating this part of the spectrum, and then dividing this part of the spectrum by the square root of the frequency range selected. This method was used

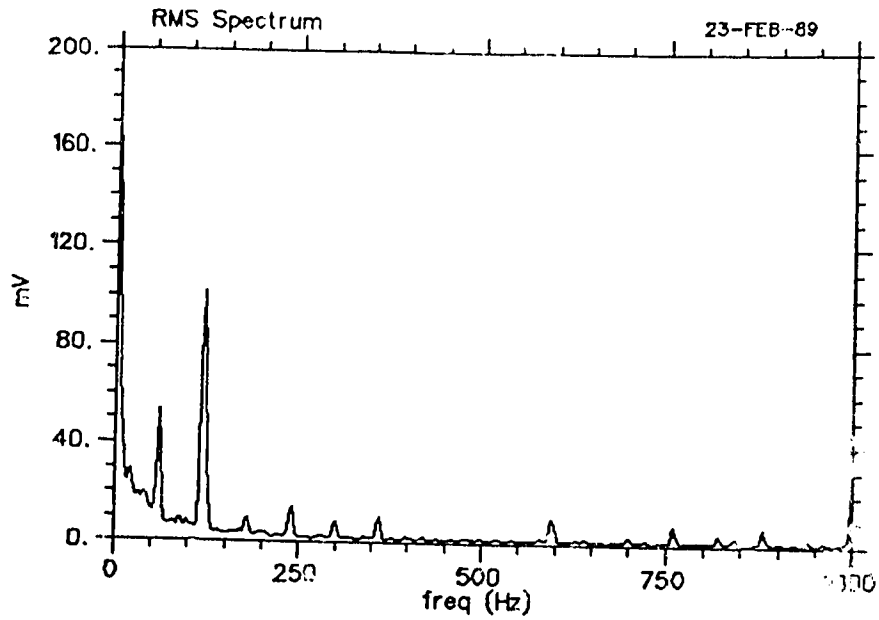


Figure 4.1: An example of the output from the FFT. The peaks are at multiples of 60 Hz.

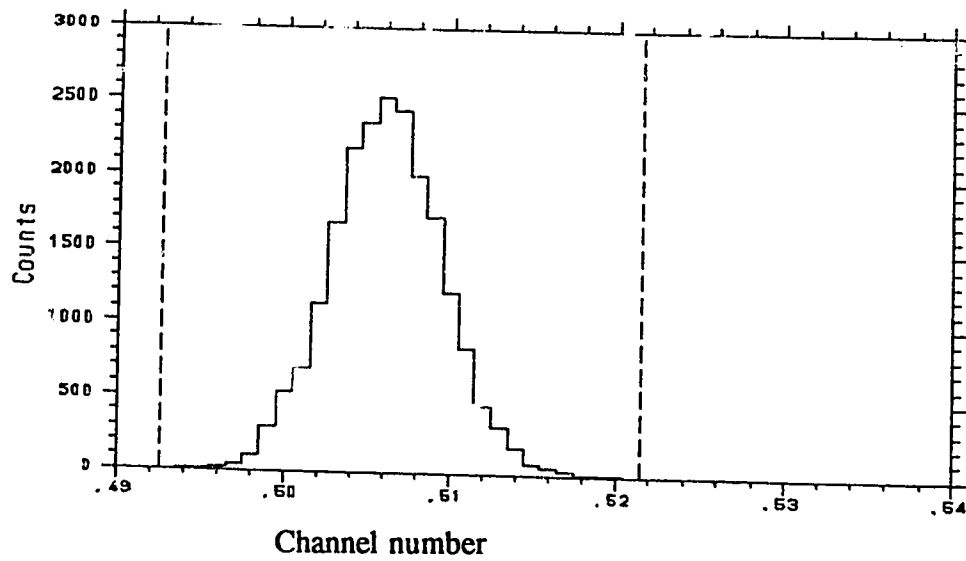


Figure 4.2: A histogram of a digitized difference signal. The full width half maximum of this histogram is used to calculate the noise figure,  $\alpha$ .

since the spectral density is independent of the binning selected on the FFT. So for example if a region between 80 Hz and 100 Hz is selected, this region is then integrated to give a value of 1 mV, and the spectral density is given by:

$$S_d = \frac{1}{\sqrt{100 - 80}} = .22 \frac{mV}{\sqrt{Hz}} \quad (4.4)$$

The root mean square noise is then given by  $S_d/\sqrt{2}$ . So by comparing this root mean square noise to the shot noise,  $\alpha$  measured by the FFT is given by:

$$\alpha_{FFT} = \frac{S_d \sqrt{2}}{2 G_{diff} R_f g \sqrt{Ie}} \quad (4.5)$$

where  $G_{diff}$  is the difference box gain,  $R_f$  is the feed back resistance of the preamplifier,  $g$  is the gas gain of the chamber,  $I$  is the beam current, and  $e$  is the electronic charge.

When the V/F was used, the TRIC signals were amplified by the 6 channel University of Alberta preamplifier, then sent to the Los Alamos analog subtracter. This difference was then sent to the V/F which was inside the Los Alamos preamplifier, which sent this frequency to a Kinetic Systems 3615 hex scaler which was read by the computer. This scaler was controlled by a LeCroy 222 dual gate generator, which was started by the computer. A histogram of this digitized

difference signal was displayed on the computer, so that the full width half maximum of this histogram could be found, thereby determining  $\alpha$ . Figure 4.2 shows a typical histogram of the digitized difference signal. Alpha in this case is given by:

$$\alpha_{dig} = \frac{2.3 \times 10^{11} F}{R_f PL} \sqrt{\frac{\delta t}{IN_s}} \quad (4.6)$$

where  $F$  is the full width half maximum of the histogram,  $R_f$  is the effective preamplifier gain in ohms,  $P$  is the pressure within the chamber in atmospheres,  $L$  is the length of the plates in cm (either 30 cm or 15 cm),  $I$  is the beam current in nA,  $N_s$  is the number of samples taken per computer read,  $\delta t$  is the time for a single sample in seconds. Equation 4.6 was found simply by rearranging equation 4.1 for  $\alpha$  and substituting the appropriate factors.

### 4.3 How $\delta A_z$ Was Measured.

During the March 1993 experimental run, the signals from the four triangular collection plates were tied together and the signals from the three middle plates were tied together. The signals from these two halves of the TRIC were amplified and subtracted by the University of Alberta precision subtracter. This voltage signal was then sent to the University of Alberta V/F converter which gave out a frequency. This frequency was then sent to a CAMAC Kinetic Systems 3615 hex scaler, which



then sent the number of counts to the computer. This scaler was controlled by a Jorway 221 12 channel timing and sequence module, which has a high accuracy (within  $\pm 0.1\%$ ) internal quartz clock. This timing and sequence module was CAMAC controlled. This whole process was repeated for another effective spin state. Then the number of counts from the two spin states were subtracted (note that these counts were normalized to one of the TRIC signals). The spin of the protons were not actually flipped during this test run, so that only noise from the chamber was measured. Call this normalized difference  $\Delta V/V$ . The values of  $\Delta V/V$  were then put into a histogram. Figure 4.3 shows a typical histogram of  $\Delta V/V$ . The value of  $\delta A_z$  was found by using the following equation:

$$\delta A_z = \frac{TF_{\Delta V/V} \sqrt{t_{pt}}}{2.35 \sqrt{300 \times 3600} SP} \quad (4.7)$$

where T is the amount of beam transmitted through the liquid hydrogen target (.96), S is the amount of beam scattered by the liquid hydrogen target, P is the beam polarization (.80),  $t_{pt}$  is the run time per point on the histogram in seconds, and  $F_{\Delta V/V}$  is the full width half maximum of the histogram. This expression assumes that the liquid hydrogen target is 40 cm long. This expression does not take into account that the beam current used for the experiment will be 500 nA. This  $\delta A_z$  is a best case scenario, seeing that only one TRIC was used.

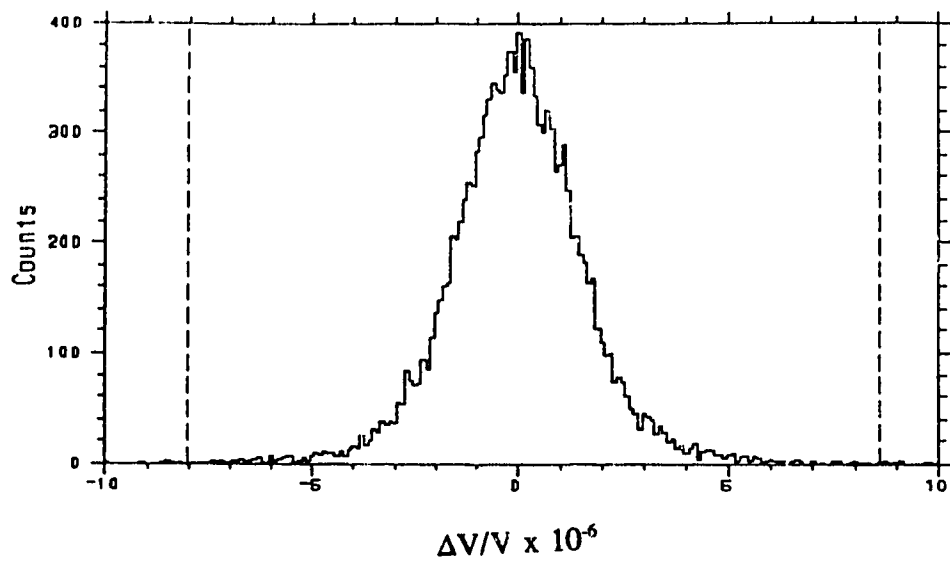


Figure 4.3: Histogram of  $\Delta V/V$ . The full width half maximum of this histogram is used to find  $\sigma$ .

## 5 Results of the Main Assembly Plateau Measurements

During the September 1992 test run, plateau measurements of the main plate were made. The main plate (without wings) plateau graph (figure 5.1) shows that everything seems to be working fine, since the TRIC output tends to follow a curve similar to the first two sections of figure 3.2. The TRIC plateaus for beam currents varying from 100 nA, 200 nA and 500 nA at 1/3 atmosphere. A universal curve for an ionization chamber can be obtained by plotting the normalized TRIC output (TRIC output / pressure / beam current) verses the applied voltage / pressure / square root of the beam current. The universal curve (figure 5.2) was made for the main plate for the first 13 runs (beam currents from 100 nA to 500 nA and chamber pressures of 1/3, 2/3, and 1 atmosphere). For this run, a signal from another beam current monitoring device was not used to measure the beam current for each point on the graph. There seems to be a curve that is followed, but there are many fluctuations. These fluctuations in the data are due to fluctuations in the beam current. The fact that the Einzel lens (used in the ion source of the cyclotron) was sparking, which results in the beam current going to zero, is also apparent in this figure. Later in this September test run the computer read beam current from the 4ASEM, so that each point on the plateau curve could be normalized by the beam current. Figure 5.3 shows a universal plateau curve for beam currents of 250 nA and 350 nA at 2/3 of an atmosphere. It can be seen from this figure that normalizing point by point greatly minimizes the fluctuations that were in figure 5.2. During the March 1993 test run,

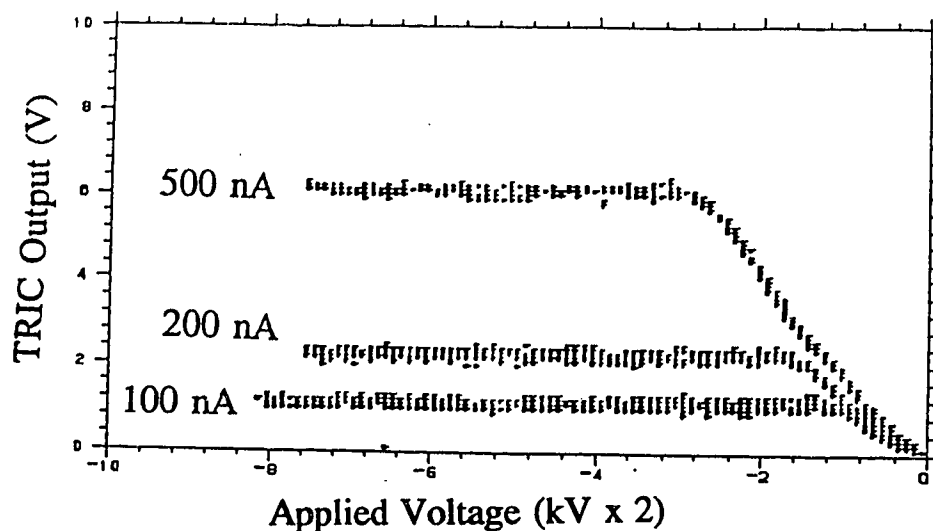


Figure 5.1: The TRIC output plotted versus the applied voltage for different beam currents as a chamber pressure of 1/3 of an atmosphere.

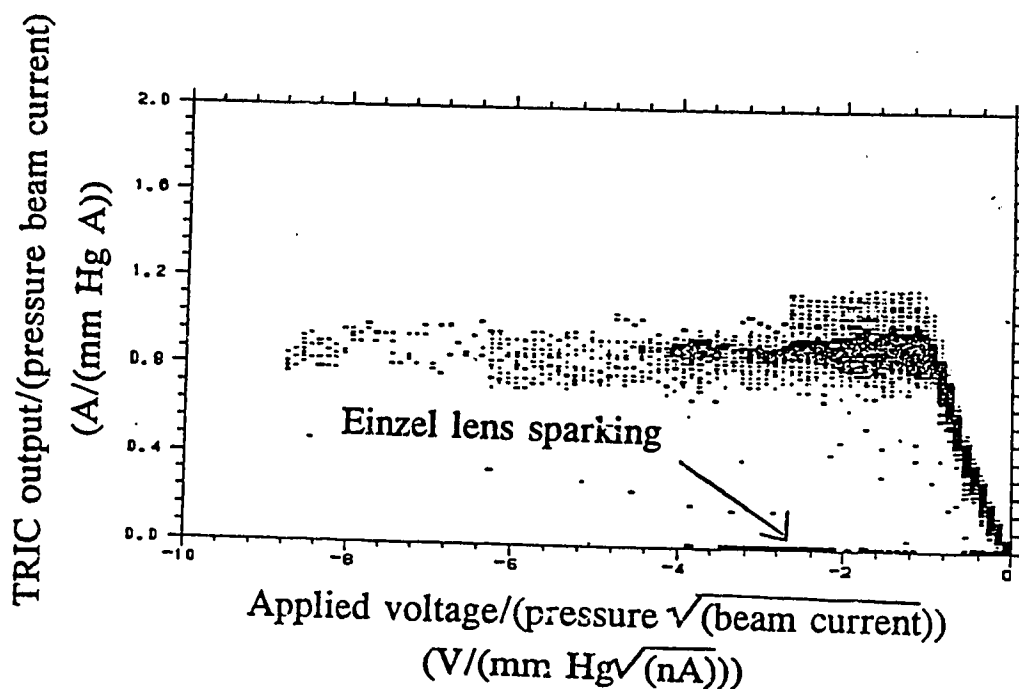


Figure 5.2: The universal curve for the main plate for beam currents from 100 nA to 500 nA and for chamber pressures of 1/3, 2/3, and 1 atmosphere.

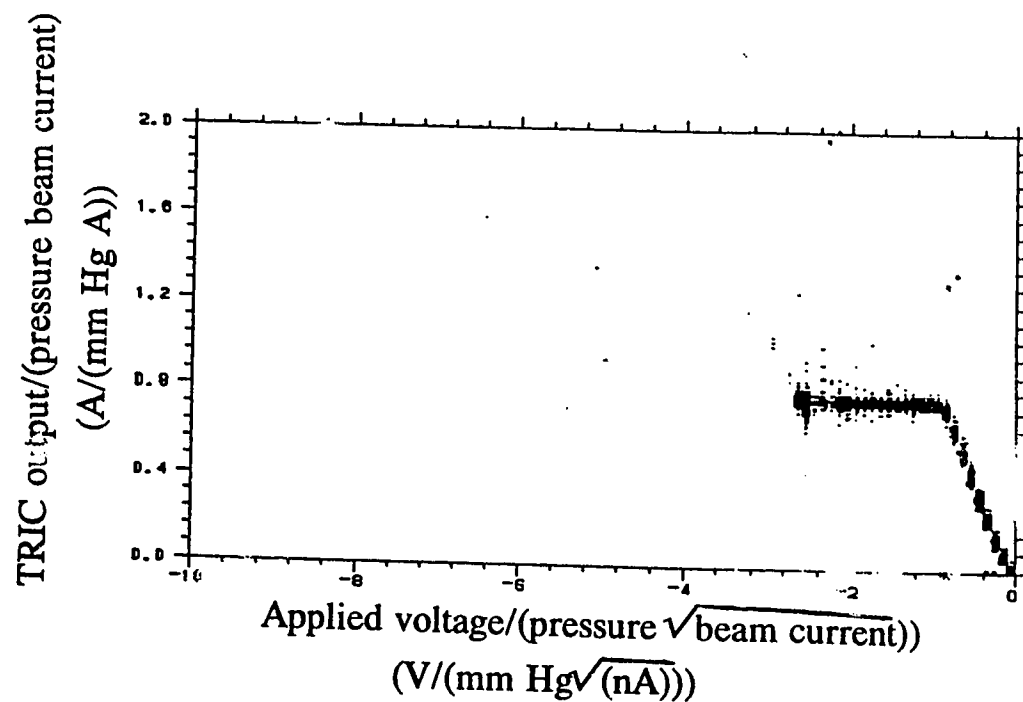


Figure 5.3: The universal curve for beam currents of 250 nA and 320 nA, at a chamber pressure of 2/3 atmosphere. The beam current was measured for each point on the graph.

there were two runs (both at about 130 nA and at 2/3 atmosphere) from which universal plateau curves were made. This time plateau curves were made from all four triangular plates tied to together (end plates) and from the three middle plates tied together. Also the parity intensity profile monitor was used to center the beam and to measure the beam current. Universal curves for these two plate configurations were almost identical. Figure 5.4 shows the universal plateau curve for the middle plates. These plateau curves were very flat. The slope of which has been measured to be  $(-4 \pm 6) \times 10^{-5}$  mA/nA/V for the end plate configuration and  $(2 \pm 6) \times 10^{-7}$  mA/nA/V for the middle plate configuration.

By locating the knee voltage in these universal curves, an idea of how the chamber is responding to space charge effects measured. Table 5.1 shows the knee voltages that were obtained from the universal curves, for various beam currents, pressures and runs.

Table 5.1: Knee voltages from universal curves.

Plates	Run	Beam Currents (nA)	Pressure (Atmospheres)	Knee Voltages (kV/ATM/ $\sqrt{\text{nA}}$ )
Main	Sept.	100 - 500	1/3, 2/3, 1	$.85 \pm .12$
Main	Sept.	350, 250	2/3	$.73 \pm .12$
Mid	Mar.	130	2/3	$.73 \pm .03$
Ends	Mar.	130	2/3	$.75 \pm .03$

Note that the first value shown in the table did not have a beam current signal read for each point on the curve. The values in table 5.1 are all consistent with each other and with the previous value obtained with the borrowed LAMPF ionization chamber

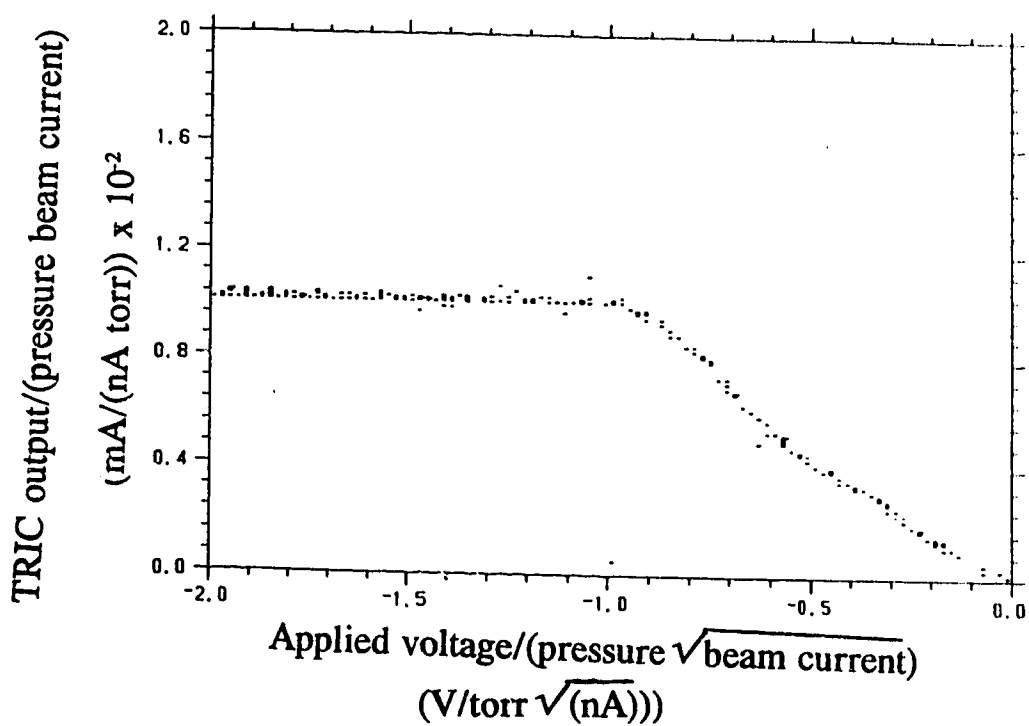


Figure 5.4: The universal curve for the three middle plates tied together, for a beam current of 130 nA, and a chamber pressure of 2/3 atmosphere.

which was discussed in section 3.6. The values in the above table are encouraging because they imply that the new chamber is not any worse than the borrowed LAMPF ionization chambers, when space charge effects are considered.

During the September run, plateau curves for the wing plates were also made for beam currents of 100 nA, 200 nA, and 500 nA. Figure 5.5 shows these plateau curves for the left wing. At beam currents  $> 300$  nA and at  $1/3$  ATM the wings do not plateau before the maximum applied voltage. By looking at the universal curves (figure 5.6a and 5.6b) for these plates for 16 runs (beam currents of 100 nA to 500 nA and chamber pressures of  $1/3$ ,  $2/3$  and 1 atmosphere), it can be seen that not enough voltage is applied at beam currents  $> 300$  nA to cause the wings to plateau. It is estimated that at voltages not much greater than 16 kV, the wings should plateau for beam currents  $> 300$  nA. This estimate comes from the position of knee in the curve in figure 5.5. This point is shown on the graph. It can also be seen that at small applied voltages that the wings tend to receive more signal. As the voltage is turned up, the extra signal decreases. This extra signal is due to the applied voltage not being strong enough for the ions to travel straight down to the main collection plate. Between the 13th run and 14th run, the beam was steered in the horizontal plane by changing thumbwheel 70 from -10 to +17. This action is seen on the graph by the left plate seeing less beam and the right plate seeing more beam.



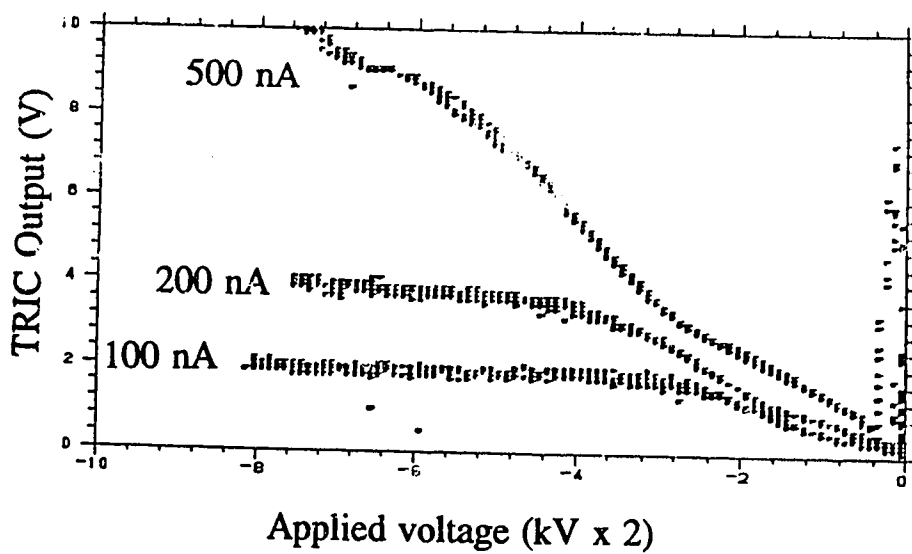


Figure 5.5: Plateau curves for the left wing at various beam currents and at a chamber pressure of 1/3 of an atmosphere.

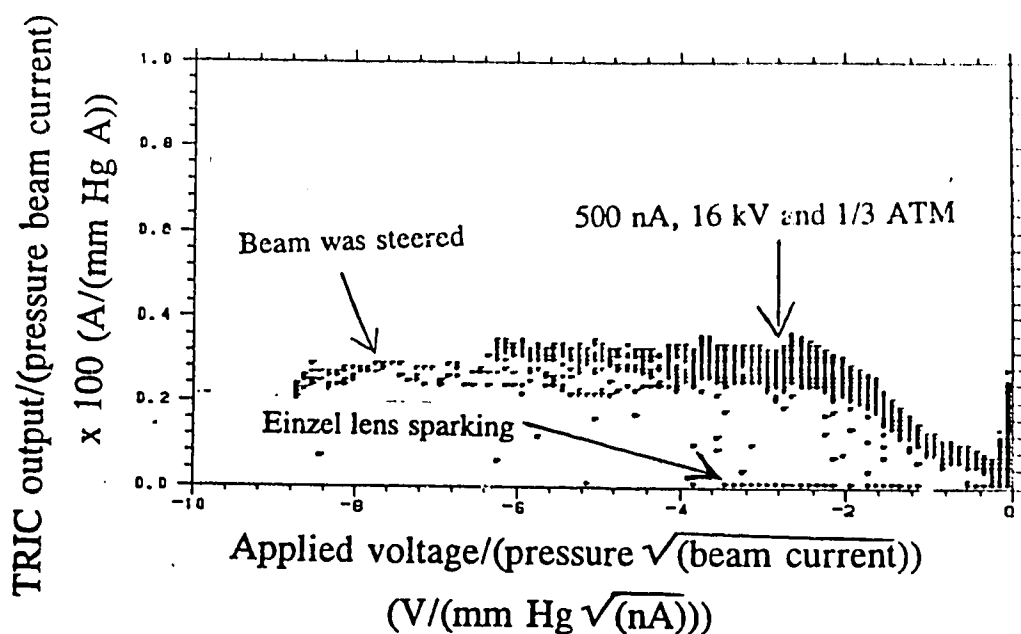


Figure 5.6a: Universal curves for the left wing for beam currents of 100 nA to 500 nA and chamber pressures of 1/3, 2/3 and 1 atmosphere.

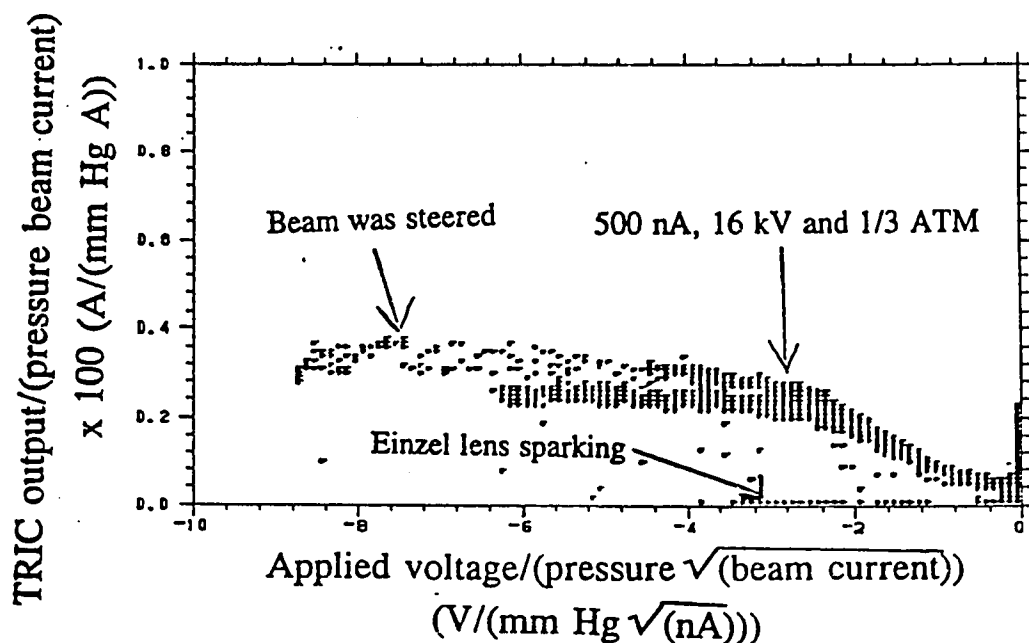


Figure 5.6b: Universal curves for the right wing for beam currents of 100 nA to 500 nA and chamber pressures of 1/3, 2/3 and 1 atmosphere.

## 5.1 Halo Monitor Plateau Results

In the September 1992 run, plateau curves for the halo monitor were also made. These plateaus look similar for the left, right, and bottom (the top signal connection came loose before the run). Figure 5.7 shows the plateau curve for the bottom halo monitor for beam currents of 300 nA and 500 nA at a chamber pressure of 2/3 of an atmosphere. This plateau and the other two plateaus have an unexplained bump in them. This bump also appears in the universal curves for the halo monitors. It was suggested that this bump could be caused by having the signal plates wired to unshielded cables. For the next run, shielded cables were used. During the March 1993 test run, these bumps were still seen. This bump is shown in figure 5.8, which shows the plateau curve for the bottom plate (this plateau curve only has the output of the halo monitor divided by the beam current). The first explanation is that the actual plateau is at the plateau level of these curves, and there is some mechanism that temporarily increases the signal. This is not a very likely scenario because it is very unlikely that something switches on and off just at a few voltages. The second explanation is that the plateau should be where the maximum of the bump is, and there is some mechanism which causes the amount of charge collected to decrease. This reasoning is more likely because the geometry of the halo monitor could lead to stray electric field lines from each high voltage plate, which could cause the charge to be swept out of the active region. It was also found that the electric field from the main assembly high voltage plate affects the halo monitor plateaus. This is shown in

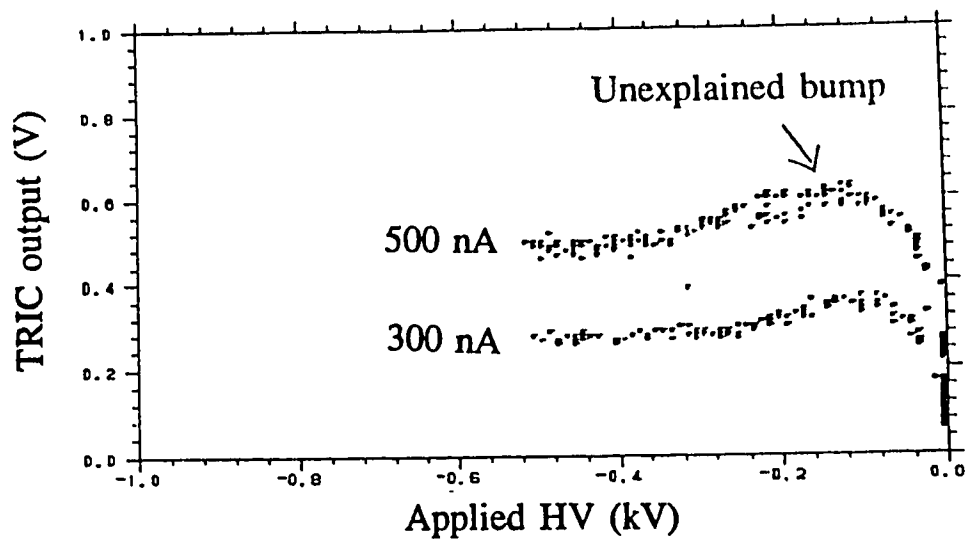


Figure 5.7: Plateau curve for bottom halo monitor for beam currents of 300 nA and 500 nA at a chamber pressure of 2/3 atmosphere.

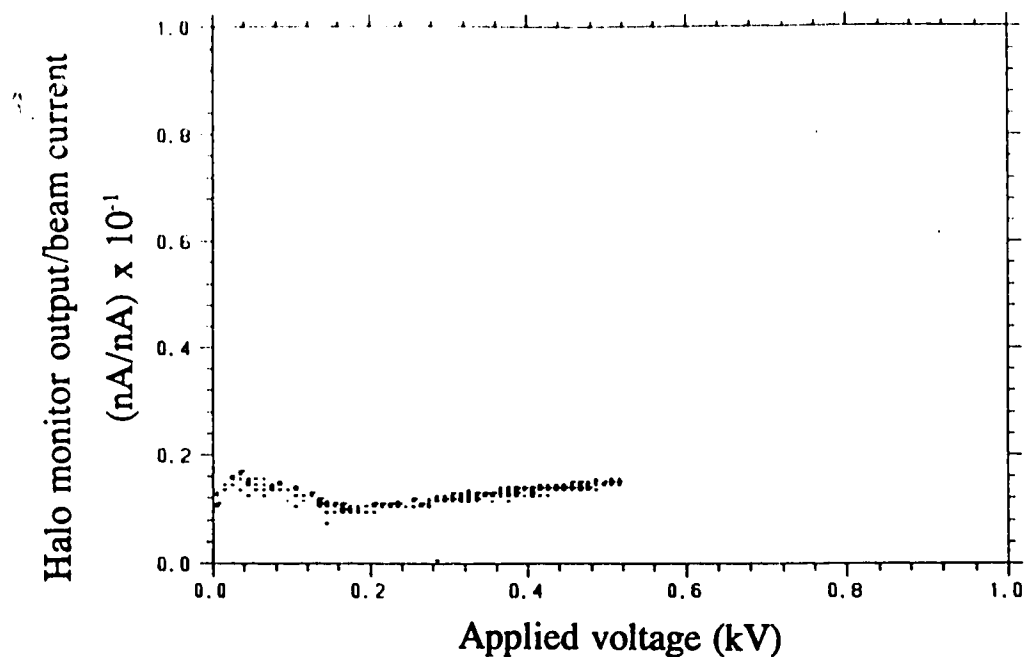


Figure 5.8: Plateau curve for the bottom halo monitor. The internal signal cables have been shielded, but the bump is still there. The main assembly high voltage has been turned off.

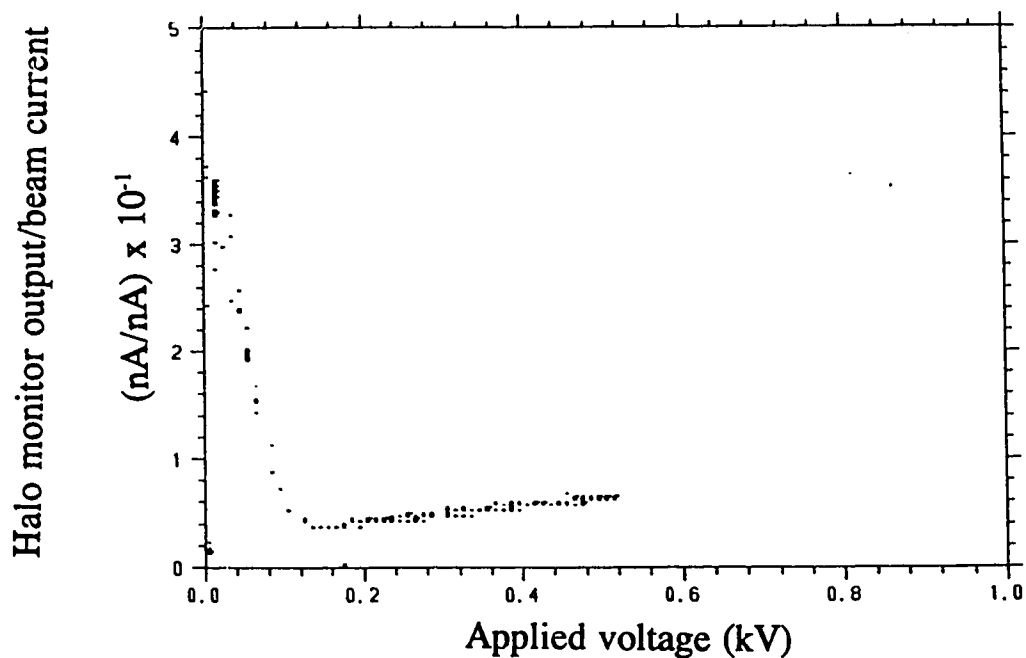


Figure 5.9: Plateau curve for the bottom halo monitor in the same situation as in figure 5.8 except now the main assembly high voltage is on at -13 kV. Note that the scale of this figure is 5 times larger than figure 5.8.

figure 5.9 for the bottom halo monitor when the main assembly has a high voltage of -13 kV. Note that the scale is a factor of 10 larger than the y axis on figure 5.8. The peak in figure 5.9 varies slightly between the four halo monitors. The peak is largest for the top halo monitor. The peaks for the left and right halo monitors are about the same height, and the peak for the bottom halo monitor is larger than these two peaks. This variation in peak height can be explained by the fact that the high voltage electrode of the main assembly is 19.3 cm away from the top and bottom halo monitors and 26.3 cm away from the left and right halo monitors. This effect, shown in figure 5.9, is thought to be due to cross talk between the halo monitor and the main plate assembly. So that there is no possibility of cross talk between these two devices during the final data taking (for example, halo monitor accidentally left on), the halo monitor has been removed from the TRIC. If the halo monitor has to be examined, it can be examined in its own separate box. A possible way to examine the internal cross talk of the halo monitor is to remove one section of the halo monitor and just test the top/bottom section or the left/right section. Another possibility is to change the high voltage connection configuration of the halo monitor.

By using the September 1992 data, the amount of halo in nA/cm<sup>2</sup> (figures 5.10a and 5.10b) has been calculated for both the wings (3.8 cm from the center of the beam) and halo monitor (5.2 cm from the center of the beam). These graphs show that the halo measured from these two devices are of the same order of magnitude, actually within a factor of 2 or so. Therefore the wings could be used instead of the halo monitor to measure the halo beam current and therefore the halo

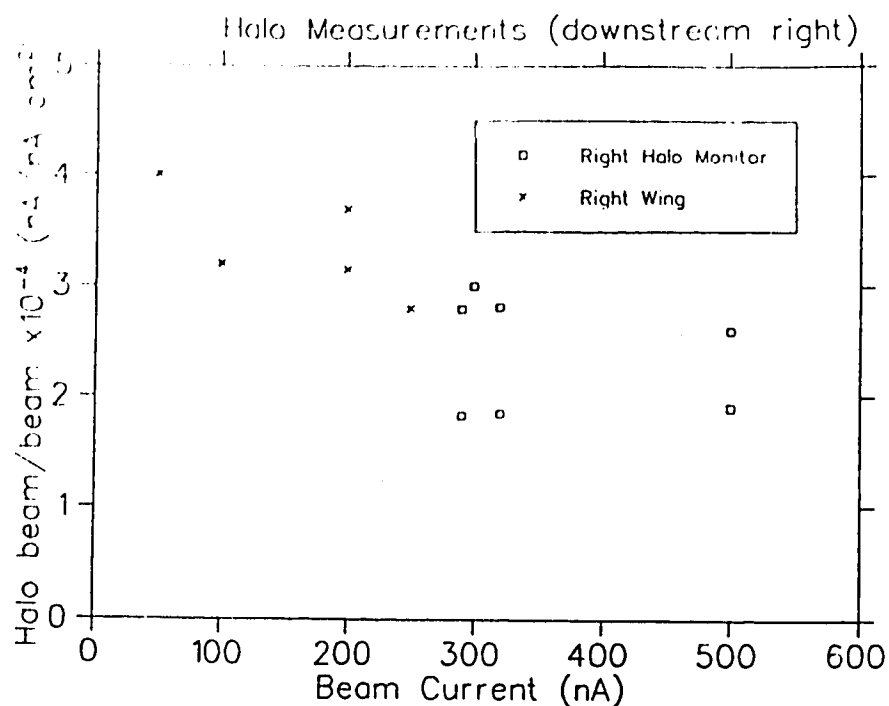


Figure 5.10a: The amount of halo measured by the right halo monitor and the right wing. The halo monitor is 5.2 cm from the center of the beam and the wings are 3.8 cm from the center of the beam.

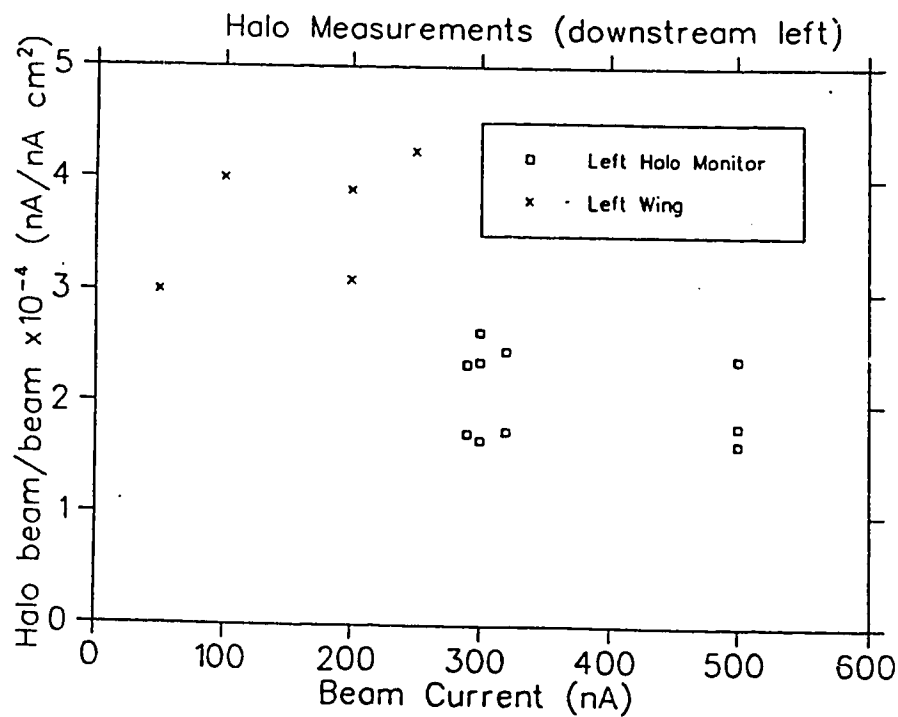


Figure 5.10b: The amount of halo measured by the left halo monitor and the left wing.

monitor can be taken out of the TRIC. Note that in figures 5.10 two points on the plateau curves were used to calculate the beam measured in the halo monitors. The value of peak of the unexplained bump was used as one point, while the flat section of the plateau was used as the other point.

## 5.2 Results of the Alpha Measurements

According to equation 4.2, alpha will have to be 0.8 or less in order for the experiment to run only for 300 hours. During the September test run, the noise factor  $\alpha$  was measured for various parameters. The range of  $\alpha$  at a chamber pressure of 1/3 atmosphere and for the 15 cm plate configuration is 0.5 to 1.2 as shown on figure 5.11. This range of data shows that in some cases the needed value of 0.8 can be achieved. The variation of  $\alpha$  with beam current and applied voltage are shown in this figure. As expected,  $\alpha$  increases at low applied voltages. These values of  $\alpha$  are comparable to the old TRIC measurement of  $\alpha$  which was found to be 0.53 at 7.8 nA and found to be 0.91 at 78 nA. Both of these measurements were at a chamber pressure of 1/3 of an atmosphere. These values for  $\alpha$  are close to the  $\alpha$  measured from the new TRIC, but these were found at much lower beam currents.

How alpha varies with the chamber pressure and with the length of the



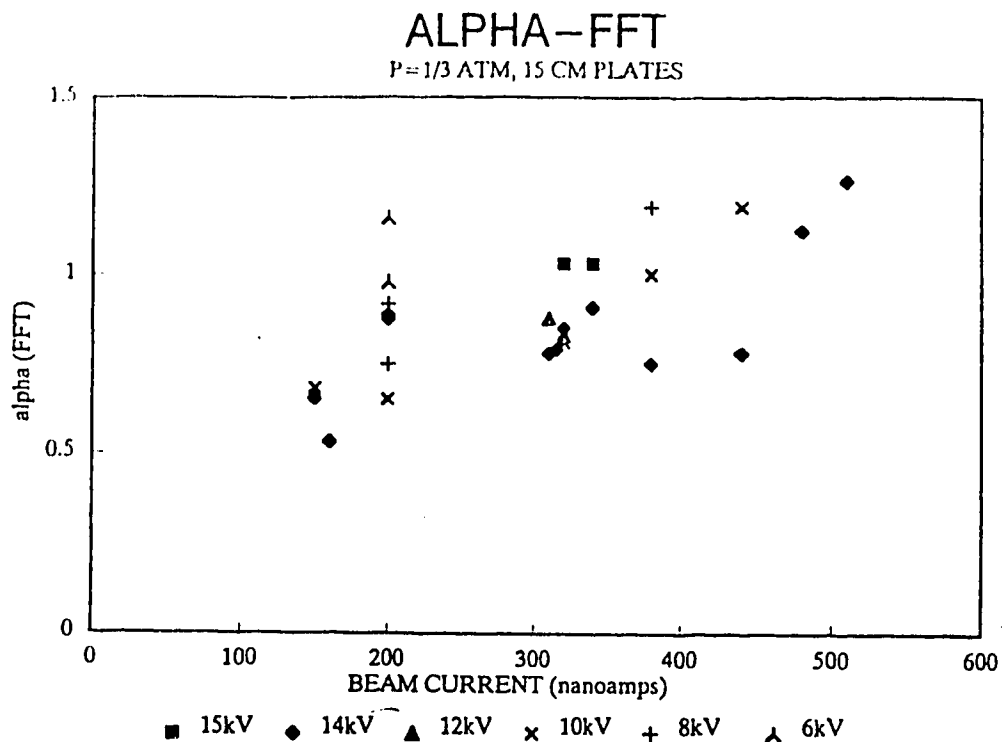


Figure 5.11: The range of  $\alpha$  for different beam currents and different applied voltages.

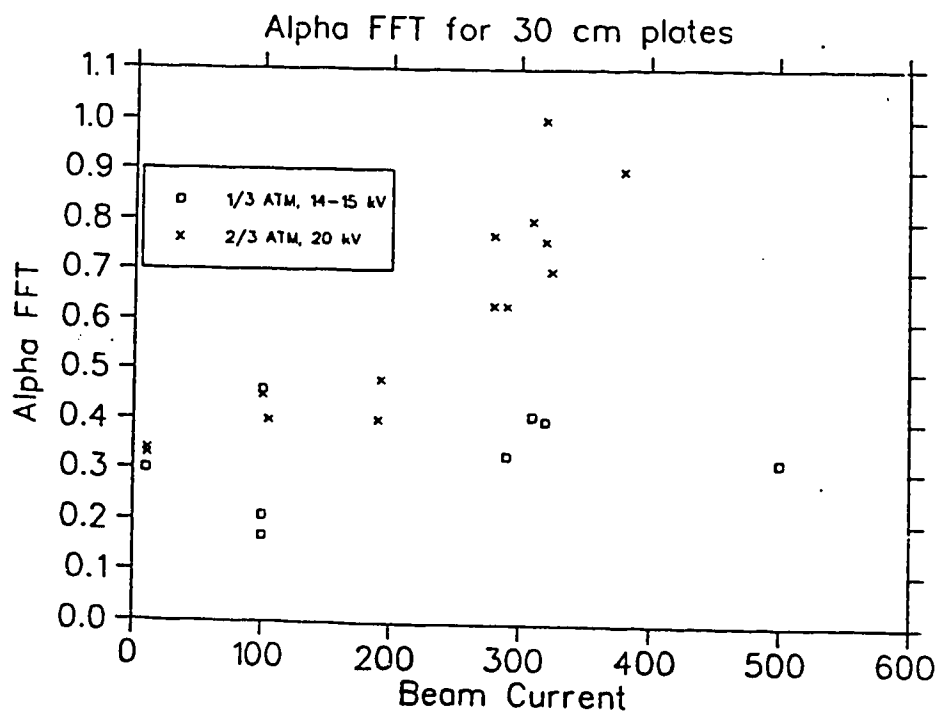


Figure 5.12: The noise figure  $\alpha$  does not decrease with increased pressure as the theoretical  $\alpha$  from delta rays would imply.

collection plates was also investigated. Figure 5.12 shows that the measured  $\alpha$  does not decrease with increased pressure as the theoretical  $\alpha$  from  $\delta$ -rays would imply. This fact would imply that some other mechanism would be dominating, when it comes to pressure changes. From the space charge section of chapter 3, it was found that decreasing the pressure would decrease the amount of space charge. This may be the mechanism which seems to dominate alpha's dependence on pressure. Figure 5.13 shows that  $\alpha$  does increase with decreased length of collection plates ( $L$ ). This fact agrees with the theoretical  $\alpha$  prediction from delta ray noise, but not absolutely. Figure 5.14 shows that  $\alpha$  does not seem to go like  $1/\sqrt{L}$  as the delta ray noise calculation from section 3.5 implied. But this trend does show that the idea of lengthening the plates to decrease alpha, was correct.

Two different ways of measuring alpha were used during the run. One method was by using the FFT manually and the other method was by using the V/F. These measurements were compared and it was found that digital (V/F)  $\alpha$  was consistently higher than the FFT  $\alpha$  by a factor of 1.5 to 3, as shown in figure 5.15.

So these  $\alpha$  measurements have shown that it is possible to do the experiment within 300 hours. They have also shown that the trend of  $\alpha$  decreasing as the collection plates are lengthened is a correct trend. It has also shown that space charge noise effects may be dominating delta ray and spallation noise effects. These measurements also have shown that increasing the chamber voltage, decreases  $\alpha$ , as expected.

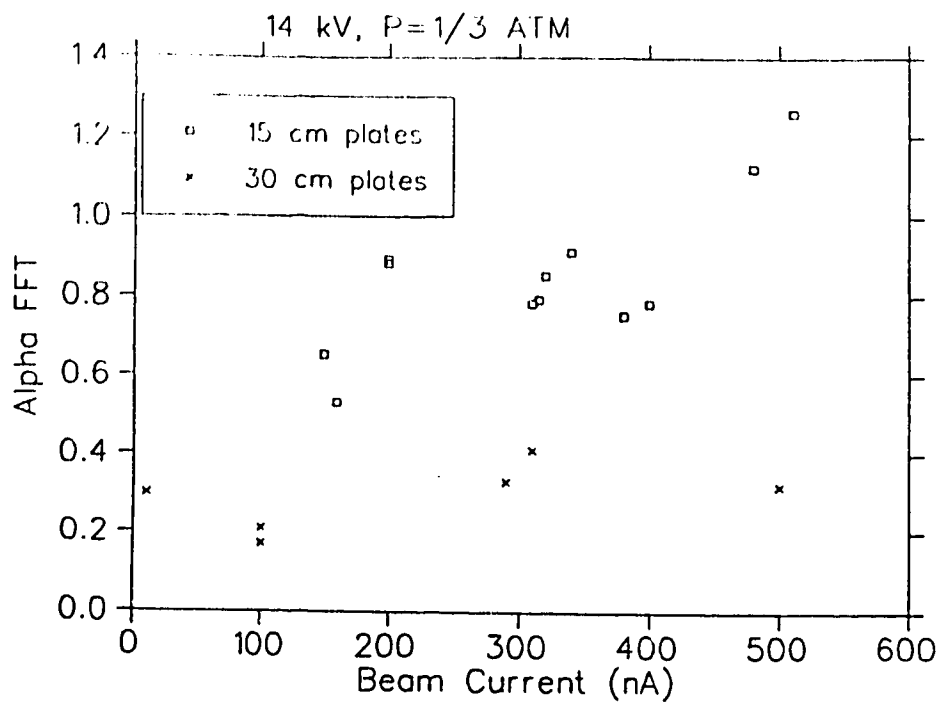


Figure 5.13: The noise figure  $\alpha$  increases with decreased length of collection plates.

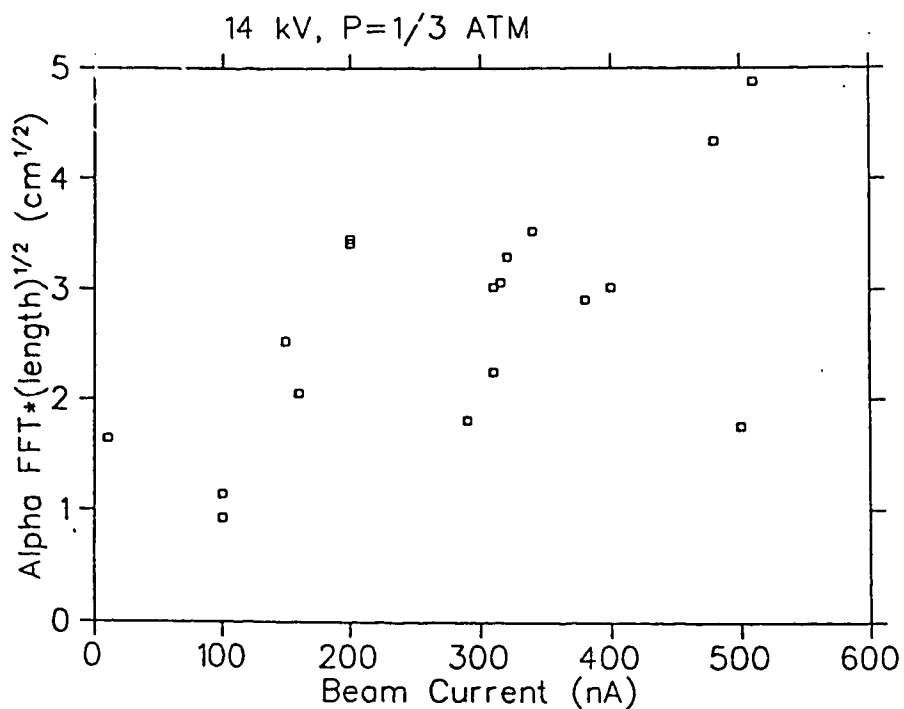


Figure 5.14: The noise figure  $\alpha$  does not go like  $1/\sqrt{L}$  as the delta ray noise calculation implied.

### 5.3 Results of the $\delta A_z$ Measurements

By using the method outlined in section 4.3 the error in  $A_z$  in terms of chamber noise was measured. Figure 5.16 shows  $\delta A_z$  as a function of spin flip frequency. This graph shows that the TRIC measures  $\delta A_z$  between  $0.9 \times 10^{-8}$  and  $3.0 \times 10^{-8}$ , depending on the spin flip frequency. These results are for a beam current of 400 nA and assuming beam polarization of 80% and a target length of 40 cm. This fact shows that the TRIC is intrinsically capable of measuring  $A_z$  to the required statistical precision of  $2 \times 10^{-8}$  after 300 hours of data taking.

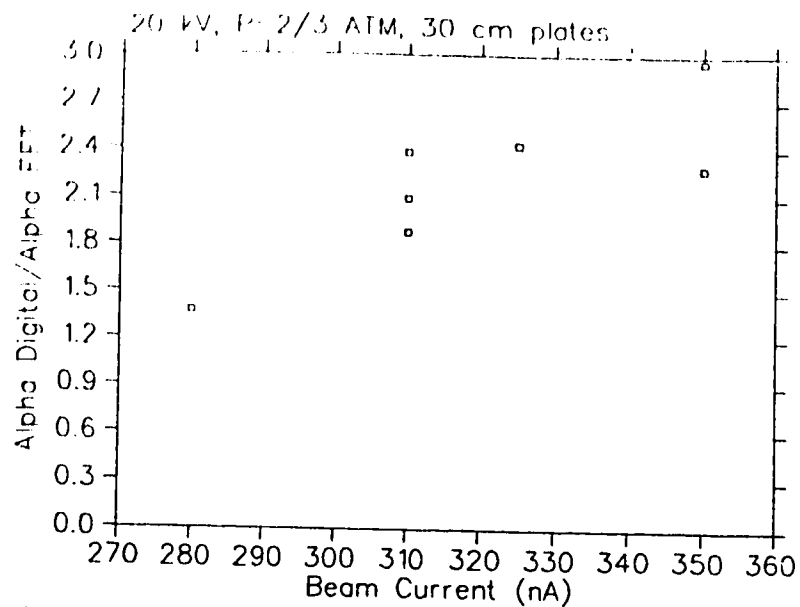


Figure 5.15: A comparison of the two methods used to measure  $\alpha$ . The digital alpha is about a factor of 1.5 to 3 larger than the FFT alpha.

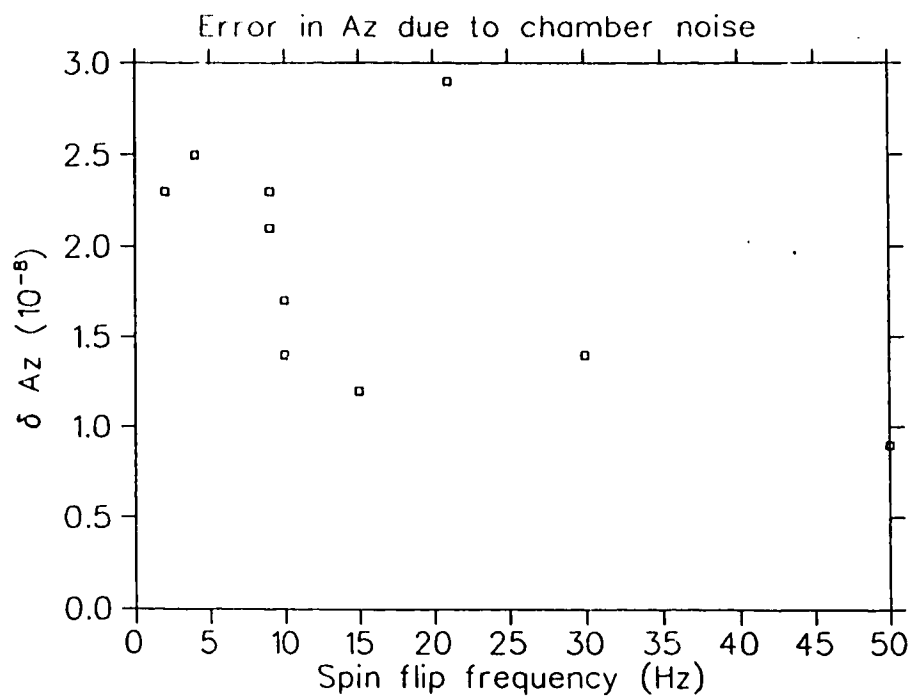


Figure 5.16: The error in  $A_z$  as a function of spin flip frequency.

## 5.4 TRIC Linearity

During the September 1992 run the TRIC was compared to the 4ASEM. By plotting the TRIC counts versus SEM counts (figure 5.17), it can be seen that the TRIC is a linear device, relative to the SEM. However, if you look at the situation more closely, by plotting the ratio of the TRIC counts to the SEM counts as a function of beam current measured by the 4ASEM (figure 5.18), then it appears as if the TRIC is nonlinear at the  $10^{-3}$  level. The SEM should be insensitive to space charge effects. At higher beam currents the TRIC should have larger signal loss due to space charge. So from these two facts, it is expected that the ratio would decrease with greater beam current. Figure 5.16 actually shows the opposite. Since the IPM does not saturate with increased beam current, figure 5.16 would imply that the TRIC output of the TRIC increases faster than it should. This conclusion would imply that the TRIC would be collecting more ions than it should at higher beam currents, which is not a likely effect. Another possibility, which is more reasonable, is that the beam size was large enough at the SEM such that the 4ASEM is missing some beam, that the TRIC sees. This explanation is reinforced by the fact that the distance between the TRIC and the 4ASEM was approximately 4 m. The decrease at the lowest beam current is due to the dark current in the SEM.

By measuring the slope of figure 5.17 between 100 nA and 400 nA, the sensitivity of the TRIC to beam current changes with spin flip is found to be  $(1.0 \pm 0.3) \times 10^{-3}$  per nA. Since an accuracy of  $\pm 2 \times 10^{-8}$  is required, the allowable amount

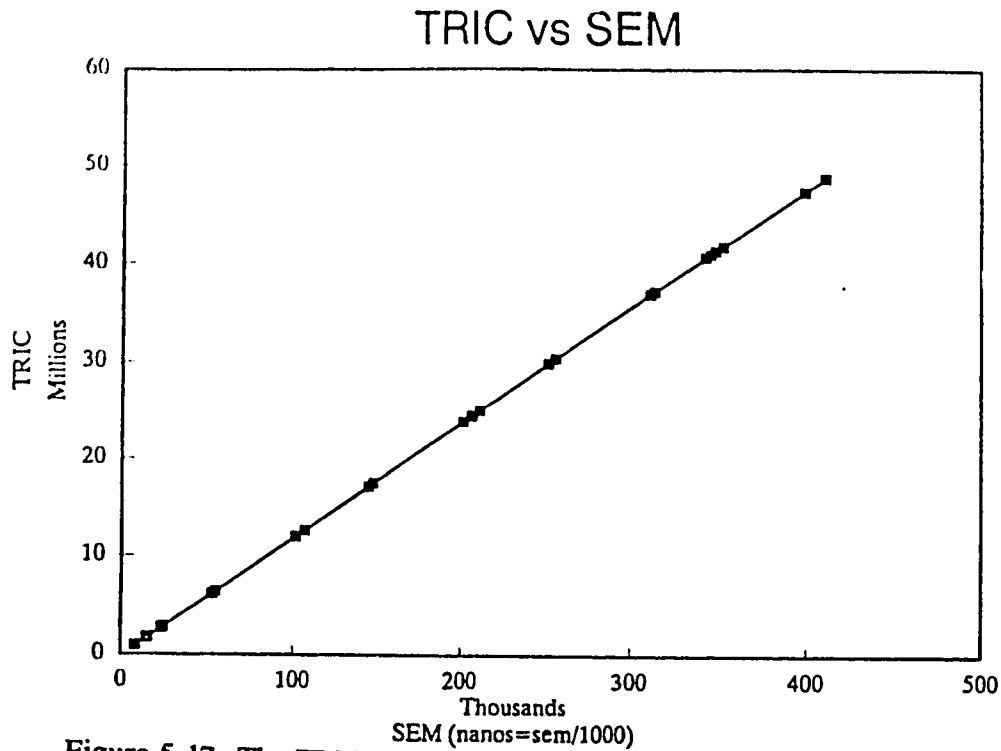


Figure 5.17: The TRIC appears linear when compared with the SEM.

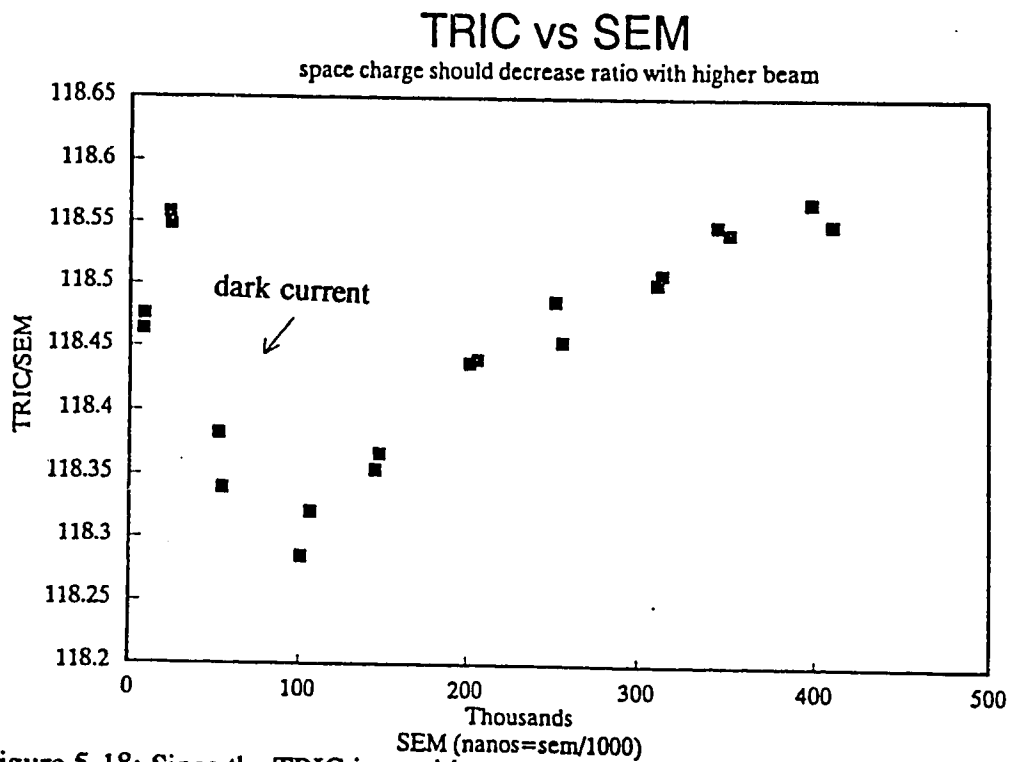


Figure 5.18: Since the TRIC is sensitive to space charge effects and the SEM is not, one would suspect that the ratio of TRIC/SEM should decrease as a function of beam current.

of beam current change with spin flip is  $\pm 2 \times 10^{-5}$ . This calculation assumes that the nonlinearity inside the TRIC is not due to the 4ASEM missing a small amount of beam.

## 6 Conclusion

The goal of this thesis was to describe the design considerations of transverse field ionization chamber and its performance with regard to the proton-proton parity violation experiment at 230 MeV at TRIUMF. It has been found that this ionization chamber follows a universal curve in which the applied voltage is normalized by the chamber pressure and the square root of the beam current. It has also been found that by measuring the noise factor with various collection plate lengths, chamber pressures, and applied voltages, an understanding of the physical processes involved in the chamber can be reached. From these measurements, it was found that increasing the length of the collection plates decreases the noise. This fact follows the trend described by delta ray effects. It was also found that by decreasing the applied voltage the noise in the chamber increases as expected. The fact that the noise decreases as the chamber pressure decreases shows that the spallation and delta ray noise is dominated by another process possibly space charge. Finally the results of a mock experiment showed that the TRIC is intrinsically capable of measuring  $A_z$  to the required statistical accuracy of  $2 \times 10^{-8}$ , within 300 hours of data taking.



## Appendix A: TRIC High Voltage Problem

During the September 1992 TRIC test run, it was found that the TRIC would not hold -20 kV when there was 250 torr of H<sub>2</sub> in the TRIC. During this run, the TRIC could only hold -16 kV at 256 torr when 380 nA of beam was passing through the TRIC. The TRIC did hold -20 kV with 500 nA of beam passing through the TRIC once the TRIC was filled up to 500 torr.

After the run the TRIC was filled to 758 torr of hydrogen. When -20 kV was applied to the TRIC, it was found that the resistor chain drew 0.22 mA of current. This amount of current was also found when the TRIC pressure was lowered to 512 torr. When the pressure was dropped down to 255 torr and -18 kV was applied the current drawn was 1.53 mA. The expected current draw at -20 kV is 0.13 mA. This fact implied that the TRIC was discharging at 255 torr. Figure A.1 shows the TRIC current as a function of applied voltage. This graph has two slopes, this fact could be due to a small leakage current. Both slopes do not give the correct resistance for the resistor chain, these slopes are lower in resistance. This lower resistance would imply that there is a leakage current somewhere within the TRIC. By looking into the view port on the TRIC, a glow between the corona shield and the TRIC's can was seen. The approximate position of the glow is shown in figure A.2.

Thinking that the roughness of the large flanges on the TRIC was the problem, the TRIUMF machine shop smoothed these welds. This action did not solve the problem, since during the March 1993 TRIC test run, the TRIC discharged at

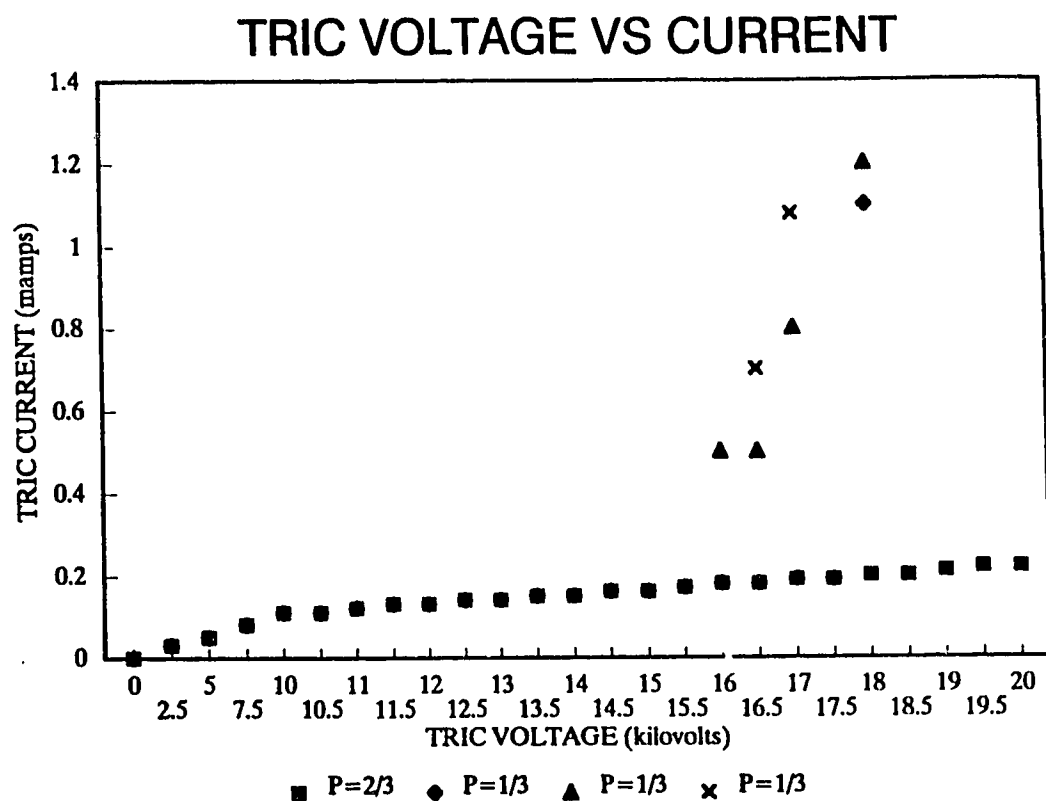


Figure A.1: The current drawn by the TRIC high voltage supply as a function of applied voltage. Note that the points above 0.3 mA are where the TRIC discharges.

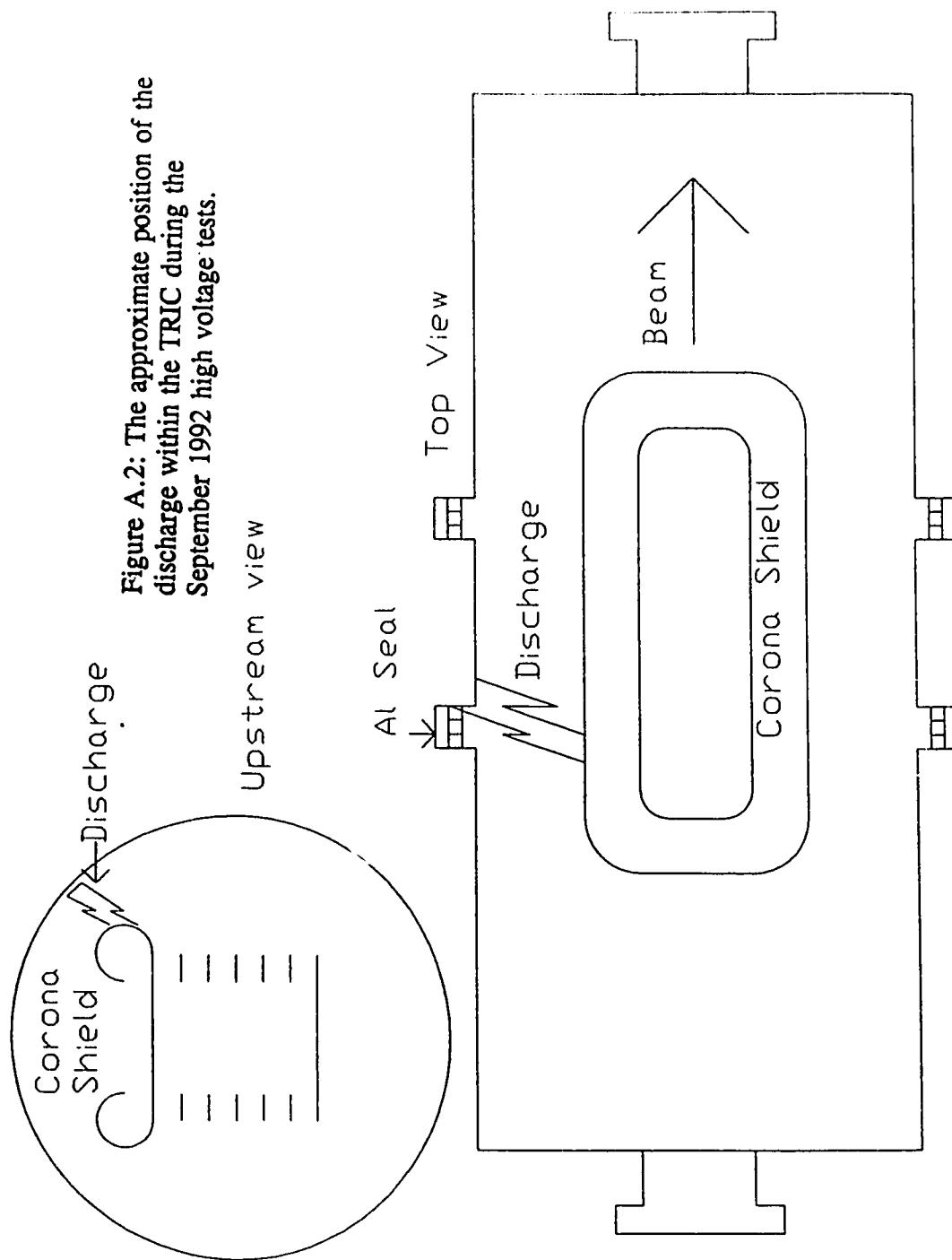


Figure A.2: The approximate position of the discharge within the TRIC during the September 1992 high voltage tests.

-16.5 kV (with 250 torr of  $H_2$  inside the TRIC and with the beam going through the TRIC). During this run it was found that at -16 kV and with the beam on, the raw signal from the TRIC had periodic spikes in it. These spikes did not go away once the beam was turned off. The halo monitor had no effect on these spikes. The spikes seemed to have a minimum interval between them. This interval decreased as the applied voltage was increased. It was thought that these spikes were from capacitor coupling.

After the March run, the discharge was seen by looking into the TRIC viewport. The discharge occurred when the TRIC high voltage was -17.6 kV and the TRIC pressure was 250 torr. The next diagram (figure A.3) shows what was seen inside the TRIC. Conditioning the TRIC was tried, but this process didn't seem to help. Seeing that the TRIC could not be filled with  $H_2$  in the TRIUMF proton hall extension, the TRIC was filled with enough Ar to make the TRIC spark at the same voltage as 250 torr of  $H_2$ . That is, the TRIC was filled up to 720 torr of Ar, so that a discharge would occur when -16 kV was applied. The discharge from the argon looked like a glow from a point source which was below the corona shield. In other words, the glow was between the corona shield and the can, but in a sector like shape with the point underneath the corona shield and the arc of the sector on the TRIC can. This point source was on the resistor side of the TRIC. The glow was different when +19.5 kV was applied. This glow was between the corona shield and the ground plate. This glow did not stay very long ( $< 1$  s). As the voltage was increased the glow would go away and a spark would be seen near the upstream end of the can.

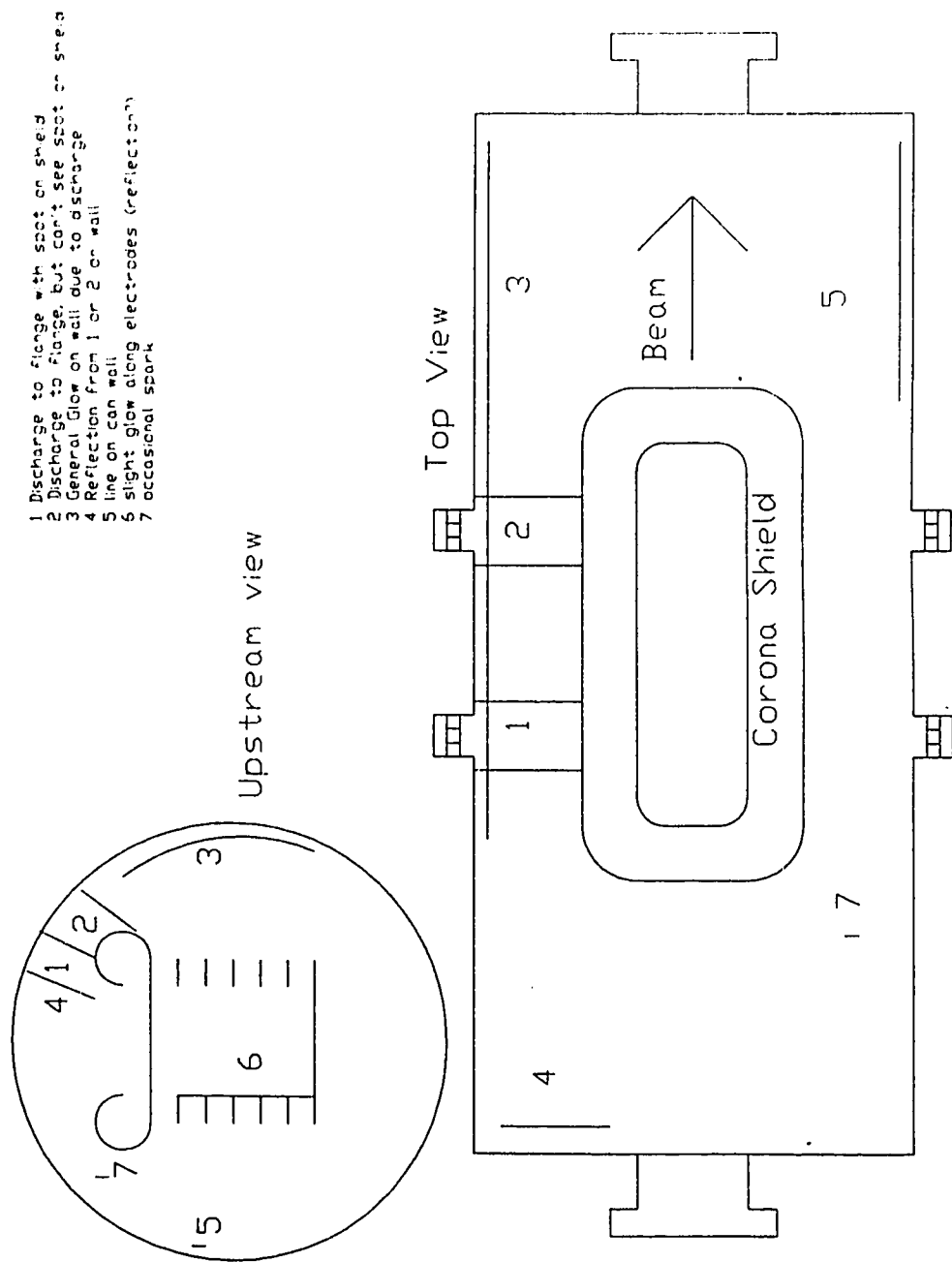


Figure A.3: The various glows seen during the March 1993 high voltage tests.

The TRIC was opened up to see what was causing the discharge. It was found that the soft solder used on the resistors had crept. There were soft solder beads on the suspension plate, on the collection plates, and on the side electrodes. A black spot was also found on the resistors that were attached to the corona shield. This spot was the closest object (with -20 kV applied to it) to the can. By putting one of the used crimp lugs from one of the resistors into an evacuated oven it was found that the solder crept at 200 °C, which is very close to the temperature of the TRIC during bakeout.

To alleviate the solder problem, silver solder was used on the resistors instead of soft solder. To solve the high voltage problem, these crimp lugs were put on so that the resistors would not stick out from the electrode stack, and the last resistor was attached to the corona shield by drilling a small hole in the shield, passing the -20 kV lead through this hole, and attaching this lead to the stainless steel stud on the ceramic post (part #44). These modifications were done using the TRIC 2 parts. The TRIC 1 assembly was not modified until later.

Once these modifications, were made the TRIC was filled with 719 torr of Ar. By use of the INR high voltage supply, voltage was applied to the high voltage stack. This voltage was turned up to -25 kV and +25 kV without the supply cutting out; the Russian supply has a 2 mA protection built into it. Since the Russian supply has no means of measuring the current drawn, another supply (Glassman) was also used. This supply was turned up to +20 kV and only drew 0.1 mV, which is the expected amount of current draw from the resistor chain. The same results were found when

then TRIC had 500 torr of Ar and 250 torr of Ar in it.

To satisfy the TRIUMF safety group, the TRIC was filled with 250 torr of  $H_2$ , outside of the proton hall. The Glassman supply was turned up to +20 kV and only drew 0.1 mA. The Russian supplies could be turned up to +25 kV and -25 kV without cutting out. These last two facts imply that the high voltage problem has been solved. The spikes in the TRIC signal could not be investigated, due to the fear that the TRIC would be rained on.

### Appendix B: Hydrogen Safety

Two possible problems that can occur when handling hydrogen are ignition and detonation. Now according to the Handbook for Hydrogen Handling Equipment<sup>30</sup>, the combustion limits of hydrogen in air are 4.1 - 74 volume percent hydrogen. These limits correspond to 26 - 95.9 volume percent of air getting into the TRIC chamber. Since the TRIC is going to be filled to only 1/3 atm, it will be under pressure, which means that the hydrogen will not leak out of the TRIC, but air may leak in. So this means that if the TRIC lets in 26% air then it is possible to have a fire inside the TRIC, but not outside. In order for the TRIC to have this mixture, the pressure would have to rise from 250 torr of hydrogen to 337 torr of the hydrogen and air mixture. The handbook also gives the detonation limits to be 18.3 - 58.9 volume percent hydrogen. These limits correspond to 41.1 - 81.7 percent volume of air getting inside the TRIC. Now to ensure that these things don't happen two things can be done: ensure no air gets into the TRIC and ensure that there are no sources of

ignition inside the TRIC. To ensure no air gets into the TRIC, the TRIC will be evacuated and then leak tested with a helium leak detector before the TRIC is filled with hydrogen. That should ensure that no air will get in before the TRIC is moved. Now the ignition problem must be looked at.

Inside the TRIC there is a high voltage plate, which could cause an ignition, if it is turned on and if the TRIC has 26 % air in it. In order to stop ignition from happening, the TRIC pressure will be measured before and after the TRIC has been moved to beamline 4A. If the pressure has not changed, then we know that no air has come into the TRIC and the experiment can be done. The high voltage will not be turned on unless we are certain no air has leaked into the TRIC. If the pressure has changed, then the TRIC will be evacuated in the beamline with a hose going from the exhaust of the roughing pump up into the fume hood. Then the leak will be found and fixed, before the TRIC is refilled in beamline 4A.

Now the other thing to consider is the possibility of hydrogen being let out during the filling of the TRIC. The TRIC will be filled by use of a palladium leak, which ensures the purity of the UHP hydrogen by only letting hydrogen into the TRIC. The TRIC will not be left unsupervised when it is being filled. The Handbook of Hydrogen Handling Equipment<sup>30</sup> talks about experiments done to try to achieve a detonation of unconfined hydrogen. The experiment was an attempt to detonate a mixture of 68% air and 32% hydrogen in a 100 cubic foot latex balloon. The experimenters found that no detonation occurred when the mixture was ignited with a hot wire, a spark source or a squib. They did get a detonation when a 2 g



charge of pentolite was used to ignite the mixture. They concluded that the probability of a detonation occurring due to a hydrogen leak into an unconfined space is small. They also pointed out that hydrogen dissipates very rapidly, therefore hydrogen is less dangerous to handle than butane and propane (both of which are heavier than air).

How much energy would be given off, if there was a hydrogen fire?

According to the Handbook of Compressed Gases<sup>31</sup>, the gross heat of combustion of hydrogen is 325 Btu/ cubic foot, which corresponds to 1330 kJ for 110 L of 1 atm hydrogen. 110 L of 1 atm hydrogen is equivalent to the 330 L of 1/3 atm hydrogen that will be in the TRIC. This amount of energy can be compared to the same volume of propane (110 L) at 60 °F and 1 atm. This handbook says that the gross heat of combustion of this propane is 2563.3 Btu/ cubic foot, which corresponds to 10505 kJ for 110 L of 1 atm of propane.

### Appendix C: TRIC Bakeout Studies

The TRIC was baked on Nov 12, 1992 to test the integrity of the Al gasket seals. This was done by the use of the R12 fibreglass insulation, variacs, and heating tapes. The temperature of the TRIC was measured by use of a thermocouple attached to the outside of the TRIC. Figure C.1 shows the TRIC temperature as a function of time. This graph is rather bumpy, because the variacs were turned down over night for safety. After the TRIC was cooled down to room temperature, it was found that

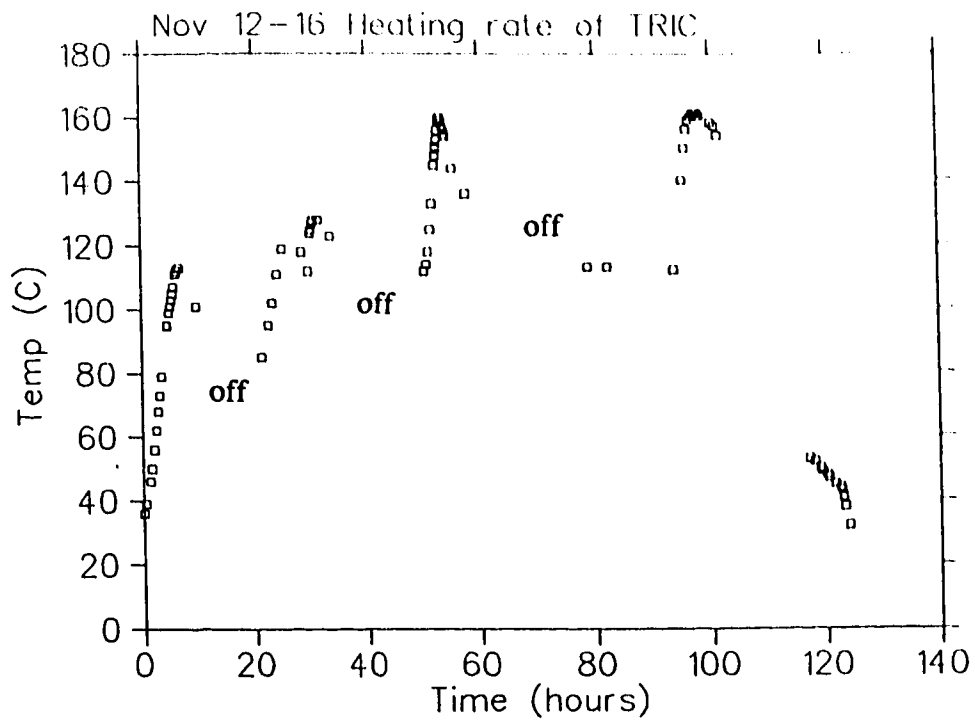


Figure C.1: The TRIC temperature as a function of time for the November 1992 baking.

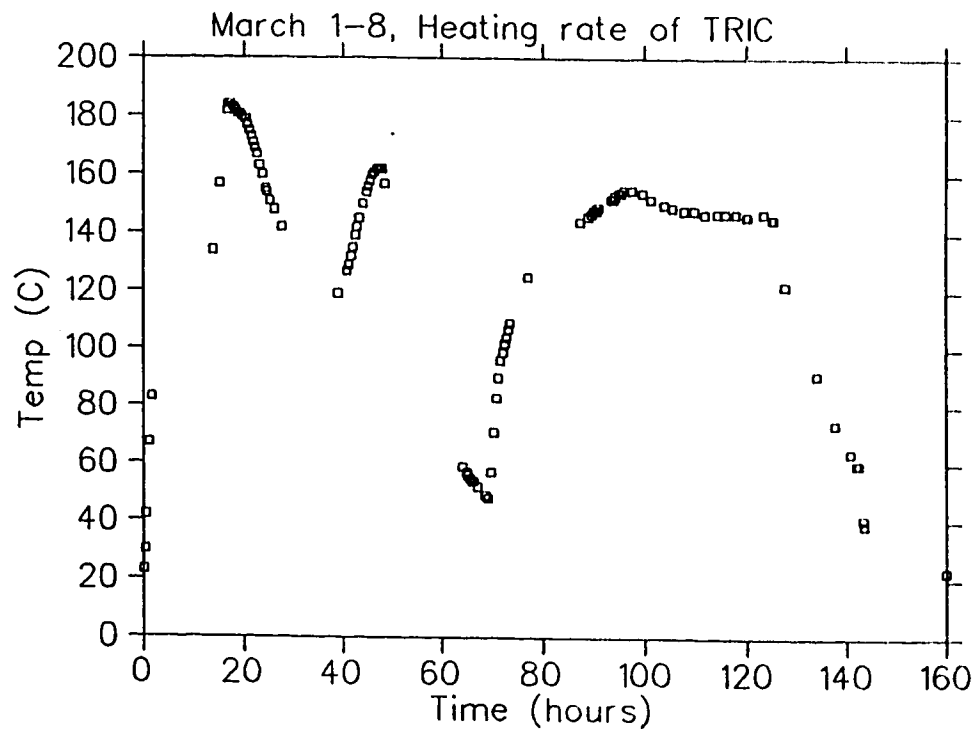


Figure C.2: The TRIC temperature as a function of time for the March 1993 baking.

one of the Al gasket seals leaked. To ensure that the TRIC would not leak during bakeout, the four large flanges on the TRIC were machined so that helicoflex delta seals could be used. Helicoflex seals work like rubber o-rings, but instead of being made out of rubber they are made out of an Al coated alloy spring.

Once the TRIC was assembled with the helicoflex deltas, it was evacuated for 2 to 3 days using a turbomolecular pump. The TRIC was then found to be leak tight by using a He leak detector. The TRIC was then baked in a similar fashion as in November, except that a 4" bellows was used as the manifold and an ion gauge was put directly on the TRIC. Figure C.2 shows the TRIC temperature as a function of time for the March 1, 1993 baking. The graph is bumpy at first, because an equilibrium setting was not found yet. After about 60 hours of heating, the heat was turned off to see if the helicoflex seals had withstood the baking. The seals performed as expected. The pressure was also measured as the TRIC was heated and figure C.3 shows the pressure within the TRIC as a function of time. At the 179 hours mark, there was a power outage at TRIUMF. The turbo pump, used on the TRIC, did not turn back on once the power was turned on. The turbo pump was not turned back on until 1 hour after the power went out. A few hours later it was found that the ion gauge still measured the TRIC pressure to be in the  $10^{-4}$  torr range. Suspecting that the ion gauge needed to be reset, it was turned off and on. After this procedure the ion gauge was reading the TRIC pressure to be in the  $10^{-7}$  torr range. After cooling the TRIC back to room temperature, the lowest TRIC pressure was found to be  $6.8 \times 10^{-9}$  torr. The ion gauge controller was inspected to see if this

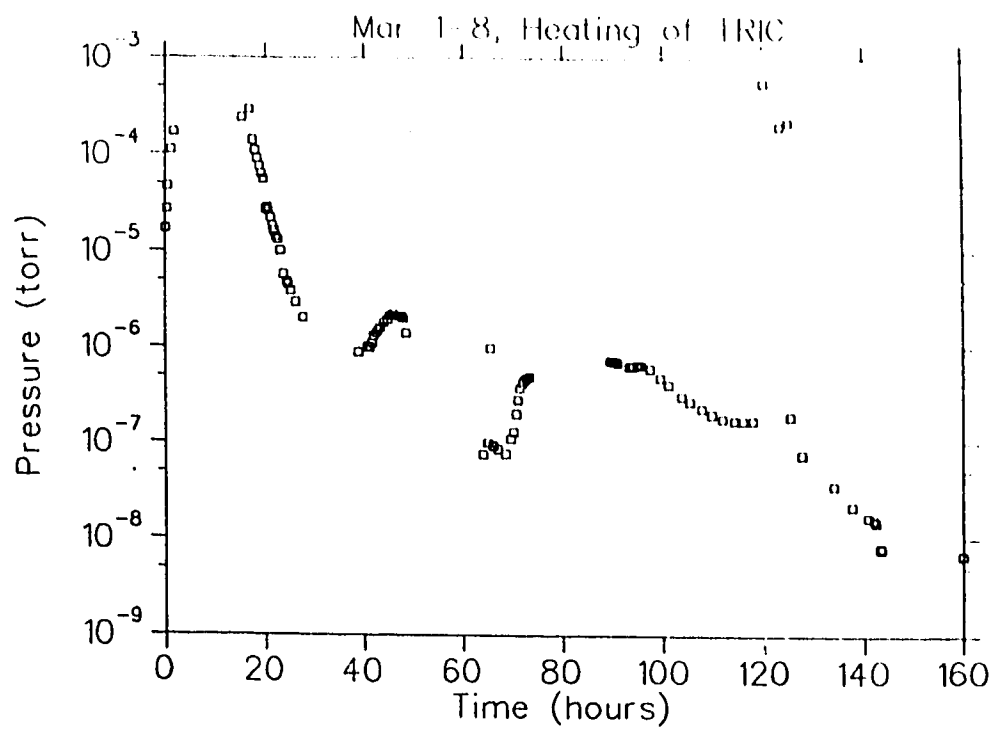


Figure C.3: The TRIC pressure as a function of time for the March 1993 baking.

reading was correct and it was found that the ion gauge controller was in working order.

During the evacuation of the TRIC a few out gassing measurements were made:

Table C.1: Outgassing measurements made on the TRIC

TRIC Temp	Time	Base Pressure	Outgassing Rate (torr L/s cm <sup>2</sup> )	
			Rate of Rise	Conductance
(°C)	(hrs)	(torr)	(x 10 <sup>-12</sup> )	(x 10 <sup>-12</sup> )
23	-55	6.2 x 10 <sup>-6</sup>	890	5400
23	-32	2.3 x 10 <sup>-6</sup>	310	2000
49	69	7.6 x 10 <sup>-8</sup>	5.5	66
60	142	1.6 x 10 <sup>-8</sup>	14	14
23	160	6.8 x 10 <sup>-9</sup>	5.9	5.9

In the above table the time column indicates the time of the outgassing measurement relative to the onset of heating the TRIC. Two methods were used to calculate the outgassing rate.

The first method was to close the valve on the TRIC and measure the rate of rise. The next five graphs (figures C.4 to C.9) show how the pressure rises once the TRIC valve is closed. The third rate of rise outgassing rate is questionable because it may not have measured the true outgassing rate. It may have been a measure of the rate at which the TRIC pumps itself. It can be seen in the last two pressure rise curves that the outgassing rate is quite slow at first. This part of the graph is where the TRIC is pumping itself. Further along the graph the true out gassing rate can be found. This is why there are two slopes in figure C.7 and in figure C.8. This effect is not seen in the third rate of rise measurement (figure C.6). So one would suspect

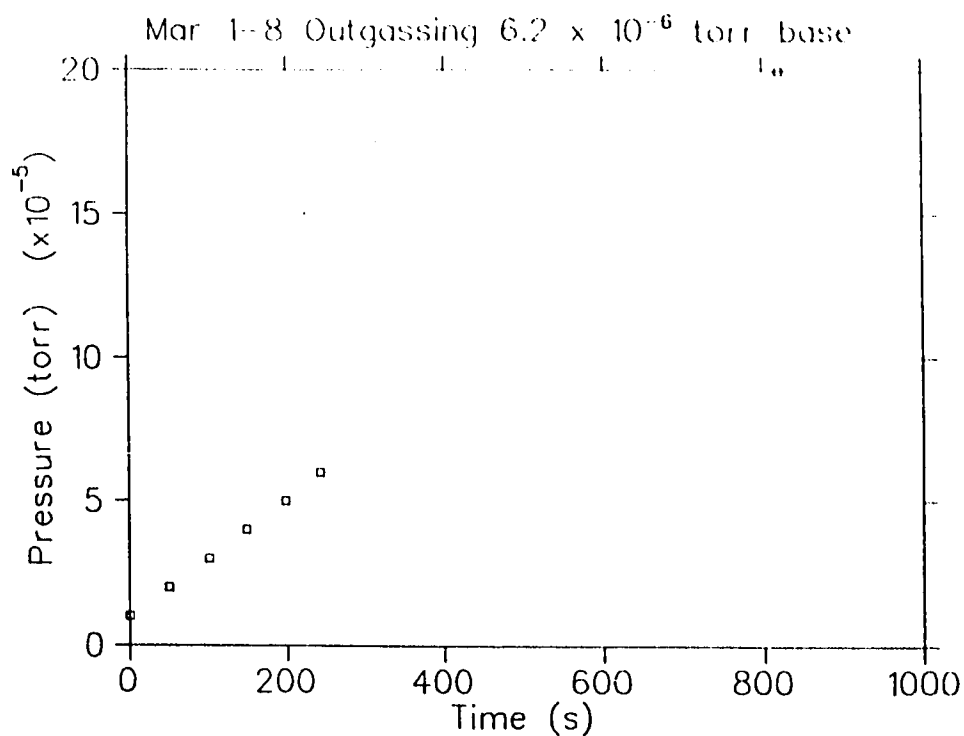


Figure C.4: Rate of rise curve for a base pressure of  $6.2 \times 10^{-6}$  torr.

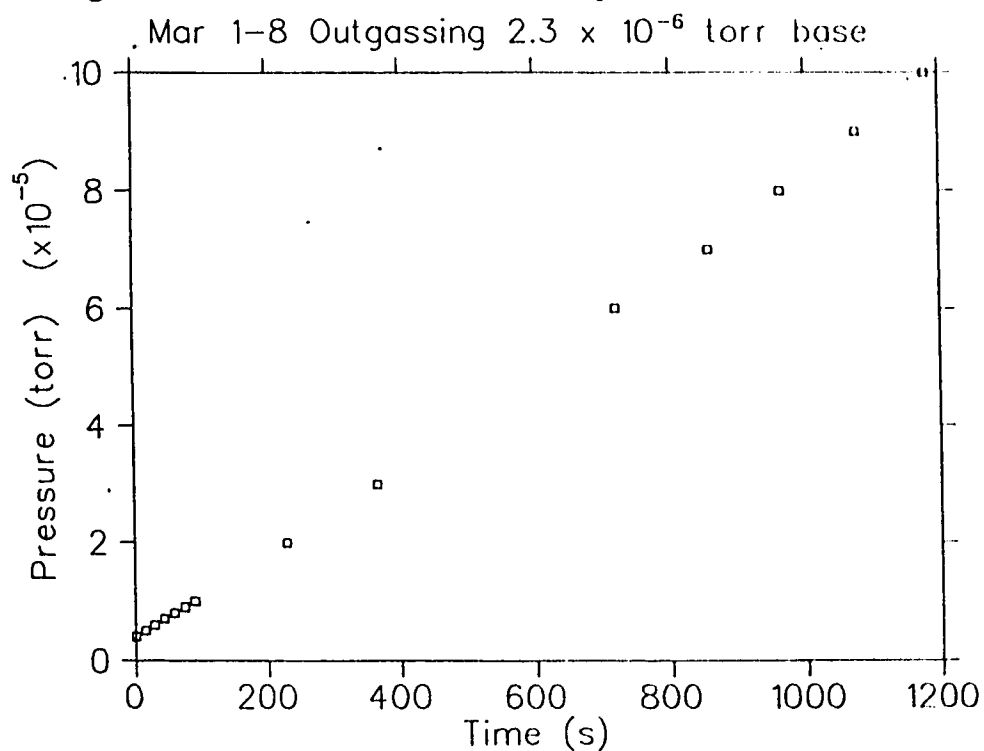


Figure C.5: Rate of rise curve for a base pressure of  $2.3 \times 10^{-6}$  torr.

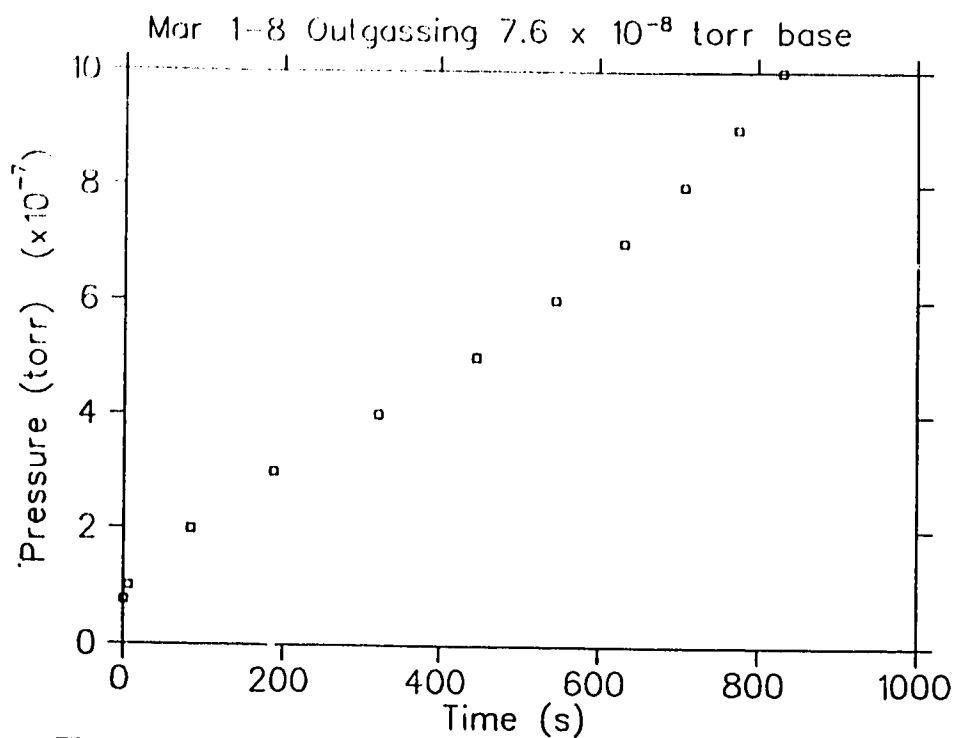


Figure C.6: Rate of rise curve for a base pressure of  $7.6 \times 10^{-8}$  torr.

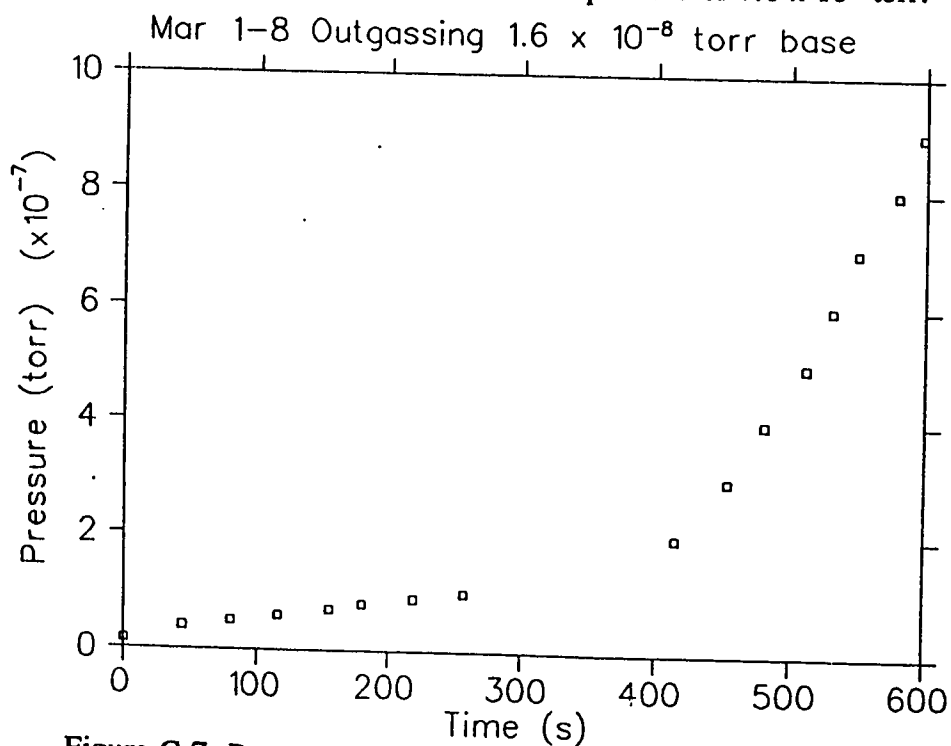


Figure C.7: Rate of rise curve for a base pressure of  $1.6 \times 10^{-8}$  torr.

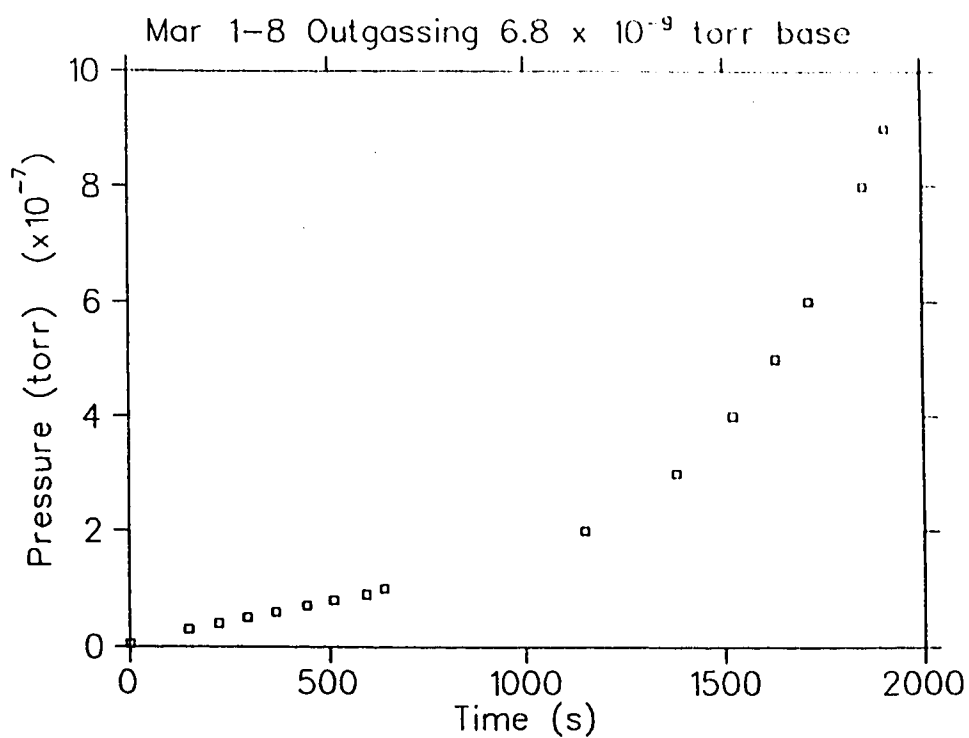


Figure C.8: Rate of rise curve for a base pressure of  $6.8 \times 10^{-9}$  torr.

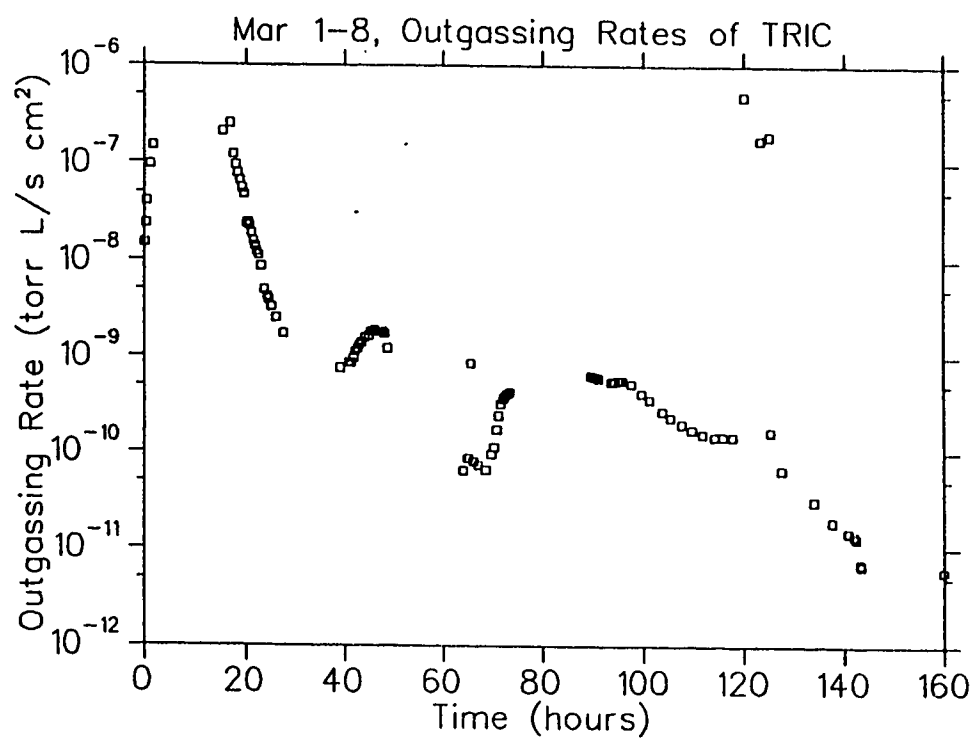


Figure C.9: Outgassing rate of the TRIC as a function of heating time.



that the third measurement was not taken long enough.

The second method determined the outgassing of the TRIC by calculating the conductance of the manifold between the pump and the TRIC. This method also uses pressure measured in the TRIC. So the outgassing rate as a function of heating time was determined and plotted on the last graph (figure C.10).

The rate of rise outgassing measurements made before the TRIC was baked tend to agree with values for electropolished stainless steel from Harris:

	Outgassing Rate (torr L/s cm <sup>2</sup> ) x 10 <sup>-10</sup>	
	1 hour at vacuum	4 hours at vacuum
Stainless Steel (raw)	200	15
Stainless Steel (electropolished)	50	4
Stainless Steel (mech. polished)	20	4

Note that the TRIC has been electropolished. According to O'Hanlon, the outgassing rate of stainless steel which has been baked for 50 hours at 150 °C is  $3.1 \times 10^{-11}$  torr L/s cm<sup>2</sup>. This value is close to our value which was measured after 142 hours of baking at 150 °C.

It turns out that the TRIC may have been contaminated when it was pumped down in the beam line with the intensity profile monitor. In the future these two devices will not be evacuated by the same pump.

## Bibliography

- 1) I. J. R. Aitchison, An informal introduction to gauge field theories, (Cambridge University Press, Cambridge, 1982).
- 2) E. G. Adelberger & W. C. Haxton, Ann. Rev. Nucl. Part. Sci. 1985.35:501-58.
- 3) G. Barton, Nuovo Cimento, 19, 512 (1961).
- 4) B. H. J. McKellar, P. Pick, Phys Rev. D 6:2184 (1972); 7:260 (1973).
- 5) B. R. Holstein, Can. J. Phys. 66, 508 (1988).
- 6) B. Desplanques, J. F. Donoghue, B. R. Holstein, Ann. Phys. 124: 449 (1980).
- 7) P. D. Eversheim et al., Phys. Lett. B256, 11 (1991).
- 8) J. M. Potter et al., Phys. Rev. Let. 33, 1307 (1974).
- 9) W. Haeberli, Can. J. Phys. 66, 485 (1988).
- 10) G. Roy in Conference Proceedings of The Lake Louise Winter Institute: Spin and Symmetry 1992, (World Scientific Publishing, Singapore, 1992).
- 11) R. E. Mischke, Can. J. Phys. 66, 495 (1988).
- 12) V Yuan et al., Phys. Rev. Let. 57, 1680, (1986).
- 13) D. E. Driscoll and G. A. Miller, Phys. Rev. C39, 1951, (1986).
- 14) M. J. Iqbal and J. A. Niskanen, Phys. Rev. C42, 1872, (1990).
- 15) T. Goldman and D. Preston, Nucl. Phys. B217, (1983); Phys. Let. B168, 415, (1986).
- 16) L. G. Greeniaus, TRIUMF Kinematics Handbook, second edition, (1987).
- 17) W. J. Price, Nuclear Radiation Detection, (McGraw-Hill Book Co., New York, 1958).
- 18) J. Sharpe, Nuclear Radiation Detectors, (John Wiley & Sons, inc, New York, 1964).
- 19) R. G. Korteling and R. E. L. Green, Phys. Rev. C22, 1594, (1980).

- 20) J. R. Wu et al., Phys. Rev. C19, 698, (1979).
- 21) L. G. Greeniaus private communication.
- 22) G. M. Raisbeck et al., Phys. Rev. C12, 527, (1975).
- 23) E. N. Volin et al., Phys. Let. 55B, 409, (1975).
- 24) Marik Dombsky private communication.
- 25) R. Silverberg and C. H. Tsao, APJSA2 25 (220), 315, (1973).
- 26) F. H. Attix, Introduction to Radiological Physics and Radiation Dosimetry, (John Wiley & Sons, inc, New York, 1986).
- 27) B. B. Rossi, High Energy Particles, (Prentice-Hall, New York, 1952).
- 28) W. R. Leo, Techniques for Nuclear and Particle Physics Experiments, (Springer-Verlag, New York, 1987).
- 29) Jim Birchall private communication.
- 30) A. D. Little, inc., Handbook for Hydrogen Handling Equipment, (Wright-Patterson Air Force Base, Ohio, Wright Air Development Division, 1960).
- 31) Compressed Gas Association, Handbook of Compressed Gases, (Rienhold Pub. Corp. 1966).
- 32) N. S. Harris, Vacuum Technology, (London Caledonian Press (T. U.) Ltd., Watford, Herts, 1981).
- 33) J. F. O'Hanlon, A User's Guide to Vacuum Technology, (John Wiley & Sons, 1980).